Quantifying Airway Dilatation in the Lungs from Computed Tomography

Kin Quan

A dissertation submitted in partial fulfillment

of the requirements for the degree of

Doctor of Philosophy

of

University College London.

Department of Medical Physics and Biomedical Engineering

University College London

May 4, 2021

I, Kin Quan, confirm that the work presented in this thesis is my own. Where information has been derived from other sources, I confirm that this has been indicated in the work.

Abstract

Non CF bronchiectasis and idiopathic pulmonary fibrosis (IPF) are pulmonary diseases characterised by the abnormal and permanent dilatation of the airways. Computed tomography (CT) is used in clinical practice to diagnose and monitor patients with the disease. Currently, analysis of the scans is performed by manual inspection and there is no established computerised method to quantify the enlargement of airways.

I developed a pipeline to quantify the cross-sectional area for a given airway track. Using an airway segmentation, my proposed algorithm measures the area at contiguous intervals along the airway arclength from the Carina to the most distal point visible on CT. I showed the use of the data generated from the pipeline in two applications. First, I proposed a novel tapering measure as the gradient of a linear regression between a logarithmic area against the arclength. The measurement was applied to airways affected by bronchiectasis. Second, I used Bayesian Changepoint Detection (BCD) with the area measurements to locate the progression of IPF along the airway track.

The proposed pipeline was applied to a set of clinically acquired scans. I show a statistical difference ($p = 3.4 \times 10^{-4}$) in the tapering measurement between bronchiectatic ($n = 53$) and controlled ($n = 39$) airways. In addition, I report a statistical difference ($p = 7.2 \times 10^{-3}$) in the change in measurement between airways remaining healthy ($n = 14$) and airways that have become bronchiectatic ($n = 5$). I show the tapering measurement is reproducible independent to voxel size, CT reconstruction, and radiation dose. Using BCD, I show on simulated data ($n = 14$) my proposed method can detect the progression of IPF within 2.5mm. Finally, using results from BCD, I present a novel measure of IPF progression as the percentage volume change in the diseased region of the airways.

Impact Statement

In my PhD I developed tools to describe the size of the airways from Computed Tomography (CT) scans. I have shown that my proposed tools are accurate and can be used with different CT scanners without loss of precision. The algorithms are designed to be used on diseases that causes the airways to abnormally expand or dilate. There are two possible applications to my work.

The first application concerns bronchiectasis. Patients with the disease can experience exacerbation; a sudden deterioration of the patients health. These events can be distressing and requires medical intervention. My work has the potential to help establish the relationship between shape of the airways and the number of exacerbations from a given patients.

The second application concerns idiopathic pulmonary fibrosis (IPF). The disease is poorly understood, and patients are not expected to survive for more then 5 years after being diagnosed. My algorithms can be used to monitor the progression of airway affected by IPF. Thus, my work may be useful in drug trials for the disease.

Code

The code is available at `https://github.com/quan14`, last accessed on May 4, 2021

Contents

List of Figures

List of Tables

Chapter 1

Prologue

1.1 Introduction

In this thesis, I developed a set of algorithms to quantify and assess changes in the size of the airways in the lungs. The motivation is to assess the severity and progression of airways affected by non-cystic fibrosis bronchiectasis or idiopathic pulmonary fibrosis. Both diseases are characterised by abnormal dilatation of the airways. The analysis of the disease is strictly based on computed tomography, a modality that uses ionising radiation to construct three dimensional images of the human anatomy.

In this chapter, I give a general introduction to the thesis, discussing the background knowledge and assumptions. The chapter is organised in the following sections: (i) General anatomy of lungs (Sec. 1.2). (ii) Image acquisition from a CT scanner (Sec. 1.3). (ii) Bronchiectasis and idiopathic pulmonary fibrosis (Sec. 1.4). (iv) Summary of the proceeding chapters (Sec. 1.5).

1.2 Lung Anatomy

The human lungs are two sets of organs located inside the ribs, they are called the left lung and right lung. (Fig. 1.1). Both lungs consist of airways, blood vessel and connective tissue known as the lung parenchyma [7]. The right lung is larger then the left lung. In addition, with typically incomplete division; the right and left lungs contains three and two lobes respectively. Each lobe is separated by fissures. The function of the lungs is for gas exchange, where air is transported by the trachea [8].

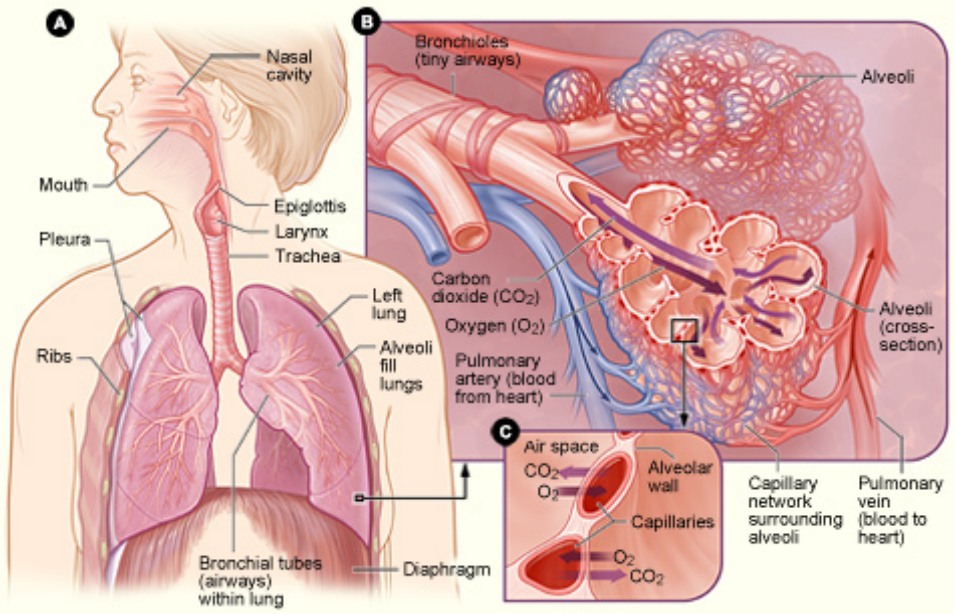

Figure 1.1: An illustration of the general anatomy of the healthy lungs. The airways is accompany by the pulmonary artery. At the end of each airway is the alveoli, where gas is exchanged form the blood. Image was taken from National Heart, Lung and Blood Institute, USA, `www.nhlbi.nih.gov/health-topics/how-lungs-work`, last assessed May 4, 2021.

1.2.1 Pulmonary Airways

The airways are a set of bifurcating tubes from a single larger tube. As displayed on Figure 1.1, the structure of the airway starts from the trachea - a tubular structure that lies outside of the lung. The trachea then bifurcates into the main bronchi where it enters the lung [7]. The bifurcation continues for around 22 to 24 times. The airways then terminate into a sac known as the alveoli. The airways can be described by generation. Conventionally, the trachea is labelled as generation 0. Next, generation 1 is described as the group of airways starting at the bifurcation from the trachea and to the end of the next bifurcation. The proceeding airway generations are labelled by the same convention. For a healthy set of lungs, the diameter of the airways decrease after each bifurcation [9, 10].

1.2.2 Pulmonary Blood Vessels

The pulmonary blood vessels are located inside the lungs. Similarly with the airways, the blood vessels are a set of bifurcating tubes. A part of the pulmonary blood vessel - the artery, follows closely with the airways. The artery bifurcates until the

Figure 1.2: LEFT: A image of a CT scanner in a clinical setting. RIGHT: The internal components of the CT scanner. The X-ray tube (green arrow) and detectors (blue arrow) rotates as the patient transverse through the bore. Images adapted from Wikipedia, `en.wikipedia.org/wiki/CT_scan`, last accessed on May 4, 2021.

vessels become the capillaries [9].

1.3 Computed Tomography (CT)

1.3.1 Introduction

Computed Tomography is an imaging modality using ionising radiation to construct 3D images of the human anatomy at millimetre scale. The technology developed in the seventies [11] and has become the recommended modality for investigating the presence of bronchiectasis [12] and IPF [13] due to the high contrast between air and soft tissue. In this section, we consider the fundamentals of CT imaging in terms of image acquisition (Sec. 1.3.2), reconstruction (Sec. 1.3.3), representation (Sec. 1.3.4) and sources of noise (Sec. 1.3.5).

1.3.2 Image Acquisition

To physically acquire a CT image, the patient lies on the CT bed and transverses through the CT scanner (Fig. 1.2). The scanner (Fig. 1.2) consists of an X-ray tube emitting X-rays towards a set of detectors. Both the X-ray tube and detector rotates in the gantry as the patient transverses thought the bore. The output is a set planar images along the patients [14, 15].

1.3.2.1 Physics of Image Acquisition

The main component in image formation using ionising radiation is in the interaction between X-ray and matter. To proceed, I consider the intensity of a beam of X-ray denoted as I. The quantity is defined as the amount of energy crossing a unit area in a normal position to the X-ray beam in unit time [16].

As X-rays are emitted, assuming the radiation passes through a given material, the X-ray intensity decreases at an exponential rate and is determine as:

$$I = I_0 e^{\int \mu(x)dx} \tag{1.1}$$

where I_0 is the initial intensity and μ the linear attenuation coefficient [16]. I will discuss in the next section that by taking a series of X-ray beam measurements around the body, I can use the concept in Equation 1.1 to give information on the geometry and contrast of a scanned object.

1.3.3 Image Reconstruction

In this section, I discuss the mathematical foundation of converting data acquired from a CT scanner into an image displaying the physical geometry of the scanned object. To this end, I relate the physical image acquisition with the mathematical principle of filtered back-projection. The following is an adapted derivation of the filtered back projection based on Heish [17] and Kalender [14].

To begin, consider the following setup of an X-ray beam, $x\cos\theta + y\sin\theta = r$ displayed on Figure 1.3. When the CT scanner completes a scan, the output is a series of integral function p known as a sinogram (example on Fig. 1.4). The output describes the sum of the attenuation coefficient of the object. Formally, the function p is described along the X-ray beam and is defined as:

$$p(\theta, r) = \int\int \mu(x,y)\delta(x\cos\theta + y\sin\theta - r)dxdy. \tag{1.2}$$

The purpose of considering Equation 1.2 is to recover the function μ. To this end, it is observed Equation 1.2 is of the form of a Radon transformation. Thus, mathe-

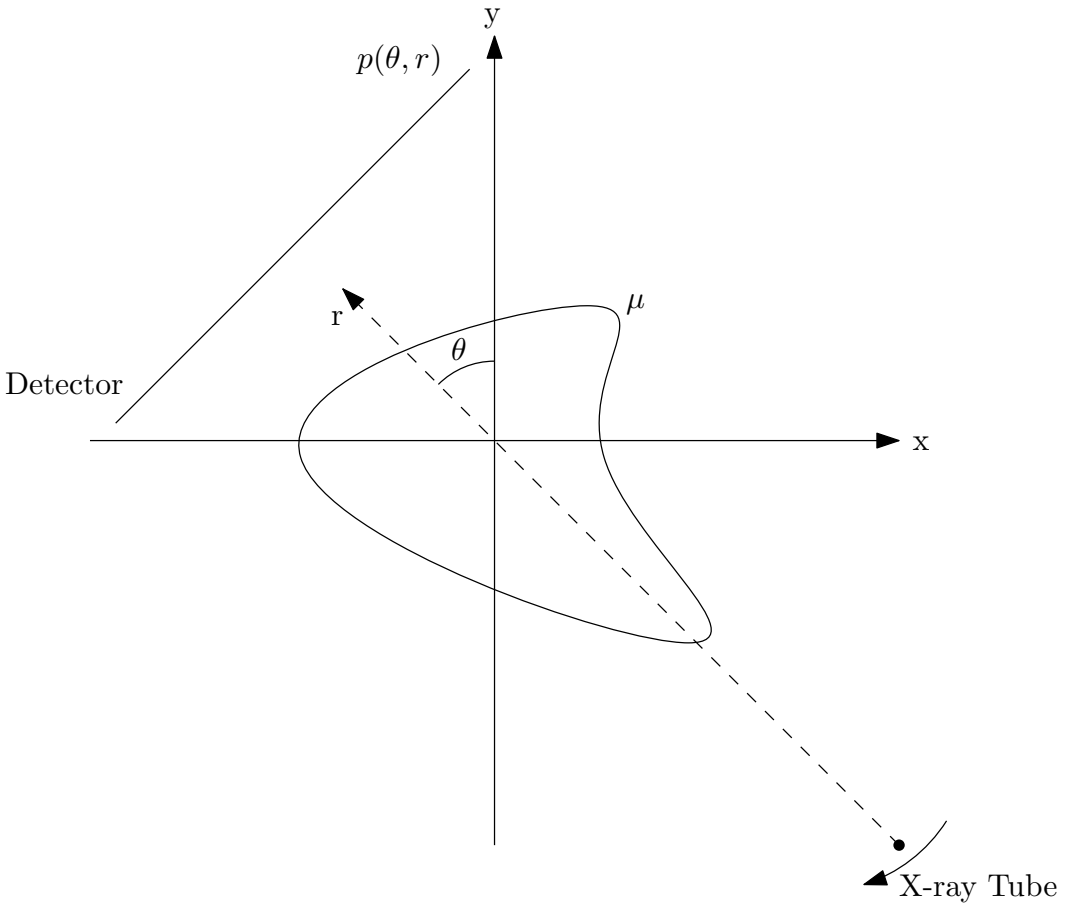

Figure 1.3: Schematic diagram linking the coordinate system in $p(\theta, r)$ with the object $\mu(x, y)$.

matically in order to recover μ, one would have to perform an inverse Radon transformation.

To begin the inverse transformation, I consider the Fourier transformation of $p(\theta, r)$ which gives:

$$P(\theta, r) = \int \mu(x, y) e^{-2\pi i k(x\cos\theta + y\sin\theta)} dxdy, \tag{1.3}$$

where the P is the Fourier transform of p. To proceed, it is observed that Equation 1.3 is of the form the 2D Fourier transform when considered with the transformation $k_x = k\cos\theta$, $k_y = k\sin\theta$. Thus by considering the 2D inverse Fourier transform and

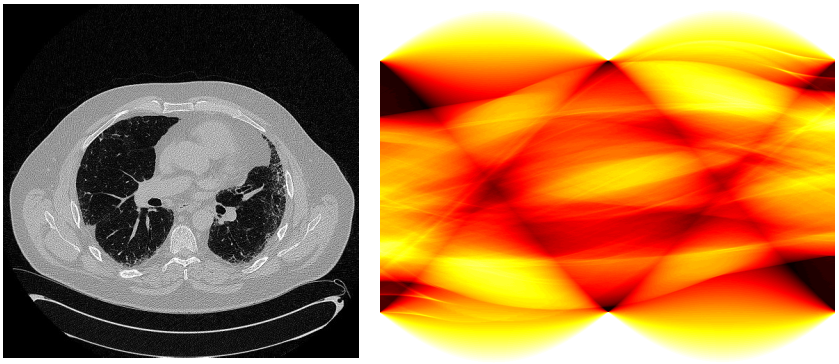

Figure 1.4: LEFT: Example of a reconstructed chest CT scan. RIGHT: A simulated sinogram of the corresponding CT scan.

the coordinate transform of k_x, k_y, I obtained:

$$\mu(x,y) = \int P(\theta,r) * K(r) d\theta \tag{1.4}$$

where $*$ denotes a convolution operation and the function $K(r)$ known as the ramp kernel defined as:

$$K(r) = \int |k| e^{2\pi i k(x\cos\theta + y\sin\theta)} dk. \tag{1.5}$$

Thus, the filtered back-projection has been derived. Equation 1.4 can be interpreted as the sum of the Fourier transformed projection smoothed by a kernel. As the problem is discretize and ill-posed, to recover the exact attenuation map μ is infeasible. To compensate, manufacturers of CT scanners developed different reconstruction kernels $K(r)$ to highlight features to the radiologists [17].

1.3.4 Image Representation

After image reconstruction, we obtained the CT image (example on Fig 1.4). To apply my proposed image processing algorithms, the images are required to be represented digitally. To this end, I discuss the digital representation of a CT image and how anatomical features can be differentiated.

1.3.4.1 The CT image

The CT images are stored as a three dimensional matrix, where the location of the array provides the coordinate system [18]. The axis are based on the anatomical

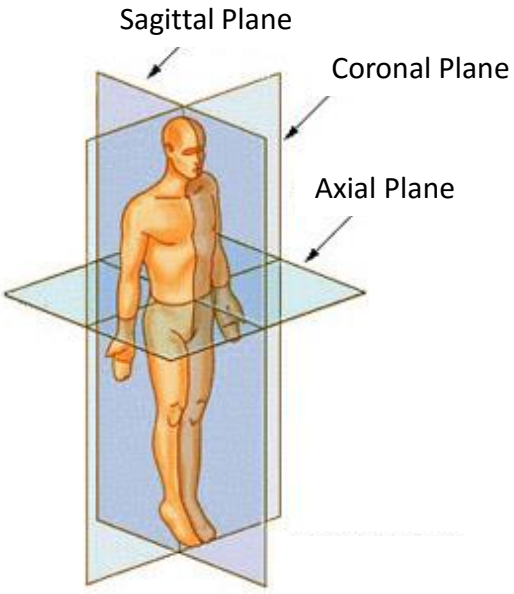

Figure 1.5: Diagram of the axial, sagittal and coronal plane on the body. Image was adapted from National Heart, Lung and Blood Institute, USA, `training.seer.cancer.gov/anatomy/body/terminology.html`, last assessed May 4, 2021.

plane – axial, sagittal and coronal plane as displayed in Figure 1.5.

Each entry values of the matrix corresponds to the property of a voxel or "volume element". It corresponds to a defined volume of the patient's tissue. For my work, we assume the voxels are at contiguous intervals i.e. each point on the scanned objected is contained in a voxel. The intensity value of each voxel is known as the CT number and is given in Hounsfield Units (HU), defined as:

$$\frac{\mu_T - \mu_{water}}{\mu_{water}} 1000, \tag{1.6}$$

where μ_T and μ_{water} is the attenuation coefficient of an arbitrary tissue T and water respectively [14].

1.3.4.2 Chest CT image

In order to quantify the airways, one would need to consider the intensities of the structures of the lungs. The information enables image processing algorithms to relate the voxel to the corresponding anatomy. For my work, I consider three components of the lungs: airways, blood vessel and lung parenchyma.

For airways, the structure consists of a lumen filled with air. Thus, in terms of CT number, the airway wall is approximately 150HU and the internal lumen is approximately -1000HU [19]. For blood vessel, the lumen is filled with blood thus the CT number is approximately 50HU [14]. Finally, for lung parenchyma, the structure has a CT number between -980HU to -800HU as it contains a combination of connective tissue, alveoli and air [20].

1.3.5 Challenges in CT Image Processing

CT images can contain noise or artefacts causing image quantification tools to become inaccurate or lose precision. In this section, I will discuss the main causes of errors: (i) Photon starvation (Sec. 1.3.5.1). (ii) Partial volume (Sec. 1.3.5.2) . (iii) Motion (Sec. 1.3.5.3). Finally, I discuss the effect of artefacts on measurements taken from image processing tools (Sec. 1.3.5.4).

1.3.5.1 Photon Starvation

Photon starvation is caused when too few photons reach the detector, for instance in low dose scans. The phenomenon causes two distinguishing artefacts. First, streaks in the image, often from dense objects in the body like bone [21, 17]. Secondly, an increase in standard deviation of intensities in a uniform material such as air in the trachea [22]. Careful consideration is needed when designing algorithms for low dose scans. An increase in noise will remove the appearance of edges. Various image processing algorithms used edges to identify features in the image such as airway lumen.

1.3.5.2 Partial Volume

Partial volume is caused when objects do not occupy the entire voxel. For example, in CT chest scans, voxels can contain both the smaller airways and parenchyma. The resulting intensity is a partial volume averaging in CT numbers between airways and parenchyma. For image processing, partial volume reduces the precision the image processing algorithms as features such as edges are only identifiable up to the resolution of the image [17].

1.3.5.3 Motion

Motion artefacts are caused when the patient moves during the scan. For example, respiratory motion i.e. the patient breathes during the data acquisition. The moving organs causes a misregistration during image reconstruction and hence results in an inconsistent set of projections. The resulting image can contain streaking and blurring. The artefacts can cause inaccuracy for image processing algorithms for example when segmenting the airways. The motion artefact shifts the appearance of the airways in the image [17, 23].

1.3.5.4 Overcoming Artefacts

Image artefacts can reduce precision for a range of image processing algorithms for quantifying airways. For example, computing the centreline of the airways [24] and finding the cross-sectional area of the lumen [25]. The resulting lack of precision and reproducibility can limit the efficacy of any proposed algorithms in two ways. (i) First, the data taken from images with artefacts may not be sensitive to monitor disease progression thus unable to compare results across longitudinal scans. (ii) Second, the lack of precision, may exclude images taken from different acquisitions parameters or scanner thus limiting the amount of resources.

In the literature, a wide range of image processing algorithms have been proposed to remove or reduce the appearance of artefacts on the image [26, 27, 28]. However, these methods can be computationally intensive and can potentially bias the appearance of features. Thus, part of my contribution is to show my proposed quantification algorithms are reproducible in images from different acquisition parameters such as radiation dose and voxel sizes.

1.4 Airway Diseases

In this section, I discuss two pulmonary diseases; bronchiectasis (Sec. 1.4.1) and idiopathic pulmonary fibrosis (IPF) (Sec. 1.4.2). Both diseases involves the abnormal dilatation and damage of the airways.

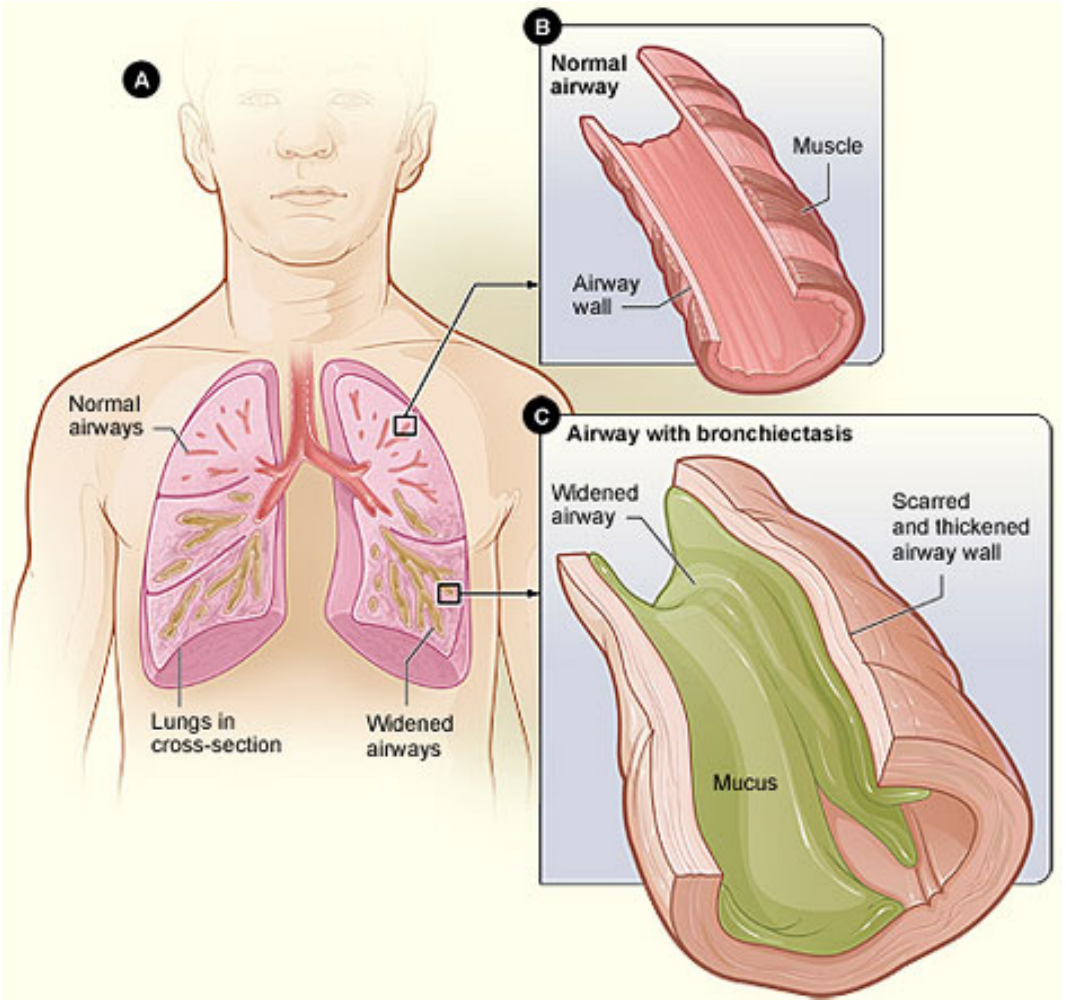

Figure 1.6: An illustration of healthy airways and airways affected by bronchiectasis. Image was taken from National Heart, Lung and Blood Institute, USA, `www.nhlbi.nih.gov/health-topics/bronchiectasis`, last accessed May 4, 2021.

1.4.1 Bronchiectasis

1.4.1.1 Pathophysiology

Non-CF bronchiectasis or bronchiectasis is a disease defined by the British Thoracic Society as the permanent damage or dilatation of the airways [12] as illustrated in Figure 1.6. The cause of the dilatation are diverse; examples of aetiologies include damage from a previous infection such as tuberculosis, an immunodeficiency like HIV or obstruction in the airway such as a foreign body [12, 29, 30]. However, for a large number of cases, between 30% to 50%, the cause remains unknown and therefore classed as idiopathic [31, 12].

Patients with bronchiectasis can present symptoms with cough, increase mucus production, recurrent chest infection, chest discomfort, coughing of blood and weight loss [12]. The progression of the disease has been described as the vicious cycle of dilated airways causing infection, leading to inflammation and causing further airway damage and dilatation [32].

Treatment and management of bronchiectasis are based on two approaches. First, identify and if possible, treat the cause of the bronchiectasis. Second, to stop the vicious cycle for example reducing airway inflammation. A range of recommended treatments include: physiotherapy to remove mucus, inhaled agents to loosen mucus and hydrate airways and oral administered antibiotics [12]. Inhaled antibiotics have been recommended for some patients however the effectiveness of some drugs have been disputed. In some drug trials, some proposed drugs perform worse than the placebo group [33, 29, 34].

Prognosis of bronchiectasis can vary, in severe cases patients can suffer decrease in lung function. In addition, patients can experience frequent exacerbations [33], these events are defined where patients experience a worsening of symptoms such that they require treatment. The study of exacerbations is an active area of research as these events can have a devastating consequence on patients. Unexpected occurrences of exacerbations can contribute to a decrease in quality of life. In addition, the frequency of exacerbations is used as an end point in clinical drug trials. [35, 36].

1.4.1.2 The Role of CT Imaging

High resolution computed tomography is the gold standard for patients with suspected bronchiectasis. The British Thoracic Society [12] recommends using volumetric CT with slice thickness smaller than 1mm. Patients are scanned in the supine position and at full inspiration. Key features that indicates the presence of bronchiectasis are the ratio between the airway lumen and adjacent pulmonary artery (broncho-arterial or BA ratio) are greater then 1, lack of tapering and airway visibility in the periphery of the lungs (Examples on Fig. 1.7). In addition, the signs of airway wall thickening and mucus blocking airways are indirectly associated with

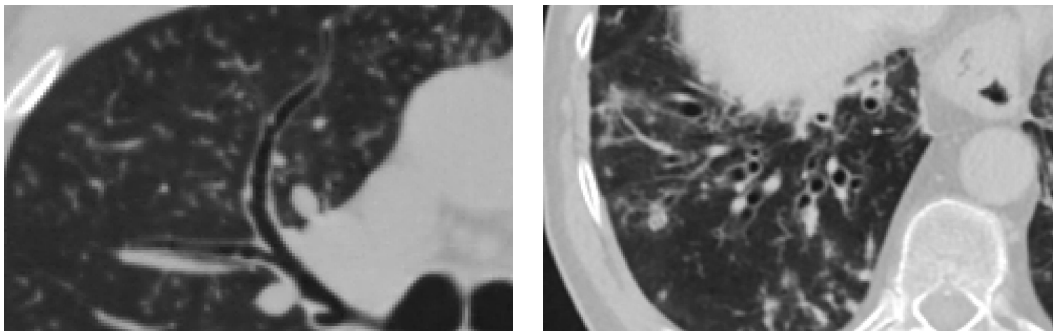

Figure 1.7: Examples of chest CT scans with bronchiectasis. LEFT: A bronchiectatic airway showing a lack of taper. RIGHT: Bronchiectatic airway being larger than its accompany pulmonary artery.

bronchiectasis.

For radiological quantification, clinicians have qualified the presence of bronchiectasis on a lobar basis. In particular, the gold standard of quantifying bronchiectasis on CT images is through a variation of the Bhalla score [37]. The scoring system requires a clinician to manually score from 0 to 3 based on a range of features: broncho-arterial ratio, airway wall thickening, number of lobes with bronchiectasis, abnormal amount of mucus and the presence of collapses or holes in the lung.

Radiological scoring combined with other clinical measurements have shown to be predictors of future hospitalization or mortality. Two bronchiectasis severity scores have been developed. First, The Bronchiectasis Severity Index (BSI) [38] is a tool design to identify patient at risk of exacerbations or mortality. Inputs used in the BSI are lung function, Reiff score [39] (a variation of the Bhalla score) and bacteriology in the lung. Second, The FACED score [40] was designed to score the severity of bronchiectasis in terms mortality in the next 5 years. The scoring system uses a combination of data: spirometry, age, bacteriology, number of lobes effected by bronchiectasis, breathing difficulties. Both scoring systems have been validated on large international datasets and shown to be effective predictors of mortality [41, 42]. Thus, in both editorials [43, 44] and reviews [34, 45] both scoring system are considered state of the art.

1.4.1.3 Current Challenges in CT Imaging

Current radiological quantification has several limitations and challenges. In terms of anatomy, it has been acknowledged that the blood vessel may not remain constant, thus contradicting the broncho-arterial ratio as feature for diagnosis [46]. In terms of the Bhalla scoring system, the method is labour intensive and crude. As mentioned by Saleh and Hurst [43], patients with localised, heavy dilated bronchiectasis may score equivalently to a patient with widespread but mild form of bronchiectasis. Finally, the Bhalla score was developed for cystic fibrosis patients thus includes features such as the presence of mucus which may not appear in non-CF bronchiectasis.

I address the limitations by developing a novel computerize tapering measurement. The proposed tapering measurement has several advantages:

1. The measurement only considers the dilatation of the airways thus removing the need of the broncho-arterial ratio.

2. After airway segmentation, acquiring the tapering measurement is an automatic processing thus removing manual processing and inter user errors.

3. The output is a continuous numerical variable compared to a discrete 0 to 3 Bhalla score, thus providing a sensitivity to measure subtle changes in the airways.

1.4.2 Idiopathic Pulmonary Fibrosis (IPF)

1.4.2.1 Pathophysiology

Idiopathic Pulmonary Fibrosis (IPF) is the disease defined by the American Thoracic Society [13] as a chronic, progressive, fibrosing (scarring) interstitial pneumonia (inflammation) of unknown cause (illustrated on Fig 1.8). IPF mainly affects patients over 50 years old. Factors that increases the risk of the disease includes being male, history of cigarette smoking and family history of fibrosing lung disease.

Patients with IPF are treated with a range of approaches, the overall aim is to improve the quality of life and slow progression of the disease. Management of

IPF involves stopping smoking, vaccinations against influenza, pulmonary rehabilitation (structured exercise) and providing supplementary oxygen. Lung transplantation has also been suggested as a possible treatment however, for many patients, the referral is too late for transplantation [47, 48]. In terms of pharmacologic management, two drugs; Nintedanib [49] and Pirfenidone [50] were shown to be effective at slowing the progression of IPF. However, both drugs have major challenges and limitations. First, both drugs are expensive with each medication costing over $100,000 USD. Secondly, both drugs can cause patients to experience adverse effects such as skin problems and diarrhoea, resulting in patients reducing dosage or stopping treatment completely. Finally, there has been no head to head comparison on the effectiveness between the two drugs, thus causing clinicians difficulty to choose a single drug or to use both drugs at the same time [47].

Prognosis of patients with IPF is poor, the median survival time is 2 to 4 years [48]. Furthermore, patients with IPF have an increased risk of blood clots, high blood pressure and lung cancer. It is recognised by Lindell at al. [51] that patients with IPF will reach a stage where death is imminent. Understanding the rate of the IPF progression remains poor [52] and can have clinical consequences on treatment. As mentioned in Recheldi et al. [48] patients with decrease lung capacity during treatment may not be a sign of treatment failure as it is impossible to compare progression of the same patient without treatment.

1.4.2.2 The Role of CT Imaging

CT is used to diagnose and monitor the progression of IPF. Patients with suspected IPF are recommended to be CT scanned in contiguous thin slices ($<$2mm) with a high frequency reconstruction kernel [53]. Patients should be scanned at full inspiration to total lung capacity. The patterns used to determine the presence of IPF are known as usual interstitial pneumonia (UIP). The UIP patterns mainly consists of three anatomical features: honeycombing, reticular pattern and traction bronchiectasis (Examples on Fig. 1.9) [13, 53].

Honeycombing is defined as the cystic (abnormal sac) airspaces which are clustered, of a similar size (3-10mm) with thick and well-defined walls [53]. It has been

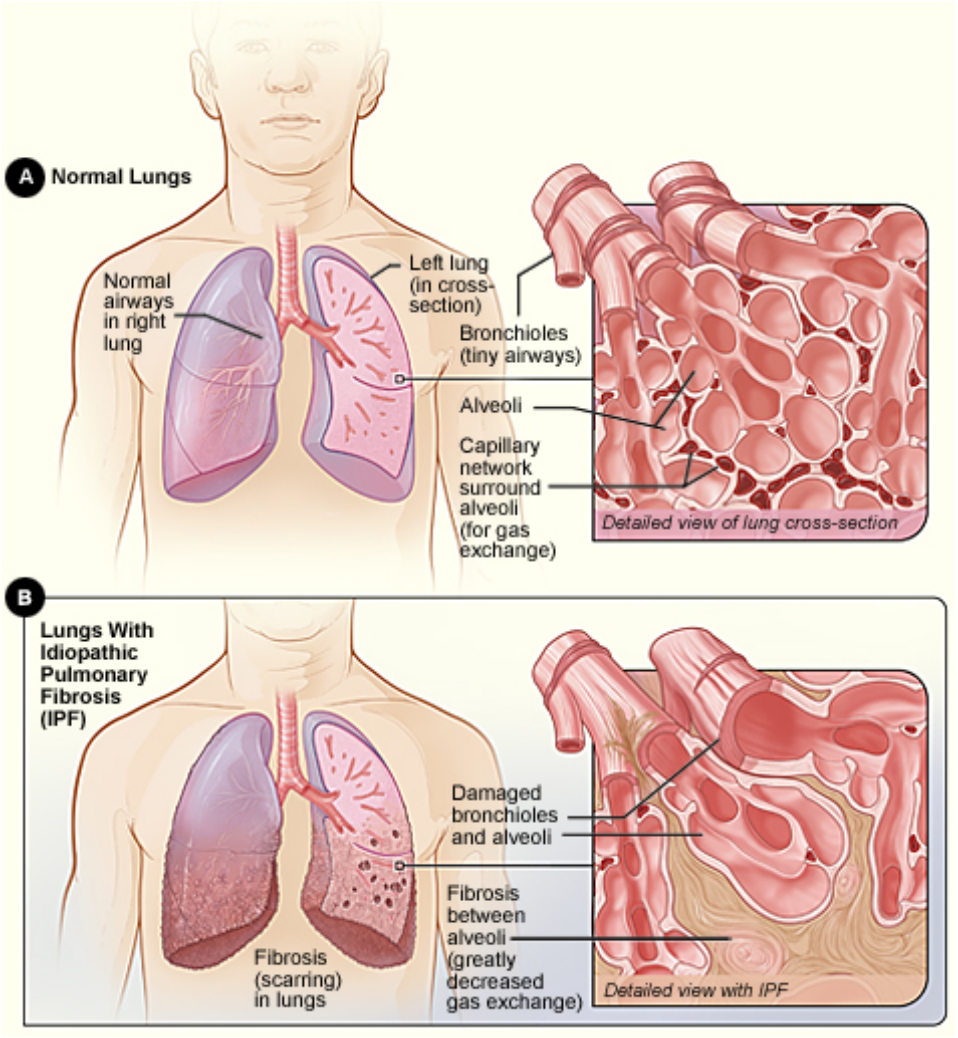

Figure 1.8: An illustration of how the alveoli changes in patients with IPF. Image was taken from National Heart, Lung and Blood Institute, USA, `www.nhlbi.nih.gov/health-topics/idiopathic-pulmonary-fibrosis`, last assessed May 4, 2021.

reported in honeycombing may not be a reliable indicator of IPF. In Jacobs and Hansell [54], they stated that patients with IPF may not have honeycombing. In addition, the literature [55, 53] reports high level of disagreement between observers when identifying the presence of honeycombing.

Reticular pattern are high contrast fine lines on the lungs. In UIP, the lines are irregularly spaced and consist of different thickness [53]. Digitalised identification of reticular pattern is a challenging task. In Jacob et al. [56], the proposed computerized algorithm misclassified regions of reticular pattern as vessels. Furthermore, in Maldonado et al. [57], there have been some disagreements between computerize

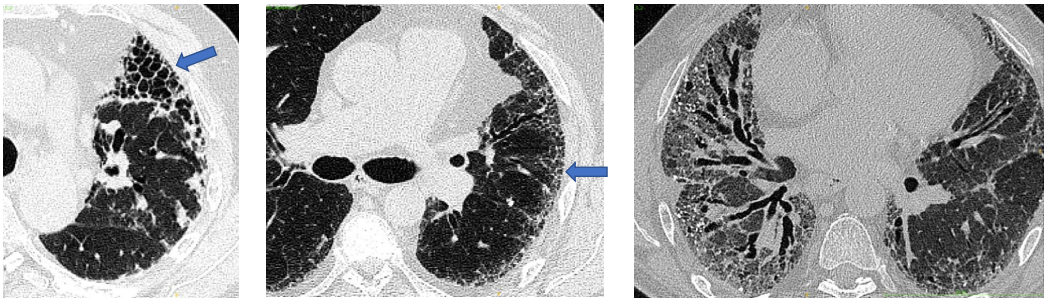

Figure 1.9: Examples of chest CT scans affected by IPF: LEFT: Example of honeycombing (blue arrow). MIDDLE: Examples of reticular pattern (blue arrow). RIGHT: Example of traction bronchiectasis caused by IPF.

and manual labels of reticulation.

Finally, traction bronchiectasis are airways that can be seen in the periphery of the lungs and where the airway wall are varicose or beaded like in appearance [13]. Traction bronchiectasis shares similarities to non CF bronchiectasis (Sec. 1.4.1). However, the distinguishable difference is traction bronchiectasis occurs when the dilatation is caused by the fibrosis pulling the airway lumen. In my thesis, I solely qualify traction bronchiectasis for the following reasons: (i) Identification of traction bronchiectasis has less inter-observer variation compared to honeycombing. (ii) Compared to reticular patterns, traction bronchiectasis is based on the airways, a clear indefinable anatomical structure. Thus, avoiding misclassification errors with the pulmonary vessels [56]. (iii): The progression of traction bronchiectasis is strongly linked to lung function [58].

1.4.2.3 Current Challenges in CT Imaging

For radiological scoring of IPF, there exist computerized scoring systems such as CAILPER [59] and QLF [60] which links features on CT to the severity of IPF. However, there is no computerized analysis that tracks IPF progression across longitudinal CT scans solely in terms of traction bronchiectasis. Currently, monitoring of traction bronchiectasis across CT scans are limited to crude visual inspection and categorical labelling [58]. Thus, in this thesis, I address the limitation by proposing a quantitative measure based on the appearance of traction bronchiectasis. The analysis provides the following advantages: (i) Assuming an airway segmentation is

available, the quantification is automatic. (ii) The method provides an interpretable measurement as percentage volume change to qualify the progression of IPF.

1.5 Contribution & Thesis Outline

My contribution is developing computerized methods to solely quantify the dilatation of airways in bronchiectasis and IPF patients. Currently, digital quantification tools are based on using multiple features such as pulmonary arteries and lung parenchyma. This approach has several problems: (i) Some features are based on false assumption such as pulmonary artery remaining a constant shape. (ii) Certain features like reticular patterns are difficult to precisely segment. (iii) Scoring systems like Bhalla may not be sensitive at measuring subtle progression of the disease. I address these problems by proposing a tapering measurement and a novel method of detecting the most proximal point of dilatation along the airway track in longitudinal scans. The proceeding chapters are organised and summarizes as follows:

- In Chapter 2, I proposed a pipeline to acquire a novel tapering measurement using state of the art image processing methods. The measurement is the general trend between the airway arc length and the logarithmic cross-sectional area. I showed the clinical utility by applying the tapering measurement on airways affected by bronchiectasis.

- In Chapter 3, I quantified the accuracy of the tapering measurement by developing bespoke airway phantoms. The phantoms utilise different components of the pipeline in order to acquire accurate area measurements.

- In Chapter 4, I assessed the reproducibility of the measurement in relation to CT dose, voxel size and CT reconstruction algorithms. In addition, I analysed the effect of airway bifurcations on the taper measurement.

- In Chapter 5, I proposed a novel method using Bayesian changepoint analysis to changes in dilatations across longitudinal scans of airway affected by IPF.

Furthermore, in terms of clinical utility, I show the method could be used to measure volume changes in disease regions of IPF.

- Finally in Chapter 6, I summarise my contributions and propose possible future works.

Chapter 2

Airway Tapering Measurement

2.1 Abstract

The gold standard to diagnose and monitor bronchiectasis is accomplished by inspection of chest computed tomography (CT) scans. A clinician examines the broncho-arterial ratio to determine if an airway is brochiectatic. The visual analysis assumes the blood vessel diameter remains constant, although this assumption is disputed in the literature. In this chapter, I proposed a simple scalar measurement to quantify the tapering of a single airway track on CT. I defined an airway track as a path from the Carina to the most distal point observable on CT. To this end, I implemented a pipeline to measure the cross-sectional area of the airway at contiguous intervals. The tapering measurement is the gradient of the linear regression between area in logarithmic space and arclength of the airway track.

I showed the clinical utility by evaluating on three datasets. First, comparing the tapering of 35 healthy and 39 bronchiectatic airway tracks identified by an expert radiologist. Second, computing the tapering difference between 14 pairs of healthy airways in longitudinal scans. Third, computing the tapering difference in 5 pairs of healthy airways that became bronchiectatic. The first dataset showed bronchiectatic airways have a reduction in taper rate (mean 3.17×10^{-2} vs. 2.11×10^{-2} mm^{-1}, p = 7.1×10^{-7}). The second dataset showed a good agreement with ICC > 0.99 between the two sets and standard deviation of the tapering difference is $1.45\times10^{-3}\text{mm}^{-1}$. Finally, I found a statistical difference (p = 7.2×10^{-3}) in tapering difference be-

tween airways remaining healthy and airways becoming diseased. Our technique provides the potential for use in the diagnosis of bronchiectasis, and the assessment of progression of bronchiectasis over time.

2.2 Publications

The following content has originally appeared in the following publication:

- **K Quan**, R J Shipley, R Tanno, G McPhillips, V Vavourakis, D Edwards, J Jacob, J R Hurst, D J Hawkes, "Tapering analysis of airways with bronchiectasis." In *Proceedings of SPIE*, 2018.

In addition, the content has appeared in the following abstract:

- **K Quan**, J Jacob, R J Shipley, D J Hawkes, J R Hurst, "Airway tapering in bronchiectatic and healthy airways." *European Respiratory Journal*, 52: Suppl. 62, OA3793, 2018.

2.3 Introduction & Motivation

Various groups have proposed methods to automatically and semi automatically compute the BA ratio for bronchiectatic airways [61, 62, 63]. However, use of the BA ratio to diagnose bronchiectasis has two major flaws. First of all, the healthy range of the BA ratio can be 1.5 times size of the artery [64]. Second, blood vessels can change size as a result of various factors including altitude [65], age [66] and smoking status [67]. This conflicts with the assumption that the pulmonary artery is always at a constant size.

An alternative approach to diagnose and monitor bronchiectatic airways is to analyse the taper of the airways i.e. the rate of change in the cross-sectional area along the airway [12]. In patients with bronchiectasis, the airway is dilated and so the tapering rate must be reduced. Airway tapering is difficult to assess visually and to measure interactively from the images. As described by Hansell [64], the observer would have to make multiple cross-sectional area measurements along the airway. As mentioned in Cheplygina et al. [68], measuring multiple lumen is a manually exhaustive task and prone to mistakes.

2.3.1 Literature Review

There have been various strategies to quantify tapering in the airways. The initial proposed tapering measurements by Odry et al. [69] were restricted to short lengths of the airways. A segmented airway would be spilt into four equal parts. Each segment had a series of lumen diameter measurements taken along each branch. The tapering was measured as the linear regression of the lumen diameters along the branch. The method shared similarity to Venkatraman et al. [70], but the diameter measurements were taken across the central half of each branch. Various analyses attempted to measure the taper of airways containing multiple branches. In Oguma et al. [3] they measured the region of interest from the carina to the fifth generation airway, however this was only performed in patients with COPD. Finally, Weinheimer et al. [71] used a graphical model of the airways for their proposed tapering measurement. The graphical model was based on a graphical tree originating at the trachea and extending into distal branches, depending on airway bifurcations. A tapering measure was assigned to the edge of the graph depending on the lumen area and generation. They also proposed a scoring system based on a collection of tapering values within a lobe.

2.3.2 Contribution

The tapering measurements described above suffer from the following limitation. The region of interest for the tapering measurement was restricted to airways that were segmented using the respective airway segmentation software. Bronchiectasis is a heterogeneous disease - it can affect any area in the lung including the peripheral regions [29]. Thus, to encapsulate the disease in the tapering measurement, one would need to consider the region of interest as the entire airway, from the trachea to the most distal point.

My contribution addresses these limitations by proposing a measurement to describe the taper of the entire airways. The measurement is a scalar value to quantify the taper rate of a given airway track form the carina to the most distal point measurable on a CT image. In Section 2.4, I present a pipeline consisting of images analysis techniques to compute the taper measurement. In Section 2.5, I demon-

strate the potential clinical utility in two experiments. First, comparing taper measurements from healthy and bronchiectatic airways. Second, computing the change in taper rate form airways remaining healthy and airways that were healthy but became bronchiectatic. Finally, in Section 2.6 the advantages of choosing various digital processing methods for my pipeline.

2.4 Method

I first, describe in detail the steps to acquire the airway tapering measurement, summarised in Figure 2.1. The pipeline required two inputs. First, the most distal point of each airway of interest was identified. Secondly, a complete segmentation of the airway was produced. In this paper, an experienced radiologist (JJ) was used to identify and label the distal point. For each chosen airway, the radiologist manually tracked the airway to the most distal point visible on the image. The distal point was marked by a single voxel. When the airway was dilated at the periphery of the lung, the point at which it was judged to be at the end of the centreline was marked. The entire analysis was completed using ITK-snap[1].

I obtained an airway segmentation by implementing a method developed by Rikxoort et al. [72] The algorithm was based on a region growing paradigm. In summary, a wave front was initialised from the trachea. Voxels on each new iteration were classed as airways based on a voxel criterion. The wave front continued until a wave front criteria was met. In most cases, the airway segmentation was unable to reach the distal points and in these cases I extended the airway segmentation to the distal points by manual delineation.

2.4.1 Centreline

The centreline was used to identify and order the airway segments for the tapering measurement. I implemented a curve thinning algorithm developed by Palagyi et al. [73] At initialisation, the algorithm used the airway segmentation and distal points acquired in Section 2.4. The final input was the start of the centreline at the trachea. The shape of the trachea was assumed to be tubular, with an approximate

[1] `http://www.itksnap.org`, last accessed May 4, 2021

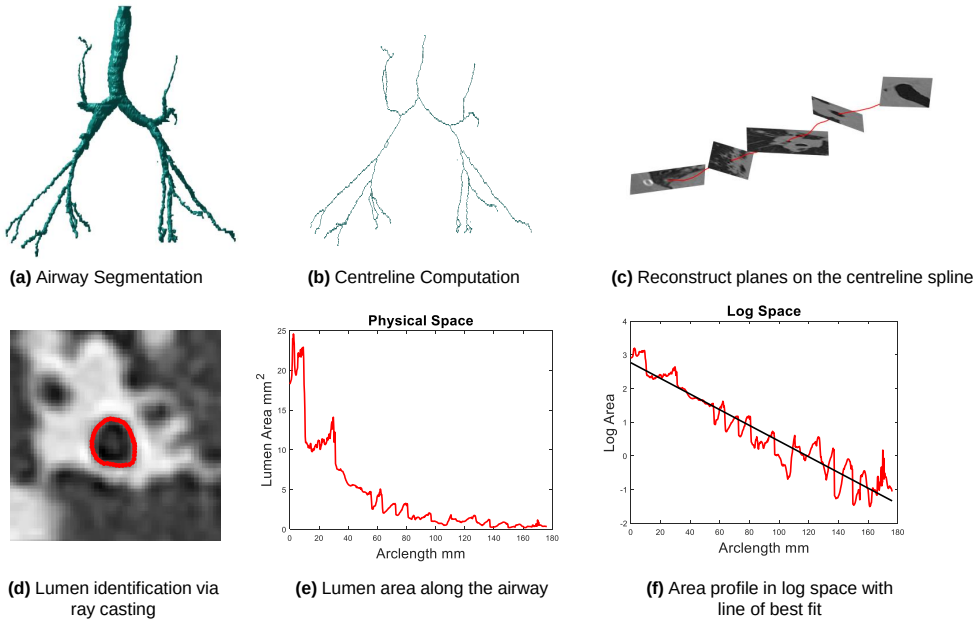

(a) Airway Segmentation **(b)** Centreline Computation **(c)** Reconstruct planes on the centreline spline

(d) Lumen identification via ray casting **(e)** Lumen area along the airway **(f)** Area profile in log space with line of best fit

Figure 2.1: Summary of steps in our pipeline

constant diameter and orientated near perpendicular to the axial slice as shown on Figure 2.2. Thus, the centreline of the trachea lay on the local maximum value of the distance transform of the segmented trachea [74]. Algorithm 1 was used to find the centreline start point.

Algorithm 1 Locating the start of centreline on the trachea

Input: $D_z(x,y)$, 2D Distance image on the zth axial slice. An example is shown on Figure 2.2.
Output: (x_s, y_s, z_s), Start point of trachea
$z \leftarrow$ First slice at the top of the trachea.
while $\max_{(x,y)} D_z < \max_{(x,y)} D_{z+1}$ **do**
  $(x_{max}, y_{max}) = \text{argmax}_{(x,y)} D_z$
  $z = z + 1$
end while
$(x_s, y_s, z_s) = (x_{max}, y_{max}, z)$

2.4.2 Recentring and Spline fitting

The next task was to separate the centreline of each individual airway from the centreline tree. To this end, I modelled the centreline tree as a graphical model similar to Mori et al. [75] The nodes corresponded to the centreline voxels and the

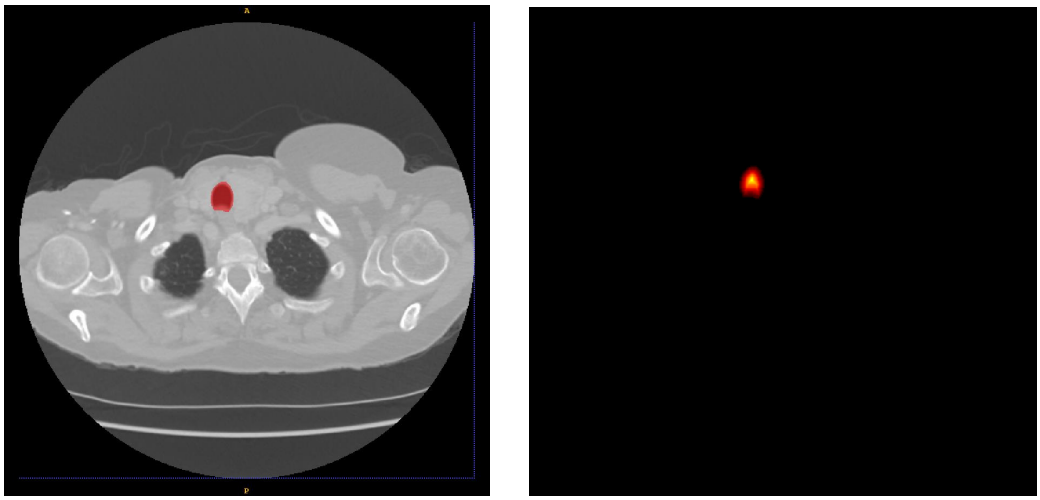

A B

Figure 2.2: A: An axial slice of a chest CT scan with a trachea segmentation. B: A distance transformation $D_z(x,y)$ of the same trachea segmentation. I used a local maximum as the start point of the centreline.

edges linked neighbouring voxels. I performed a breath first search algorithm [76] on the centreline image. Starting from the carina, I iteratively found the next set of sibling branches. When a distal point was found at the end of a parent branch, the path leading to the distal point was saved. The output was an array of ordered paths describing the unique route from the trachea to the distal point. The proposed tapering measurement started at the carina. Thus, centreline points corresponding to the trachea were removed from further analysis.

For each path I corrected for the discretization error - a process known as recentring [77]. I implemented a similar method to that described by Irving et al. [78] A five point smoothing was performed along each path. I modelled the centreline as a continuous model by fitting a cubic spline $F : [0, k_n] \rightarrow \mathbb{R}^3$ denoted as

$$F(t) = \begin{cases} f_1(t), & t \in [0, k_1] \\ \vdots & \\ f_i(t), & t \in [k_{i-1}, k_i] \\ \vdots & \\ f_n(t) & t \in [k_{n-1}, k_n] \end{cases}, \tag{2.1}$$

where $f_i(t) = \sum_{j=0}^{3} c_{i,j} t^j$ and $c_i \in \mathbb{R}^3$. The knots k_i where taken on every smoothed point on the centreline. The spline fitting was performed using the *cscvn*[2] function in Matlab. The continuous model should enable computations of the arc length and tangent at sub-voxel intervals along the airway.

2.4.3 Arc Length

The tapering measurement required an array of arc lengths at contiguous intervals from the carina to the distal point. For our pipeline, I considered small parametric intervals t_i on the cubic spline $F(t)$. At each interval t_i, I computed the arc length from the carina to t_i as described in Kreyszig [79]:

$$s(t_i) = \int_0^{t_i} \sqrt{\frac{dF}{dt} \cdot \frac{dF}{dt}} dt, \tag{2.2}$$

where $(\cdot)$ is the dot product. For our work, I considered parametric intervals of 0.25 units along the spline.

2.4.4 Plane Cross Section

I measured the cross-sectional area accurately by constructing a cross-sectional plane perpendicular to the airway. Using the interval t_i from the arc length computation, I computed tangent vector $q \in \mathbb{R}^3$ by

$$q(t_i) = \frac{\dot{F}}{|\dot{F}|}, \tag{2.3}$$

[2] `https://uk.mathworks.com/help/curvefit/cscvn.html`, last accessed on May 4, 2021

where $\dot{F} = \frac{dF}{dt}$.

From linear algebra, points on the plane can be generated by their corresponding basis vector [80]. To this end, I generated a set of orthonormal vectors $v_1, v_2 \in \mathbb{R}^2$ using the method stated in Shirley and Marschner [81]. The method is summarised in Algorithm 2.

Algorithm 2 Constructing the basis for the plane reconstruction, adapted from Shirley and Marschner [81].

Input: q Unit tangent vector of the spline
Output: v_1,v_2 Basis of the orthogonal plane
$a \leftarrow$ Arbitrary vector such that a and q are not collinear
$v_1 = \frac{a \times q}{|a \times q|}$
$v_2 = v_1 \times q$

Assuming $F(t_i)$ was the origin, each point $u \in \mathbb{R}^3$ on the plane can be written as:

$$u = \alpha_1 v_1 + \alpha_2 v_2. \tag{2.4}$$

I selected the scalars $\alpha_1, \alpha_2 \in \mathbb{R}$ such that the point spacing are 0.3mm isotropically.

2.4.5 Lumen Cross Sectional Area

I calculated the cross sectional area using the Edge-Cued Segmentation-Limited Forward Width Half Maximum (FWHM_{ESL}), developed by Kiraly et al. [82] The method is as follows: the cross-sectional planes were aligned on both the CT image and airway segmentation. The intensities of the plane were computed for both images using cubic interpolation. Fifty rays were cast out in a radial direction, from the centre of the plane. Each ray sampled the intensity of the two planes at a fifth of a pixel via linear interpolation. Thus, each ray produced two 1D profile with the first from the binary plane r_b, and second from the CT plane r_c. I then applied Algorithm 3 to find boundary point l.

The final output of the FWHM_{ESL} was an array of 2D points corresponding to the edge of the lumen. Finally, I fitted an ellipse based on the least square principle. The method was developed and implemented in Matlab by Fitzgibbon et al. [83] I considered the cross sectional area as the area of the fitted ellipse.

Algorithm 3 Summary of the FWHM_{ESL}, adapted from Kiraly et al. [82]. The purpose of the algorithm was to find the point of the ray which crossed the lumen.

Input: The rays: $r_b : [0,p] \rightarrow \mathbb{R}_{[0,1]}$, $r_c : [0,p] \rightarrow \mathbb{R}$ where p is the length from the centre to the border of the plane.
Output: The position of the lumen edge, l.
$s \leftarrow$ The first index of the ray such that $r_b(s) < 0.5$
$I_{max} \leftarrow$ Local maximum intensity in r_c nearest to s
$x_{max} \leftarrow$ The index such that $r_c(x_{max}) = I_{max}$
$I_{min} \leftarrow$ Minimum intensity in r_c from 0 to x_{max}
$x_{min} \leftarrow$ The index such that $r_c(x_{min}) = I_{min}$
$l \leftarrow$ The index such that $r_c(l) = (I_{max} + I_{min}) \times 0.5$ and $l \in [x_{min}, x_{max}]$

2.4.6 Tapering Measurement

I assumed for a healthy airway that the cross-sectional area was modelled by an exponential decay along its centreline. It has been shown in human cadaver studies that the average cross section area in a branch reduces at an exponential rate at each generation [84]. The same observation has been also observed in porcine models [85]. Using the decay assumption, I modelled the relationship between the arc length and the cross-sectional area as

$$y = Tx + \log A, \tag{2.5}$$

where x is the arc length of the spline, T is the proposed tapering measurement, y is the cross-sectional area and A is an arbitrary constant.

In terms of implementation, for each airway track. I considered the array arc length and cross-sectional area computed for each individual airway. A logarithmic transform $\log(x)$ was applied only on the cross-sectional area array. I fitted a linear regression on the signal, the tapering measurement is defined as the gradient from the line of best fit.

2.5 Evaluation & Results

I demonstrate the utility of my tapering measurement for diagnosing and monitoring bronchiectasis by using 3 datasets. First, a set of healthy airways (n = 35) and a set of bronchiectatic airways (n = 39) from 10 scans. The selection of bronchiectatic

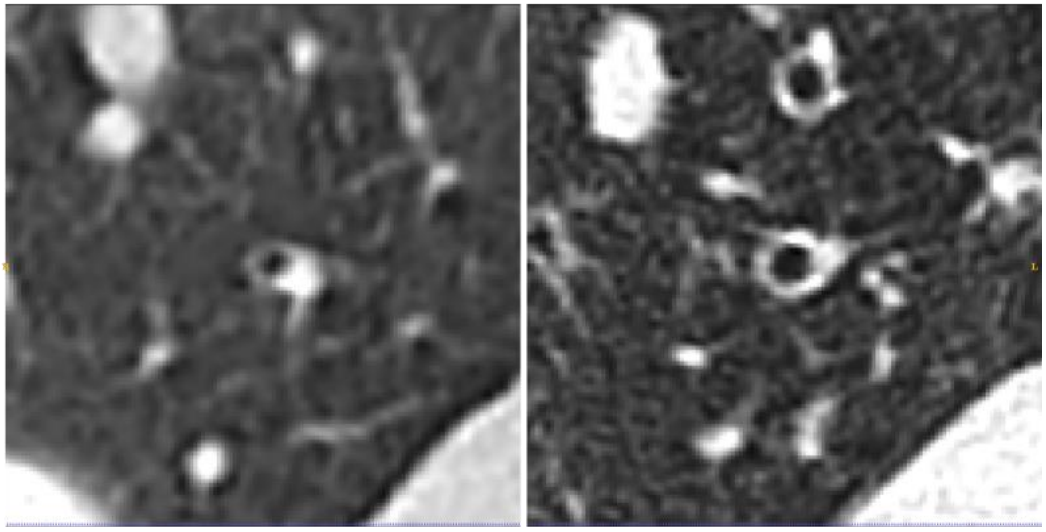

Figure 2.3: The same pair of airways from longitudinal scans. LEFT: Initial healthy airway. RIGHT: The same airway at the same location becoming bronchiectatic.

airways were based on clear dilatation along the airways. Diseased airways that contained mucus or had airway wall thickening were excluded from the study. Second, a set of healthy pairs of airways (n = 14) from 3 longitudinal scans. Third, a set of airways (n = 5) from a single pair longitudinal scan, where the airways were healthy on the initial scan but become bronchiectatic on the second scan. An example is displayed on Figure 2.3. All airways were selected by an experienced radiologist. The image properties of the first dataset are displayed on Table 2.1. The images properties of the second and third dataset are displayed on Table 2.2.

2.5.1 Tapering in Healthy and Bronchiectatic Airways

Figure 2.4 compares the tapering measurement between healthy and diseased airways. On a Wilcoxon Rank Sum Test between the populations, $p = 3.4 \times 10^{-4}$. The difference between the mean of the two populations was 0.011mm^{-1} and difference between the medium of the two population was 0.006mm^{-1}. In addition, with receiver operating characteristic (ROC) analysis shows the area under curve, AUC = 0.84.

2.5.2 Tapering Change in Longitudinal Scans

I compared the change in taper measurement in healthy airways across longitudinal scans. The results are displayed as a Bland-Altman graph on Figure 2.5. The

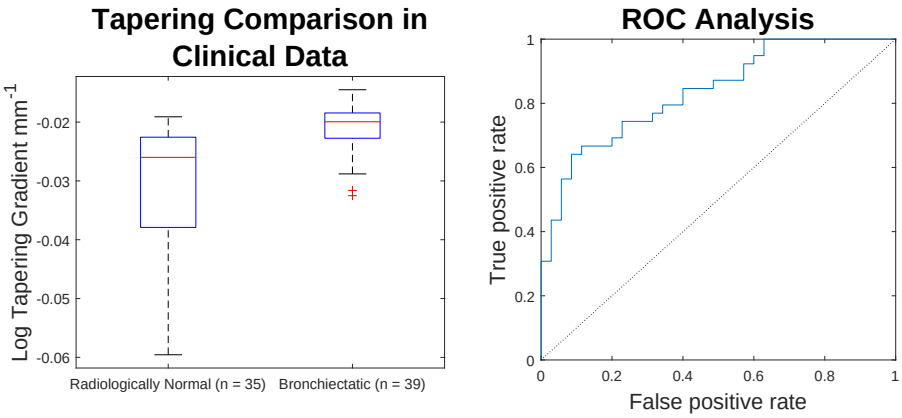

Figure 2.4: LEFT: Comparing the proposed tapering measurement with labelled healthy and bronchiectatic airways. On a Wilcoxon Rank Sum Test between the populations, $p = 3.4 \times 10^{-4}$. RIGHT: ROC curve on the same data. On the graph, the dotted line is the identity line. For the area under the curve; AUC = 0.84

Patients	Bronchiectatic Airways	Healthy Airways	Scanner	Kernel	Voxel Size (x,y,z) mm
bx500	0	9	Toshiba Aquilion ONE	FC18	0.67, 0.67, 1.50
bx503	15	5	Toshiba Aquilion ONE	FC56	0.64, 0.64, 1.50
bx504	0	8	Toshiba Aquilion ONE	FC56	0.78, 0.78, 1.50
bx505	5	0	Toshiba Aquilion ONE	FC51	0.75, 0.75, 0.80
bx507	0	4	Toshiba Aquilion ONE	FC18	0.63, 0.63, 1.50
bx508	1	0	GEMD CT750 HD	STANDARD	0.80, 0.80, 1.00
bx511	0	6	Toshiba Aquilion ONE	FC56	0.78, 0.78, 1.50
bx512	1	0	GEMD CT750 HD	BONEPLUS	0.69, 0.69, 1.00
bx513	1	3	Toshiba Aquilion ONE	FC56	0.73, 0.73, 1.50
bx515	16	0	Toshiba Aquilion ONE	FC18	0.78, 0.78, 1.50

Table 2.1: List of CT images used for the experiment. The table includes the number of classified airways, scanner, kernel and voxel size. Abbreviation: GEMD - GE Medical Systems Discovery.

Dataset	Patients	BL CT Scanner	BL Voxel Size	FU CT Scanner	FU Voxel Size	Airways	TBS
2	bx500	Toshiba Aquilion One	0.67, 0.67, 1.00	Toshiba Aquilion One	0.56, 0.56, 1.00	6	9M 6D
2	bx504	Toshiba Aquilion One	0.63, 0.63, 1.00	Toshiba Aquilion One	0.78, 0.78, 1.00	7	35M 6D
2	bx510	GEMS LightSpeed Plus	0.70, 0.70, 1.00	Philips Brilliance 64	0.72, 0.72, 1.00	1	5M 22D
3	P1	GEMS Discovery STE	0.86, 0.86, 2.50	Siemens SD AS	0.67, 0.67, 1.50	5	12M 7D

Table 2.2: List of make, models and voxel sizes of CT images for progression experiment. The voxel sizes are displayed as x,y,z and in mm units. Abbreviation: GEMS - GE Medical Systems, BL - Baseline Scan, FU - Follow-up scans, TBS - Time between scans, SD -SOMATOM Definition.

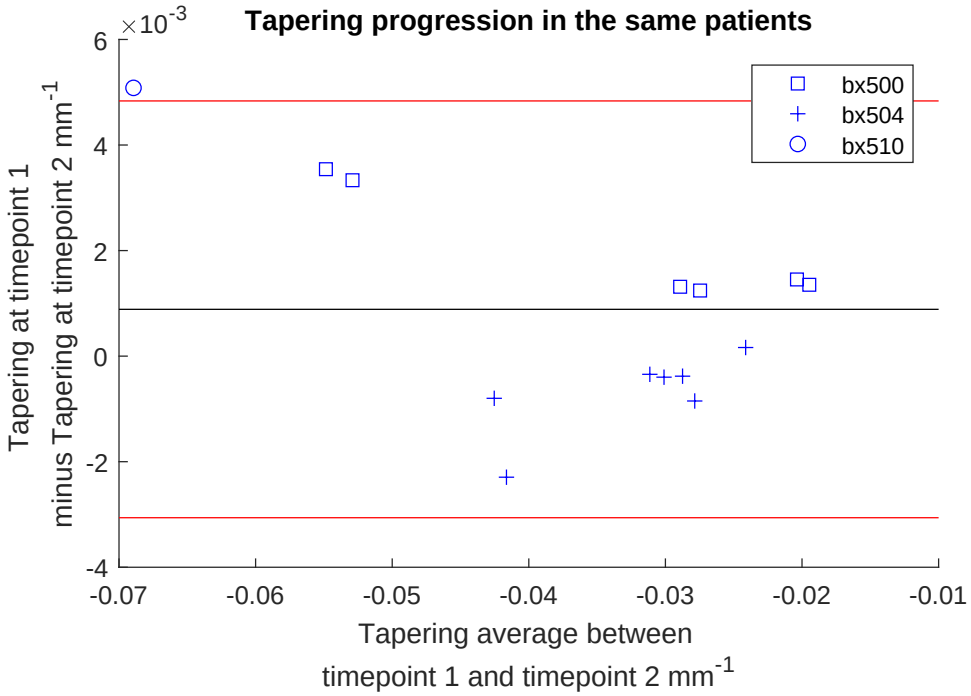

Figure 2.5: Bland-Altman [1] graph comparing tapering measurement on the same airways from the first and subsequent scan, $ICC > 0.99$.

95% confidence interval in taper difference was $\pm 4.0 \times 10^{-3}\text{mm}^{-1}$, the confidence interval was less than the average difference between healthy and bronchiectatic airways, described in Section 2.5.1. The results demonstrated good agreement with an intraclass correlation coefficient [86] $ICC > 0.99$. The standard deviation of the tapering difference was $1.45 \times 10^{-3}\text{mm}^{-1}$.

Finally, I compared the taper rate change between airways remaining healthy and airways that became the bronchiectatic. The metric used for comparison was the difference in tapering i.e. the taper rate of the initial scan minus the taper rate on the subsequent scan. Figure 2.6, shows the tapering change between airway pairs remaining healthy and airway pairs that were initially healthy but became bronchiectatic. The comparison shows statistical difference between the two populations, on a Wilcoxon Rank Sum Test between the populations, $p = 7.2 \times 10^{-3}$. In addition, the diseased airway pairs showed greater change in magnitude compared with the controlled airway pairs.

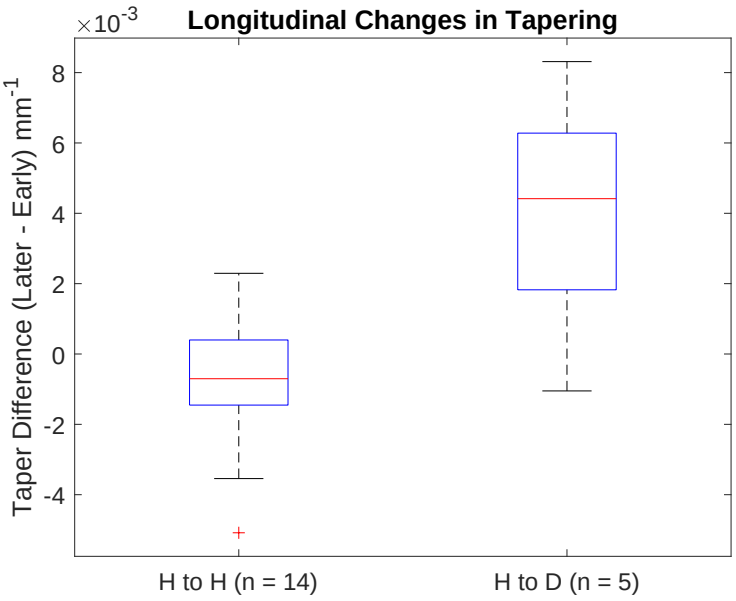

Figure 2.6: Comparing the change in taper rate between airways remaining healthy and airways that were healthy and became bronchiectatic.The time period between taper rates are displayed in Table 2.2. On a Wilcoxon Rank Sum Test between the populations, $p = 7.2 \times 10^{-3}$.

2.6 Discussion

In this chapter, I proposed a tapering measurement for airways imaged using CT and validated the reproducibility of the measurement. The tapering measurement is the exponential decay constant between cross-sectional area and arclength from the carina to the distal point of the airway. To compute the taper measurement, I constructed a pipeline consisting of various established image processing algorithms. The steps include centreline computation, orthonormal plane reconstruction and area lumen measurement.

The pipeline consists of various established image processing algorithms. I chose the centreline algorithm developed by Palagyi et al. [73]. Unlike other proposed methods [74, 87, 88] the algorithm explicitly links the distal points to the carina. Furthermore, it has been shown that the algorithm of Palagyi et al. [73] can be used on images with non-isotropic voxel sizes [78]. By modelling the centreline as a graphical model similar to Mori et al. [75], I performed a breadth first search [76] to avoid analyses of false airway branches. The removal of false branches is

not a trivial task [75, 78, 89].

I corrected the centreline discretisation error or recentring by smoothing points on the centreline. Smoothing has been an established method in the literature [78, 90]. A recentring method was proposed by Kiraly et al. [89] which shifts the centreline voxels in relation to a distance transform. The process is iterative compared to a single computation of smoothing.

For our pipeline, I generated the orthonormal plane based on the method of Shirley and Marschner [81]. Other methods have been proposed. In Kreyszig [79], they generated a binormal and principle normal. However, the method is not robust as the binormal vector can become a zero vector. Grelard et al. [91] used Voronoi cells, a method that requires two parameters whereas Shirley and Marschner [81] is parameter free. For our work, intensities on the cross-sectional plane were computed via cubic interpolation. Various papers have used linear interpolation [92, 82, 93]. However, it has been shown by Moses et al. [94] that the method can create high frequency artefacts in the image [95].

Various methods have been proposed to measure the area of the airway lumen [96, 97, 98]. I used the FWHM_{ESL} because of two distinct advantages. First, the method is parameter free. Second, the method is robust against slight variations in intensities [82]. The method can therefore be applied to images from different scanners and using different reconstructions.

Part of the evaluations consist of analysing the difference in tapering across longitudinal scans. The timescales between scans ranges from 9 to 35 months. The motivation for a long timescale is a proof of principle demonstration that the tapering measurement is reproducible for clinical studies. Examples include, drug trials [99] and investigations in exacerbations [100], where the timescales in monitoring patients were 12 months and 60 months respectively.

2.6.1 Limitation

In this study, I compared the tapering measurement for healthy and diseased airways using a Wilcoxon Rank Sum Test. The test assumes the data points are independent. However, we used a variety of airways from the same lung. Thus, the tapering

profiles of the same patients will have a degree of overlap. Future work is needed to analyse data points that are not dependent on each other.

In the study, all diseased airways were chosen on an ad hoc basis. The criteria for selection was a clear dilatation of the inner lumen without mucus or with airway wall thickening. In addition, the airways were selected independently from lobe location or defined cylindric, varicose or cystic appearance as described in Cantin et al. [101]

A key limitation of the tapering measurement is the requirement of having a robust airway segmentation. In this paper, the airway segmentation software was often unable to reach the visible distal point of an airway. Thus, time-consuming manual delineation was needed to extend the missing airways. The distal point is usually located at the periphery of the lungs. Thus, to avoid manual labelling, a segmentation algorithm would need to automatically segment the airways past the sixth airway generation. From the literature, the state of the art software developed by Charbonnier et al. [102] using deep learning could still only consistently segment airways to the fourth bifurcation. The segmentation of small and peripheral airways is not a trivial task [94, 103, 104].

2.7 Conclusion

I demonstrated the clinical utility of the tapering measurement through comparing the taper rate of a set bronchiectatic and healthy airways. I show a statistical difference between the two population and the magnitude of tapering in healthy airways is greater than the diseased set. The observation concurs to the hypothesis that disease airways retains a larger cross sectional area along the arc length. The results shows potential towards distinguishing between bronchiectatic and healthy airways.

I considered clinical utility in of my propose tapering measurement on longitudinal scans. I computed the difference in taper rates in pairs of healthy airways. The results show changes in normal airways on Figure 2.5 do not overlap between healthy and diseased airways identified by a radiologist on Figure 2.4. Furthermore, I showed a statistical difference between changes in taper rates in airways initially

healthy but became bronchiectatic to controls. Thus, as a proof of principle experiment I showed the measurement could potentially be use to track and monitor airways becoming bronchiectatic.

I further developed and validated the analysis of the taper measurements in the following chapters. In Chapter 3, I will quantify the accuracy of the proposed tapering measurement. In Chapter 4, I present methods to assess the precision and reproducibility of the tapering measurement.

Chapter 3

Accuracy of the Image Analysis Components that Form the Airway Tapering Analysis System

3.1 Abstract

In Chapter 2, I proposed a pipeline to compute an airway taper measurement. To obtain the taper rate, I require a series of contiguous cross-sectional area measurements. To compute the area, I need to perform centreline computation, centreline recentring and generating cross-sectional planes. Each stage can affect the accuracy of the computed area. In this chapter, I quantified the accuracy of my pipeline in acquiring contiguous cross-sectional area measurements. To this end, I used a phantom with calibrated 3D printed structures. To encapsulate, different morphologies of the airways, the printed tube structures differ in diameter, curvature and linear area change.

Results showed my pipeline is accurate to measuring cross sectional area to sub voxel level scale for diameters above 1.1mm. I showed the accuracy is independent of curvature and can be used to measure linear trends along tubular structures in CT. Our results showed the pipeline is robust to a range of airway morphologies. Thus, verifying the accuracy of my tapering measurement.

3.2 Publications

The following content has originally appeared in the following publication:

- **K Quan**, R J Shipley, R Tanno, G McPhillips, V Vavourakis, D Edwards, J Jacob, J R Hurst, D J Hawkes, "Tapering analysis of airways with bronchiectasis." In *Proceedings of SPIE*, 2018.

3.3 Introduction & Motivation

As stated in Section 2.4, a key input of my tapering measurements is an array of cross-sectional areas measurements along the airway. The accuracy of the tapering measurement is dependent on the accuracy and robustness of acquiring lumen area measurements. To compute area measurements, various image processing algorithms were used including centreline computation, centreline recentring and generating cross-sectional planes. Such methods can affect the accuracy of area measurement [77, 87, 94]. In addition, the pipeline is required to take hundreds of cross-sectional area measurements along vessels that can change size and tortuosity. Thus, it is necessary to quantified the accuracy of my pipeline against differing morphologies of the vessel.

3.3.1 Literature Review

One common method to validate the accuracy of airway lumen measurement are through in-silico images [24]. However, for more realistic simulations of the airways, various groups have used physical phantoms. The phantom consists of two parts: First, the airways are represented by non-metallic hollow tubes with varying diameters [20, 96, 105]. Second, padding materials such as foodstuff [98, 106] or polyurethane foam [20, 107] are used to surround the tubes. These materials are used to simulate surrounding lung parenchyma. In most experiments phantoms were scanned with tubes perpendicular to the axials slice [20, 96, 105]. The experiments were extended by Oguma et al. [108] and Hasegawa et al. [107] where the tubes were tilted such that lumen appeared elliptical on the CT axial slice. Finally, Achenbach et al. [109] used porcine lungs to assess the accuracy of their airway

quantification algorithm. The ground truth were obtained by freezing the lung after scanning and obtaining histological slices.

3.3.2 Contribution

In previous experiments, two factors were not assessed in detail: First, area measurements were not taken on a connected vessel with a narrowing lumen. Second, the area measurements were not taken at contiguous intervals.

The contribution of this chapter is to quantify the accuracy of my proposed lumen area measurement using a phantom airway with differing morphologies. The morphologies were chosen such that to obtain accurate cross-sectional area at contiguous intervals, it will utilise all the steps in my pipeline. The layout of the chapter is as follows: In Section 3.4, I describe methodology to generate the airway phantom using 3D printing. In Section 3.5, I showed results of cross-sectional area results on a range of morphologies. In Section 3.6, I discussed the results and experiments.

3.4 Method

My methodology followed a similar experimental setup to Wiemker et al. [110]. In Section 3.4.1, I discussed the construction of my phantom using 3D printing. In Section 3.4.2, I discuss verification of the accuracy of the 3D printed structures using a micro CT scanner.

3.4.1 Phantom Experiment

The aim of the phantom was to have a ground truth to assess the accuracy and precision of the pipeline. The design of the phantom was to encapsulate various morphologies of the airway lumen. To this end, the airway lumen structures were built using 3D printing.

3.4.1.1 Phantom Design

The body of the phantom was a cylindrical Perspex case, 240mm in diameter. A set of 3D printed structures was attached on the flat side of the cylinder. The remaining space was filled with rice to approximately mimic the attenuation properties of lung

Tube Number	Narrowing Gradient t	Start Diameter/mm	End Diameter/mm
1	0.051	2.5	5.1
2	0.083	2.5	6.7
3	0.109	2.5	8.0
4	0.132	2.5	9.1
5	0.168	2.5	10.4

Table 3.1: The parameters of each tube in the narrowing phantom.

parenchyma. A similar material was used by Robinson et al. [106] for the same effect.

I designed the 3D printed structures to simulate various morphologies based on the appearance of airways in CT. Three parameters were used; diameter, radius of curvature and narrowing. Each structure consists of 5 tubes attached to a circular base, with wall thickness 1.7mm and length 50mm. The designs are displayed in Figure 3.1. All structures were made using an EnvisionTEC ULTRA 3SP printer with the ABS 3SP Tough resin. The voxel resolution ranges from 0.05mm to 0.1mm. The resolution was set to the lowest possible setting. The supporting structure was set at the base of the tubes.

The diameter lumen consist of tubes of diameters: 1.1mm, 2.5mm, 3.9mm, 5.3mm, and 6.7mm. The curvature lumen consists of 2.5mm diameter tubes with its centreline radius of curvature of 30mm, 25mm, 20mm, 15mm, and 10mm. For the narrowing structures, I used the linear change in diameter along the tube. All narrowing tubes started at 2.5mm at the tip and diameter d along the tube was calculated as:

$$d = 2.5 + zt, \tag{3.1}$$

with centreline arc length z and narrowing gradient t. The diameter gradient varies with each tube, as shown on Table 3.1. I chose parameters through visual inspection of the CT image and cadaver experiments from the literature [84].

3.4.1.2 Image Acquisition and Post Processing

The phantom was imaged in a Toshiba Aqulilion ONE CT scanner at the Royal Free Hospital. The image voxel size were 0.625mm by 0.625mm by 1mm and re-

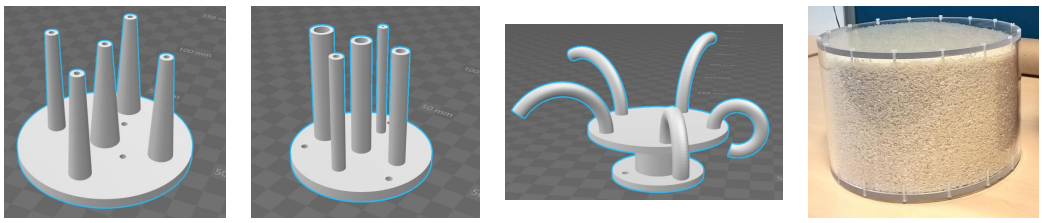

Figure 3.1: FAR LEFT: Different narrowing lumen. CENTRE LEFT: Different lumen diameter. CENTRE RIGHT: Different lumen centreline curvatures. FAR RIGHT: Physical phantom.

constructed using the Lung kernel. To test the pipeline, every tube was segmented using SegEM[1] with manual corrections. The endpoints were semi-manually demarcated using the centre of mass [111] of each segmented tube.

3.4.2 3D Printer Analysis

The scale of the CT image is sub-millimetre, thus, I verified the precision and accuracy of the 3D printer. To this end, two airways were manufactured, both with a nominal lumen diameter of 2.5mm - one 3D printed and another from a lathe. The milled lumen had a tolerance of 0.05mm.

Both lumens were micro CT scanned consecutively. The scanner was a Skyscan 1172 with a voxel size of 11.0μm isotropically. The large image size made it difficult to perform any post-processing. Thus I downsampled the images to 22μm isotropically with Sinc interpolation.

To avoid computing the centreline, the lumen needed to be perpendicular to the in-plane slice. To this end, the lumen was initially semi-manually segmented with SegEM. The misaligned angles was computed through the centre of mass of the segmented lumen. The image was then rotated with the misaligned angles with Sinc interpolation. Finally, in the realigned image, the lumen was semi-manually segmented using SegEM.

[1] `http://cmictig.cs.ucl.ac.uk/wiki/index.php/Seg_EM`, last accessed on May 4, 2021.

3.5 Results

I present the results in two sections. First, in Section 3.5.1, I established the ground truth of the 3D printed structures from the micro CT scan. Second, in Section 3.5.2, I showed the measurement acquired from the 3D printed structures.

3.5.1 Micro CT

The micro CT scanned images of the milled and 3D printed lumens are displayed in Figure 3.2. The 3D printed lumen contained abnormalities in the structure. Errors include holes and jagged surface indicated by the yellow and red arrows respectively.

Diameter measurements were taken 449 times in each slice from the tip to the base of the lumen. Figure 3.2, shows a systematic underestimation of the 3D printed lumen compared to the milled counterpart. The outliers were located near the ends of the lumen. The outliers were removed by only considering two-thirds of the lumen starting at the midpoint and expanding in both directions. I define mean difference between the inner lumen of the milled and 3D printed diameters as the offset error, and was calculated as 0.38mm.

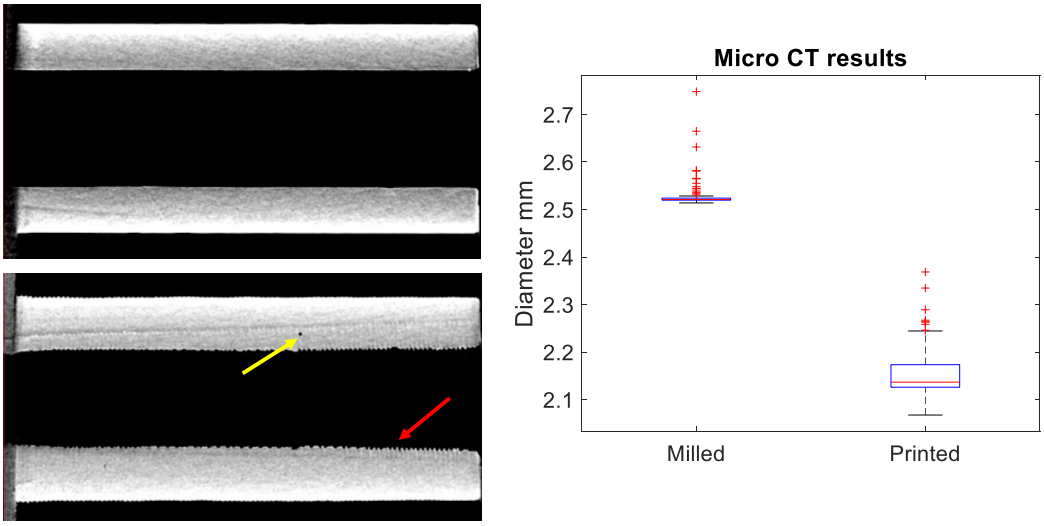

Figure 3.2: TOP LEFT: Slice of the 2.5mm diameter lumen made from a lathe. BOTTOM LEFT: Slice of the 2.5mm diameter lumen made using the 3D printer. The yellow arrow shows a hole within the resin. The red arrow shows the jagged surface. RIGHT: A box plot comparison of diameters between the milled and 3D printed lumens.

3.5.2 Clinical CT

I present the diameter measurements from each of the 3D printed structures. However, I first corrected the offset error found in Section 3.5.1. To this end, I added 0.38mm to every diameter measurement from the clinical CT phantom.

For the differing diameter lumen, Figure 3.3 shows the accuracy was at sub voxel level for diameters above and equal to 2.5mm. In the 1.1mm lumen, there is a significant overestimation by approximately 0.8mm. In terms of precision, the error range for each lumen was within 0.3mm and therefore at sub voxel level. When the measured diameters were plotted against the ground truth without calibration, there is an offset of -0.44mm in the line of best fit.

For the differing curvature lumen, Figure 3.3 shows the pipeline is accurate to sub voxel level. The mean error difference was within 0.2mm and the interquartile range was within 0.2mm for all curvatures. Thus the pipeline is precise to the sub voxel level and the precision is independent of the orientation of the lumen.

For the differing narrowing lumen, I computed the narrowing gradient from the image. The diameter measurements were plotted against the centreline length of the tube, starting from the base. Next, the diameter gradient was taken as the gradient of the linear regression of the plotted data. Figure 3.3, shows good correspondence between the measured and ground truth diameter gradient. The correlation coefficient was $r > 0.99$.

3.6 Discussion & Conclusion

This chapter presents a set of experiments to quantify the accuracy of the pipeline. To this end, we developed a phantom with calibrated 3D printed structures. The phantom were designed such that my proposed pipeline had to utilised various components to achieve an accurate measurement. I showed the pipeline can measure diameters accurate to 0.3mm – independent of orientation. As expected, the accuracy was reduced when the size of the lumen was near the voxel size of the image. From Figure 3.3, the pipeline can measure a range of linear changes along the centreline of the vessel.

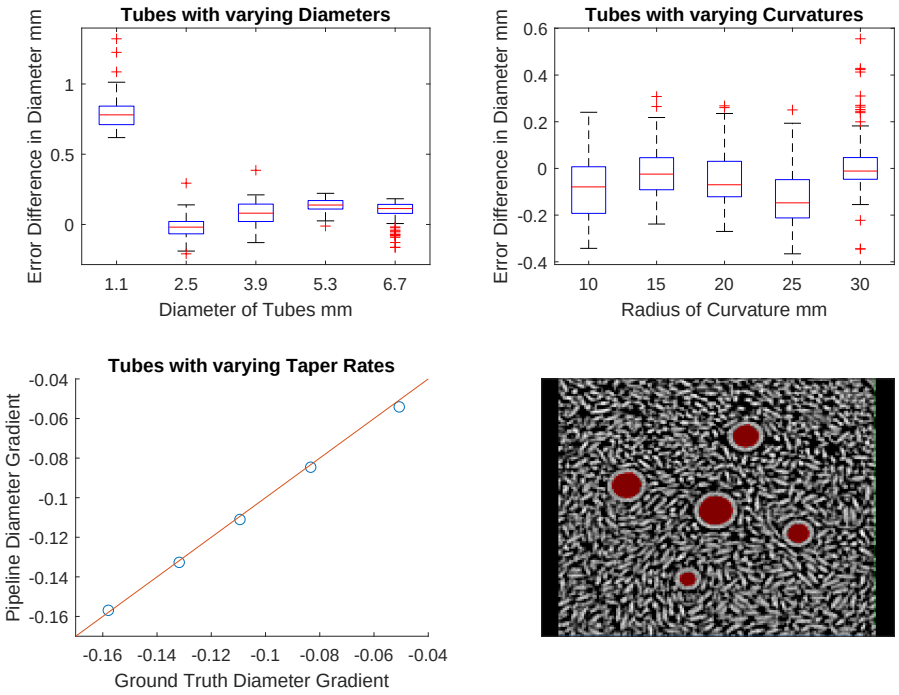

Figure 3.3: TOP LEFT: The diameter error difference when measuring the five tubes of varying diameters. TOP RIGHT: The diameter error difference when measuring the five tubes of varying curvatures. All tubes have a diameter of 2.5mm. BOTTOM LEFT: Relationship between the computed diameter gradient and its corresponding ground truth on the narrowing lumen with the identity line. BOTTOM RIGHT: A slice of the narrowing lumen, with the segmentation indicated in red.

In this chapter I showed at contiguous intervals, the area measurements are accurate to sub voxel scale. Furthermore, I showed the accuracy is independent of curvature and changes in area along the vessel. My tapering measure considers the general trend of hundreds of area measurement. Thus, I can infer that the taper measurement is highly accurate and the accuracy is independent to the complex morphologies of the airway tack.

In this work, I used a micro CT scanner without detailed calibration. As stated in Kagadis et al. [112], geometric calibration of a scanner ensures the signals is related to the image. The method involves scanning a phantom and setting the CT reconstruction to map pixels on the detector to the voxels in the image [113]. I believe the errors caused by any miscalibration are negligible as there is an logarithmic difference between the errors of interest in CT at a magnitude of 0.1mm and

errors in micro CT miscalibration at a magnitude of 0.01mm.

In the post-processing of the clinical CT results (Sec. 3.5.2), I assume an offset error of 0.38mm to the airway lumen, the error is similar to those reported in the literature [114]. Future work is required to establish if errors from 3D prints are multiplicative or offset errors. For my work, we assumed an offset error as I verified a single sized lumen. Furthermore, the errors of 3D printed lumen reported in Matsumoto et al [114] are within a magnitude of 0.38mm.

In the next chapter, I investigate the precision and reproducibility of my taper measurement. I will compute the tapering measurement against different CT acquisitions parameters. Finally, I will examine the effect of bifurcations on the tapering measurement.

Chapter 4

Precision of Tapering Measurement

4.1 Abstract

In Chapter 2, I proposed a tapering measurement for clinical utility of airways affected by bronchiectasis. In this chapter, I extended the work by showing the measurement is applicable for images acquired in a clinical environment. To this end, I quantified the reproducibility of tapering measurement against differing acquisition parameters. For this work, I performed 3 set of experiments: First, I compute the tapering measurement using 74 airways from 10 CT scans with differing radiation doses and voxel sizes. Second, on a subset of the same data, I compared the tapering measurement on airways taken from two different reconstruction kernels. Third, on a selected set of airways, I analysed how bifurcations affects the reproducibility of the tapering measurements.

Results showed in simulated low dose scans, the tapering measurement retained a 95% confidence interval of $\pm 0.005\text{mm}^{-1}$ in a 25 mAs scan. In simulations assessing different voxel sizes, the tapering measurement retained a 95% confidence of $\pm 0.005\text{mm}^{-1}$ up to 1.5 times the original voxel size. The tapering shows good correspondence with $r > 0.99$ when comparing tapering measurements against reconstruction kernels (n=44) and bifurcations regions (n=19). In conclusion, I have established an estimate of the precision of the tapering measurement and estimated the effect on precision of simulated voxel size and CT scan dose. I recommend that the scanner calibration be undertaken with the phantoms as described, on the

specific CT scanner, radiation dose and reconstruction algorithm that is to be used in any quantitative studies.

4.2 Publications

The following content has originally appeared in the following publication:

- **K Quan**, R J Shipley, R Tanno, G McPhillips, V Vavourakis, D Edwards, J Jacob, J R Hurst, D J Hawkes, "Tapering analysis of airways with bronchiectasis." In *Proceedings of SPIE*, 2018.

- **K Quan**, R Tanno, R J Shipley, J S Brown, J Jacob, J R Hurst, D J Hawkes "Reproducibility of an airway tapering measurement in computed tomography with application to bronchiectasis" In *Journal of Medical Imaging*, 2019.

4.3 Background

Quantification of the reproducibility of the tapering measurement is clinically useful as it allows statistical testing between measurements taken from different scanners and scanner parameters. Thus, extending clinical applicability of my proposed measurement to scanners that lack calibration and low dose scans.

4.3.1 Literature Review

Obtaining the cross-sectional area is a necessary input for computing the tapering measurement. There have been various analyses attempting to validate the reproducibility and precision of measurements against dose [115, 116], voxel size [96] and reconstruction kernel [117, 118, 119]. In most of the validation experiments, area measurements were taken from phantom [117, 118] or porcine [115, 116] models. In Fetita et al. [120], they used synthetic models of the lung. None of these experiments were explicitly performed on scans with bronchiectasis. Furthermore, the area measurements were not taken at contiguous intervals along the lumen thus missing possible dilatations from a bronchiectatic airway.

In the literature, investigations of the repeatability of arc length computation in airways are limited. In Palagyi et al. [73] they used simulated rotation of in vivo

scans. The assessment of repeatability was based on the lengths of a single branch rather than multiple generations of branches, thus precluding the repeatability of length quantification from the carina to an airway's most distal point.

4.3.2 Contribution

In all the proposed tapering measurements described in Section 2.3.1, there is no detailed quantification of the reproducibility when considering differences in specifications of the CT scanner, or reconstruction kernel, making it difficult to compare tapering statistics from two different CT scanners or from the same CT scanner but with different scanning parameters.

The contribution of this chapter is to quantify the reproducibility of my proposed tapering measurement under various acquisition and anatomical parameters. The chapter is organised as follows: Section 4.4 describes a set of methods to acquire images with varying dose, voxel size, reconstructions kernels. In addition, I constructed a protocol to assessed the effect of including region of airway bifurcations within in the taper measurement. In Section 4.5, I present the results of the reproducibility experiments on the tapering measurements and its constituent components: arclengths and cross-sectional areas. Finally, in Section 4.6, I discussed the clinically utility of the tapering measurements in light of these experiments.

4.4 Methods

The methodology is presented as follows, I applied my tapering measurement on a range of images with different parameters: First, in Section 4.4.1, I undertake silico simulations of differing dose and voxel sizes. Second, in Section 4.4.2, I acquired images with differing reconstruction kernels directly from the CT scanner. Third, in Section 4.4.3, I removed the bifurcation regions on airway tracks.

4.4.1 Simulated Images

I assessed the reproducibility of the tapering measurement experiment with in silico simulations of varying radiation dose and voxel sizes. For both experiments I used the entire dataset as described in Section 2.5.

```
function noisySlice = AddingDoseNoise(axialSlice,lambda)

%Creating the sinogram
sinogram = radon(axialSlice,0:0.1:179);

%Adding the Gaussian Noise
noisySinogram = sinogram + randn(size(sinogram))*10^lambda;

%Converting the noisy sinogram into physical space using Filter Backprojection
noisySlice = iradon(noisySinogram,0:0.1:179,length(axialSlice));

%Converting into integer precision intensities
noisySlice = uint16(noisySlice);

end
```

Figure 4.1: The Matlab code used simulate noise from differing doses.

4.4.1.1 Dose

To simulate the images acquired with different radiation doses, I used the method adapted from Frush et al. [121], I performed a Radon transform on each axial slice of the original CT image. The output is a sinogram of the respective axial slice. To simulate different radiation doses, Gaussian noise was added on each sinogram with standard deviation $\sigma = 10^{\lambda}$; with a range of λ. The noisy sinograms were then transformed back into physical space using the filtered back projection. The final output is a noisy CT image in Hounsfield units in integer precision. A Matlab implementation is displayed on Figure 4.1. For our experiment I varied λ from 0.5 to 5 in increments of 0.5. An example of the output image are displayed in Figure 4.2.

To relate λ to the physical dose from a CT scanner, I adopted the method described in Reeves et al. [22] This paper quantified the dose of an image with a homogeneous region in the chest CT scan. To this end, I used the homogeneous region inside the trachea. Using the airway segmentation, I considered the first 60 axial slices of the segmented trachea. To avoid the influence of the boundary, the tracheas were morphologically eroded [122] with a structuring element of a sphere of radius 5. All segmentations were visually inspected before further processing. Finally, I computed the standard deviation of the intensities inside the mask, denoted as T_n. Table 4.2, shows values of T_n on a selection of images against a range of λ. Using results from Reeves et al. [22] and Sui et al. [123], a low dose scan with

Figure 4.2: TOP: CT images with simulated noise against varying λ. BOTTOM: An image subtraction of the simulated noisy image with the original.

a tube current-time product 25mAs has maximum T_n of 55HU. Thus, I assume $\lambda = 3.5$ corresponds to a low dose scan. I considered higher values of λ to verify any correlations in the results.

I computed the taper measurement on the noisy images using the same segmented airways and labelled distal point on the respective original image. The literature has shown in low dose scans, airway segmentation software [72, 24] cannot segment as distally compared to standard dose scans of the same patient. But these methods can still segment a large number of branches in low [72] and ultra-low [24] dose scans. Furthermore, research have shown there are minor differences in the performance of radiologists when attempting to detect features from standard and low dose CT scans [124, 125, 123].

4.4.1.2 Voxel Size

I analysed the effect of voxel sizes on the tapering measurement. For each CT image, the voxel spacing s_x, s_y, s_z, was subsampled to new spacing of $\sigma s_x, \sigma s_y, \sigma s_z$. The intensities at each new voxel position was computed using sinc interpolation with a small amount of smoothing. To compute the tapering value, I downsampled the segmented airway and distal point to the same coordinate system using nearest neighbour interpolation. Some morphological filtering was used on segmented airways to remove artefacts caused by the downsampling. For our experiment I used the parameters; $\sigma = 1.1, \ldots, 2$ with increments of 0.1.

4.4.2 CT Reconstruction

On a subset of images, four patients were scanned using the Toshiba Aquilion One Scanner. A total of 44 tapering measurements were computed. On the same acquisition data, two different images were computed. The images were reconstructed using the Lung and Body kernel respectively, an example of the reconstruction kernels are displayed on Figure 4.3. Table 4.1 shows which image was used to generate both the airway segmentation and distal point. The tapering measurement was computed on both reconstruction kernels using the same airway segmentation and distal points.

Patients	Reconstruction kernel used for prepocessing
bx503	FC56 - Lung
bx507	FC18 - Body
bx513	FC56 - Lung
bx515	FC18 - Body

Table 4.1: The images used for the reconstruction kernel experiment. The table lists which reconstruction kernel was used to generate the airways segmentation and distal point labelling. The make, model and voxels size of the images are displayed in Table 2.1.

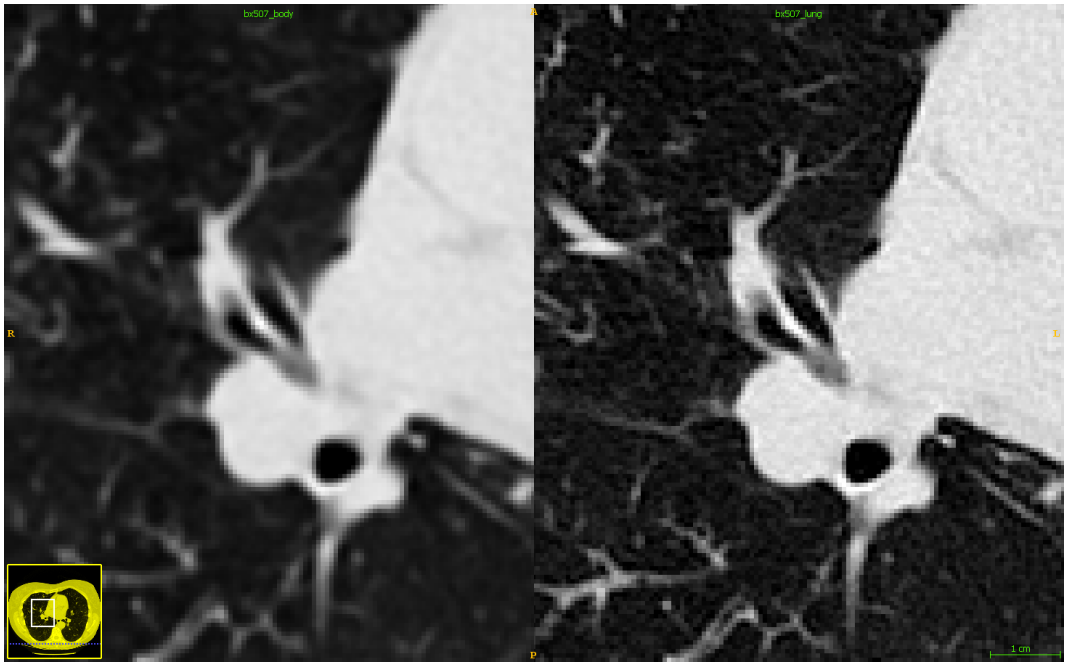

Figure 4.3: Images from the same CT scan with the body kernel (LEFT) and lung kernel (RIGHT). Both images are displayed in the same intensity window.

λ	bx500	bx503	bx504	bx505	bx507	bx508	bx511	bx512	bx513	bx515
Ground Truth	15	28	15	21	16	28	20	33	21	17
0.5	15	28	15	21	16	28	20	33	21	17
1.0	15	28	15	21	16	28	20	33	21	17
1.5	15	28	15	21	16	28	20	33	21	17
2.0	15	28	15	21	16	28	20	33	21	17
2.5	16	29	16	22	17	28	20	33	22	17
3.0	21	32	21	26	22	31	25	36	26	22
3.5	49	54	49	51	49	54	51	57	51	49
4.0	146	150	148	148	148	148	149	149	148	145
4.5	461	467	467	463	466	462	467	459	463	457
5.0	1456	1473	1477	1464	1474	1458	1475	1449	1463	1445

Table 4.2: Table of standard deviation of intensity, T_n (HU) in the inner lumen mask for a selected image against differing λ.

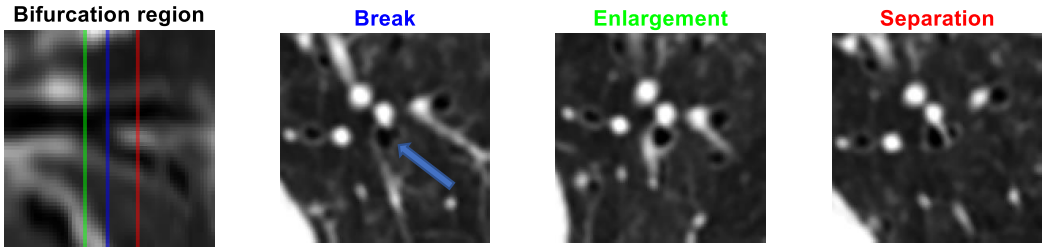

Figure 4.4: FAR LEFT: A region of bifurcation along the reconstructed slices. The green, blue and red regions are the slices corresponding to the enlargement, break and separation slices respectively. The labelled region consists of slices from green to red. CENTRE LEFT: A cross sectional plane where the airway is at the point of bifurcation, indicated by the blue arrow. CENTRE RIGHT: First slice of the bifurcation region. FAR RIGHT: The final slice of the bifurcation region. The slides are chronologically ordered with the protocol described in Section 4.4.3.

4.4.3 Effect of Bifurcations

I analysed the effect of airway bifurcations on the tapering measurement. To this end, I manually identified regions of bifurcating airways. On a selected subset of airways, I considered the reconstructed airway image described on Figure 4.14. Using ITK-snap, I started at the cross sectional plane corresponding to the carina and scrolled towards the distal point. Using visual inspection, the following protocol was developed to identify bifurcations on cross sectional planes:

1. The scrolling stops when the airway is almost or at the point of separation.

2. The author scrolls back until the airway stops decreasing in diameter. An alternative interpretation is when the airways are about to enlarge due to the bifurcation.

3. Starting at the point of enlargement and scrolling forward, each slice is delineated until complete separation of bifurcating airways is reached. The criteria for a complete separation is the lumen wall of both airways are completely visible and separate. The entire protocol is summarised in Figure 4.4.

For our experiment, I selected 19 airways from Section 2.5. The data consist of 11 healthy and 8 bronchiectatic airways.

4.5 Results

I present the results in the following sections: Section 4.5.1 & Section 4.5.3 compares the reproducibility of taper and cross-sectional area measurements against simulated doses and CT kernels respectively. In Section 4.5.2, compares the reproducibility of taper and arc length measurements against simulated voxel sizes. Finally, Section 4.5.4, compares the taper measurements with and without bifurcation regions.

4.5.1 Dose

I analysed the difference in cross-sectional area measurements and the final tapering measurements at different CT radiation doses.

For the cross-sectional areas, Figure 4.5 compares the cross-sectional areas between the original image and one of the noisy images. Each graph contains approximately 30000 unique lumen measurements. The correlation coefficients between the populations was $r > 0.99$ on all graphs. The 95% confidence intervals increase with the amount of noise. For the tapering measurement, Figure 4.6 displays the measurements from all the noisy images compared against their respective original images. The correlation coefficient between noisy and original tapering measurements was $r > 0.98$ on all values of λ.

For the tapering measurement, Figure 4.6 displays the measurements from all the noisy images compared against their respective original images. The correlation coefficient between noisy and original tapering measurements was $r > 0.98$ on all values of λ. For the repeatability dose images, there were negligible differences in the tapering measurement on images generated using the same value of λ.

I analysed the tapering difference between the original images and simulated images. I interpret the mean and standard deviation of the error difference as the bias and uncertainty respectively. Figure 4.7, shows an overestimation bias with an increase in noise and a positive correlation between uncertainty and dose.

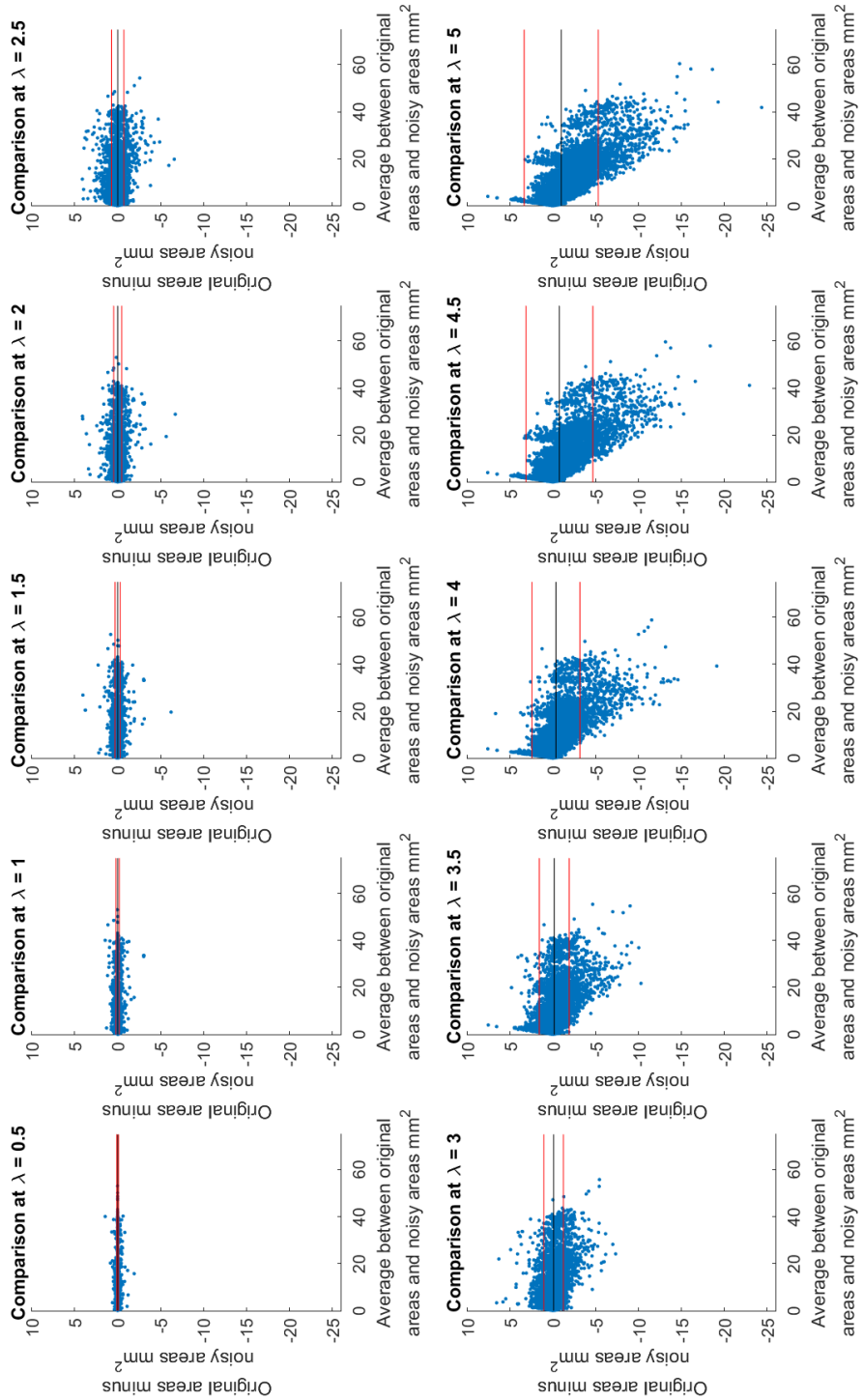

Figure 4.5: A series of Bland-Altman [1] graphs comparing area measurements from simulated low dose scan and the original image. On all graphs, the correlation coefficient was $r > 0.99$

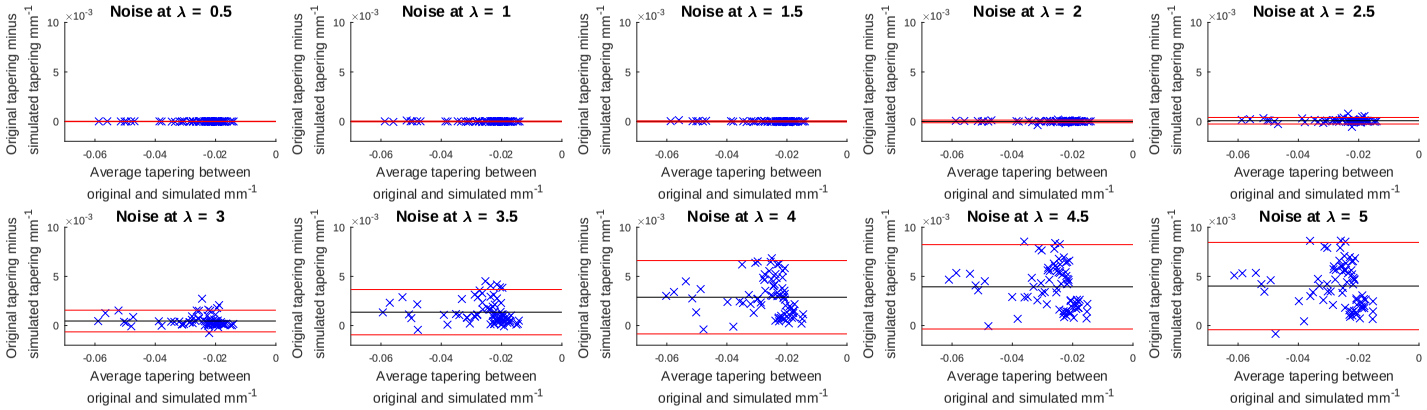

Figure 4.6: A series of Bland-Altman [1] graphs comparing tapering measurement between simulated dose and the original image. On all graphs the correlation coefficient was $r > 0.98$.

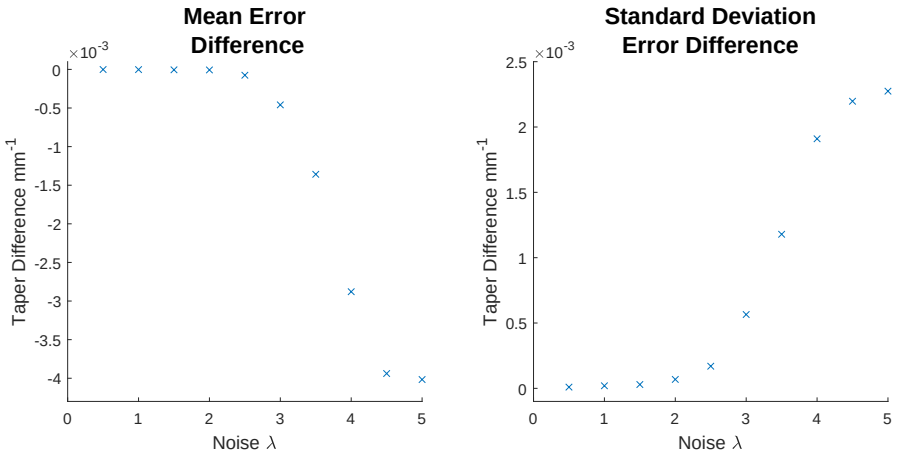

Figure 4.7: Mean (LEFT) and standard deviation (RIGHT) of the difference in tapering between original images minus the simulated lower dose.

4.5.2 Voxel Size

I analysed the computed spline and tapering for all the scaled images. I used the arclength of the spline as the metric for comparison for the computed spline. Figure 4.8 compares the arclengths computed from the scaled splines with the respective originals. On all scales σ the correlation coefficients between measurements was $r > 0.98$. Furthermore, I analysed the error difference in arclength. On Figure 4.9, the mean difference shows a weak correlation coefficient with $r = 0.55$ with scale σ. The mean difference shows both an overestimation and underestimation bias with the arclength measurement. Figure 4.9, shows a weak correlation between standard deviation and scale with $r = 0.51$.

In terms of the tapering measurement, Figure 4.10 compares the tapering values from the scaled images with the respective originals. The correlation coefficients between the scaled and original tapering values was $r > 0.97$ on all scales σ. In addition, I examined the error difference of the original minus the scaled tapering. Figure 4.11, shows a negative correlation with both overestimation and scale with $r = -0.98$. Furthermore, Figure 4.11, shows a positive correlation with uncertainty and scale with $r = 0.94$.

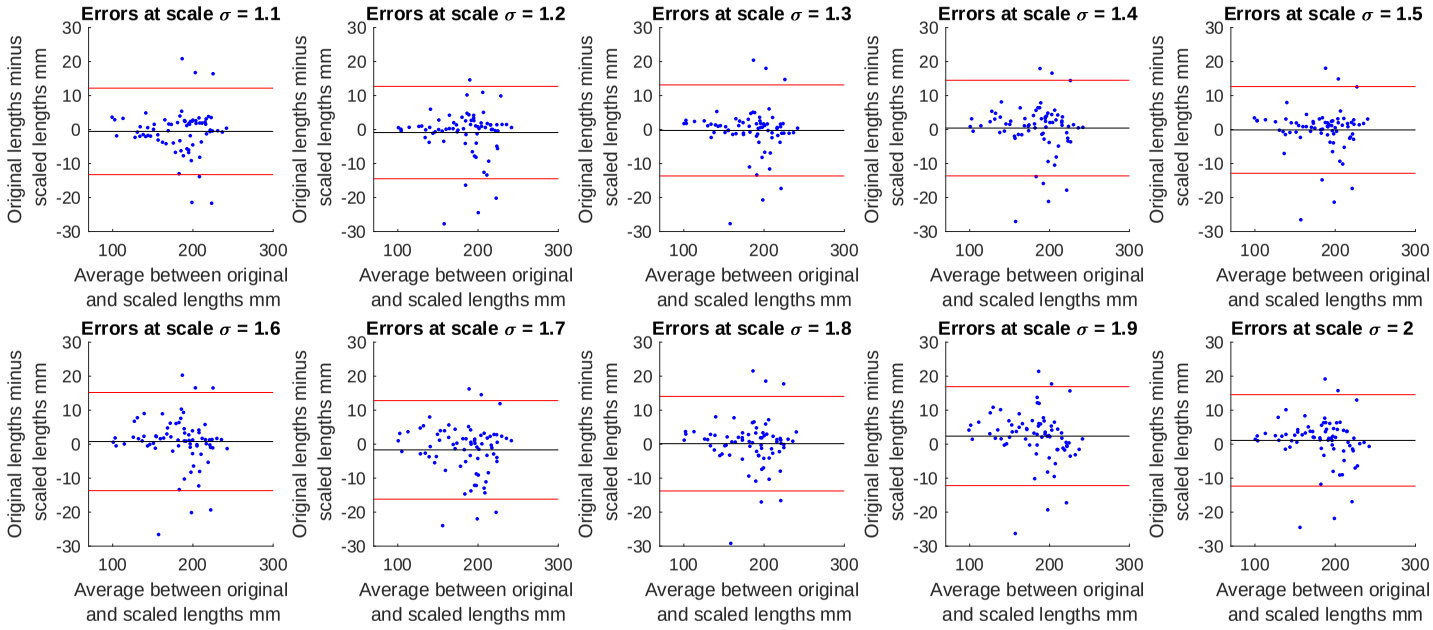

Figure 4.8: A series of Bland-Altman [1] graphs comparing arc lengths between scaled images and the original images. On all graphs, the correlation coefficient was $r > 0.98$

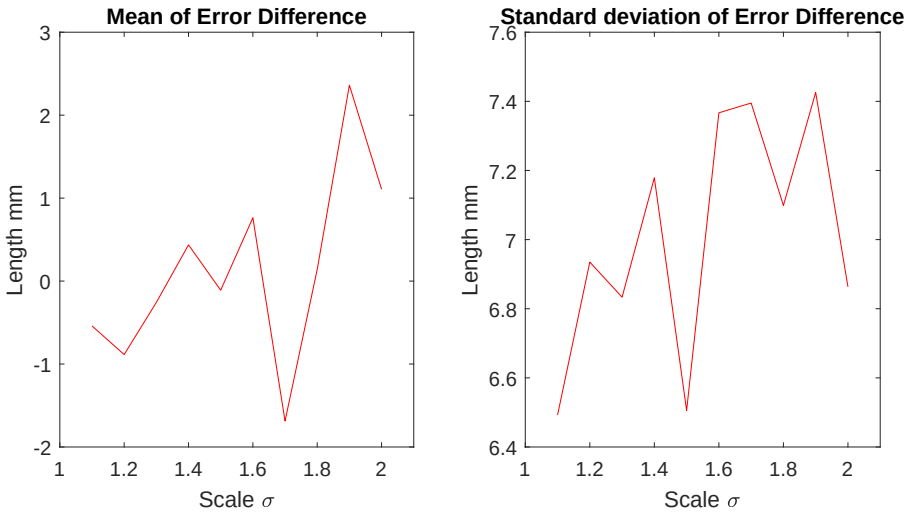

Figure 4.9: Mean (LEFT) and standard deviation (RIGHT) of the difference in arclength between original images minus the scaled images. The correlation coefficient of the mean and standard deviation against scale are $r = 0.55$ and $r = 0.51$ respectively.

4.5.3 CT Reconstruction

I analysed the difference in cross sectional area and tapering measurement between reconstruction kernel. Figure 4.12, compares the difference in area measurements. On all patients, the correlation coefficient between the two measurements was $r > 0.99$. The largest 95% confidence was in patient bx515 with ± 1.98 mm^2 from the mean. Figure 4.13, compares the differences in tapering measurement. I collected $n = 44$ tapering measurement from 4 patients. The correlation coefficient was $r = 0.99$ between the reconstruction kernels.

4.5.4 Bifurcations

I compared tapering measurements with and without points corresponding to bifurcations. On the first dataset, the tapering measurements were computed using all area measurements. The second dataset has tapering measurements computed without area measurements from the bifurcating regions as described in Figure 4.14. I compared the measurements on Figure 4.15, the correlation coefficient was $r = 0.99$.

The uncertainty of each tapering measurement were computed using the stan-

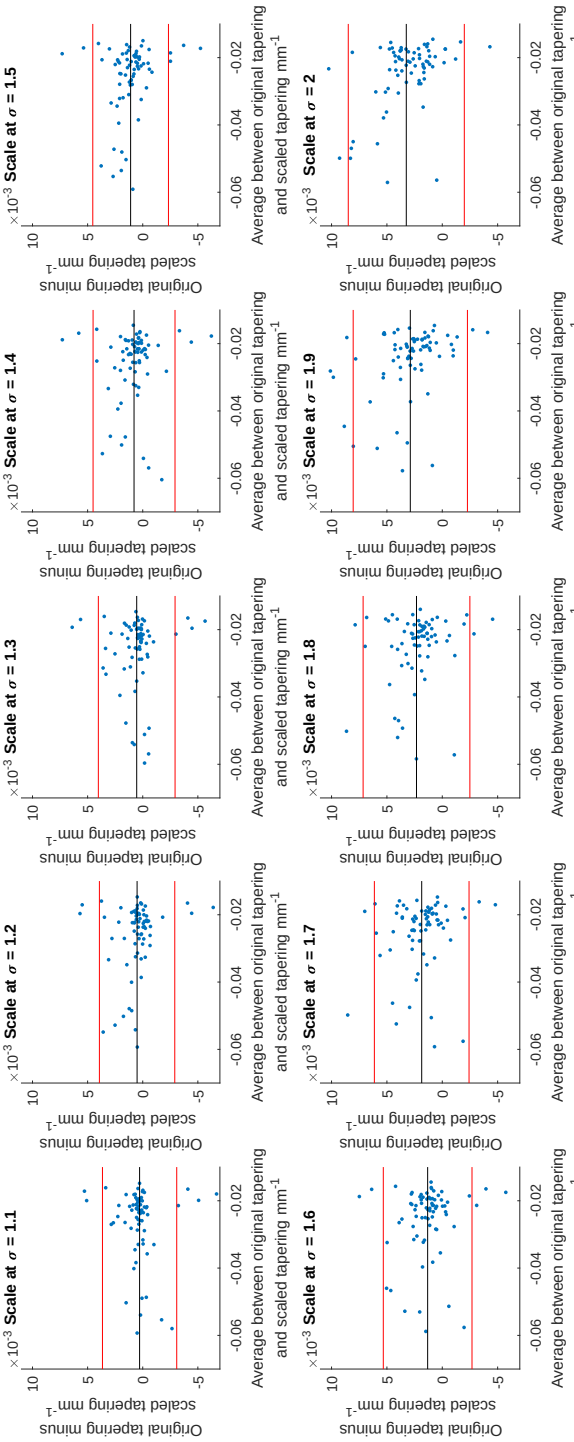

Figure 4.10: A series of Bland-Altman [1] graphs comparing tapering between original images and scaled images. On all graphs the correlation coefficient was $r > 0.97$

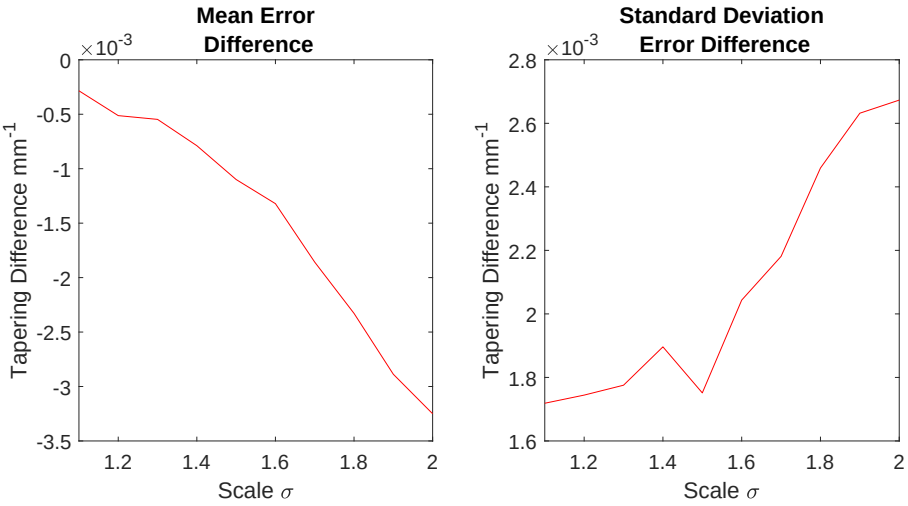

Figure 4.11: Mean (LEFT) and standard deviation (RIGHT) of the difference in tapering between original images minus the scaled images. The correlation coefficient of the mean and standard deviation against scale are $r = -0.98$ and $r = 0.94$ respectively.

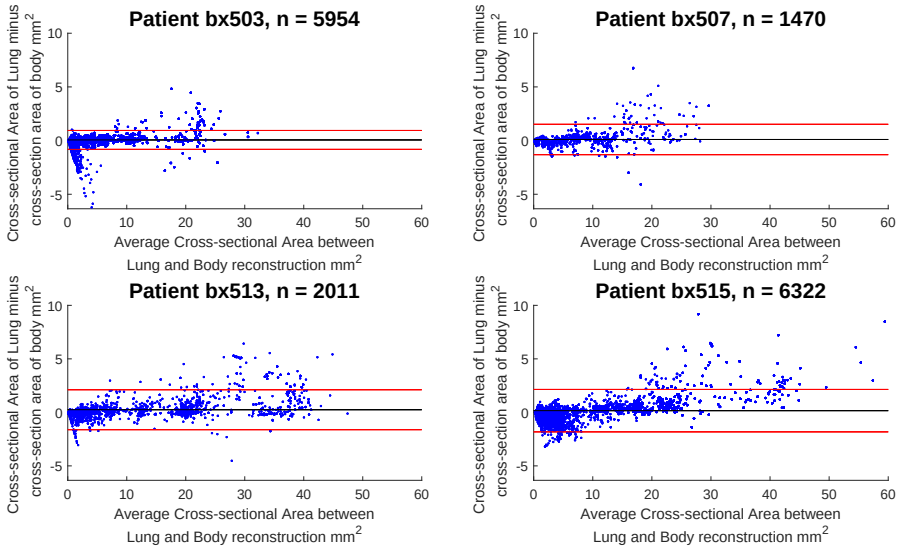

Figure 4.12: Bland-Altman [1] graphs comparing the cross-sectional area between the Lung and Body reconstruction kernels. On all four images the correlation coefficient was $r > 0.99$

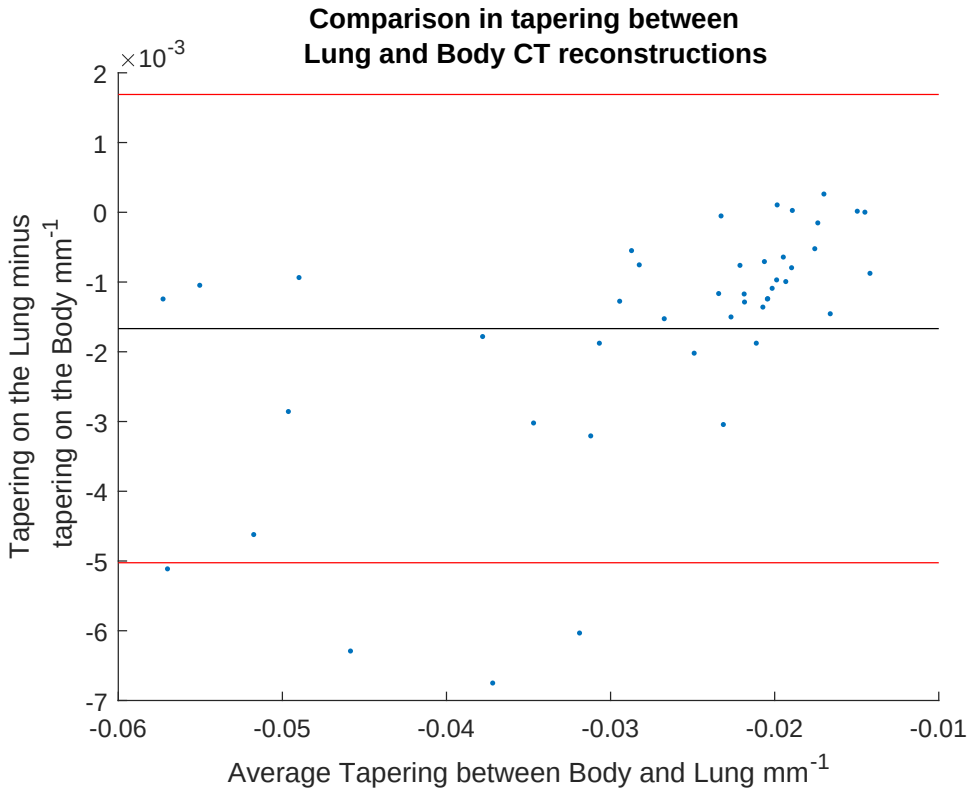

Figure 4.13: Bland-Altman [1] graph comparing tapering measurements $(n = 44)$ between Lung and Body reconstruction kernels, $r = 0.99$.

dard error of estimate s, defined as [126]:

$$s = \sqrt{\frac{\sum_{i=1}^{N}(Y_i - y_i)^2}{N}} \tag{4.1}$$

where x_i, y_i is the computed area and arclength respectively, Y_i is the estimate from the linear regression from each x_i and N is the number of points in the profile. Figure 4.14 compares the uncertainty between the two populations. There was a statistical difference between the populations, on a Wilcoxon Rank Sum Test, $p = 7.1 \times 10^{-7}$.

4.6 Discussion

In this Chapter, I quantified the behaviour of the reproducibility of my proposed tapering measurement against CT parameters and regions of bifurcation. Experiments included in silico image simulation of differing dose and voxel sizes. For the dose experiment, I related the image noise with the radiation dose through segmenting

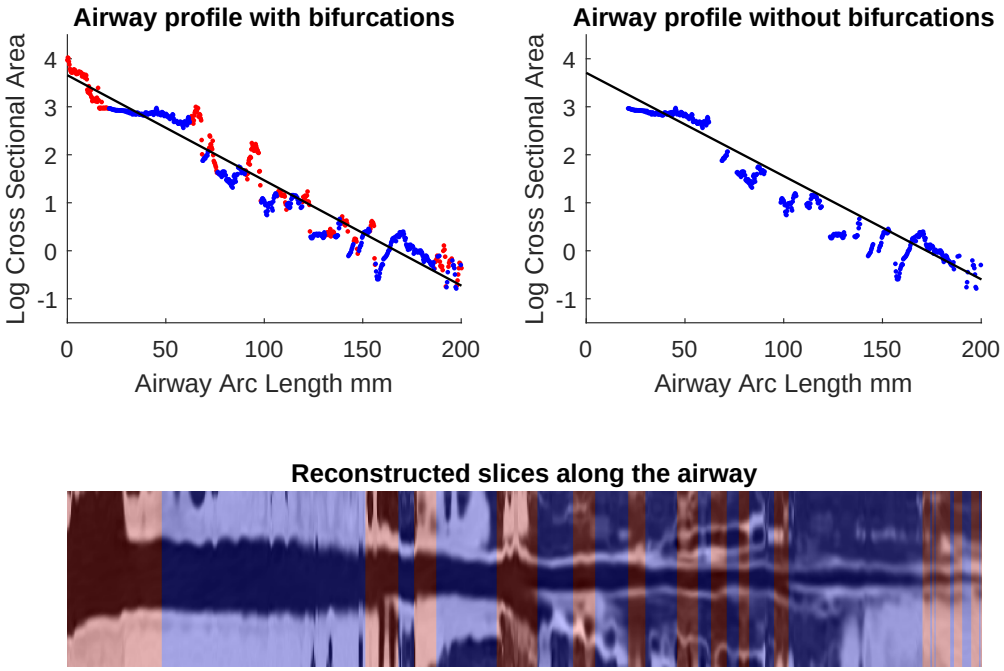

Figure 4.14: TOP LEFT: A signal of area measurement with bifurcation regions (red) and tubular regions (blue). TOP RIGHT: The same signal with tubular regions (blue) only. On both graphs, the black line is the linear regression of the respective data. The gradient of the line is the proposed tapering measurement. BOTTOM: The reconstructed bronchiectatic airway of the same profile. The blue-shaded and red-shaded regions corresponds to the tubular and bifurcating airways respectively. A reconstructed healthy airway have been discussed in Quan et al. [2] Similar reconstructed cross sectional images of vessels have been discussed in Oguma et al. [3], Kumar et al. [4] and in the supplementary materials of Alverez et al. [5].

the trachea and computed the standard deviation of the mask.

In this chapter, I analyse the reproducibility of all computerized components of the tapering algorithm. The chapter does not address reproducibility of manual labelling of the airways. It is noted in the literature that semi-manual labelling of small airways can take hours [127]. Future work is required to analyse the reproducibility of manual segmentation of the airways. I hypothesise, that the segmented healthy peripheral airways consist of a small number of voxels, therefore any errors in voxel labelling will be considerable smaller then a dilated peripheral airway affected by bronchiectasis.

In this work, I simulated low dose scans through performing Radon transforms

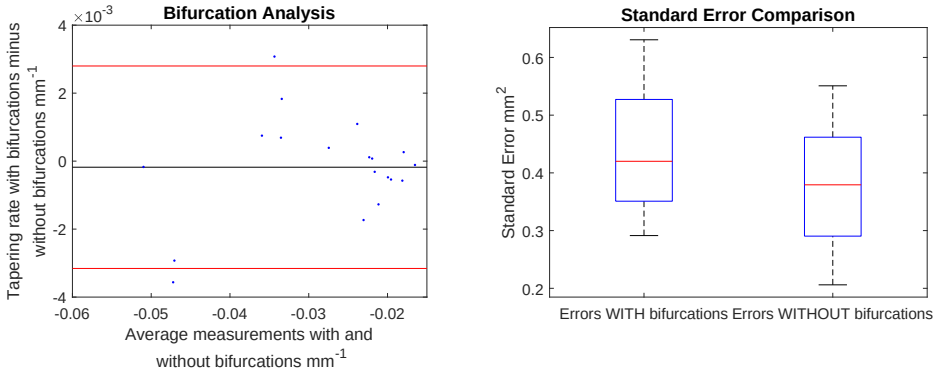

Figure 4.15: LEFT: Bland-Altman [1] graph showing the relationship of the taper rates $(n = 19)$ with and without bifurcations, $r = 0.99$. RIGHT: Comparison of the standard error from linear regression between airways with and without bifurcations. On a Wilcoxon Rank Sum Test between the two populations, $p = 7.1 \times 10^{-7}$.

on existing CT images, adding Gaussian noise on the sinogram and using backprojection to reconstruct noisy CT images. There are proposed methods to simulate a low dose scans by adding a combination of tailored Gaussian and Poisson noise on the sinogram [21]. These methods assume the original high dose sinogram are available for simulation, however it has been acknowledged that sinograms are generally not available in the medical imaging community [128, 129]. Thus, various groups have proposed low dose simulations using reconstructed CT images. The methods involve adding Gaussian [129, 128] or a combination of Gaussian and Poisson noise [130] on the sinogram of the forward projection of the CT image. Whilst there has been limited validation of the appearance of lung nodules against simulated low dose simulation [131], there has been no validation on the efficacy of these methods on the appearance of airways. I believe that our low dose simulation is sufficient because the measured standard deviation of the trachea mask T_n is similar to results taken from low dose scans from Reeves et al. [22] and Sui et al. [123]

Similarly, with voxel size simulation, ideally one would reconstruct the images from the original sinogram, for example in Achenbach et al [25]. However, as the sinograms were unavailable, we simulated the voxel size through interpolation of the original CT images similar to Robins et al [132]. We believe the simulation is sufficient as it shows the robustness and precision of the centreline, recentring

and cross-sectional plane algorithms in the pipeline. Changes in voxel sizes will change the combinatorics or arrangement of the binary image. By showing steps in the pipeline like centreline computation, are repeatable across voxel sizes, we avoid resampling the image to isotropic lengths. Thus, potentially avoiding a computationally expensive [24] pre-processing step. In the same experiment, I downsampled the binary image using nearest neighbour interpolation [111]. The original binary airway segmentation consists of sparse labelling and vessel structures. From Justesen and Forchhammer [133], nearest neighbour method creates a bias towards black voxels and maintains the topology of the object. Thus, making the method superior to linear interpolation.

In addition, I used a subset of airways to analyse the reproducibility of the tapering measurement under different CT reconstruction kernels. The limited samples were due to CT reconstructions being restricted to commercial vendors [134]. The experiment is sufficient as a proof of principle study in reproducibility as I have assessed robustness of cross-sectional area measurements between different reconstructions. Changes in CT kernels will cause subtle changes in the intensity profiles on the edge of the airways [135].

4.7 Conclusion

Previously in Chapter 2, I showed a statistical difference in tapering between healthy airways and those affected by bronchiectasis as judged by an experienced radiologist. From Figure 2.4, the difference between the mean and median of the two populations was 0.011mm^{-1} and 0.006mm^{-1} respectively. In simulated low dose scans, the tapering measurement retained a 95% confidence interval of $\pm 0.005\text{mm}^{-1}$ up to $\lambda = 3.5$. In simulations assessing different voxel sizes, the tapering measurement retained a 95% confidence between $\pm 0.005\text{mm}^{-1}$ up to $\sigma = 1.5$. The tapering measurement retains the same 95% confidence, $\pm 0.005\text{mm}^{-1}$ interval against variations in CT reconstruction kernels and, importantly, over time in evaluating sequential scans in normal airways. Furthermore, in our previous work (Chapter 3), the measurements are accurate to sub voxel level. This suggests airway tapering

can be used to assist clinical trials provided phantom calibration is performed on the scanner.

For the bifurcation experiment, I show the tapering values retains the 95% confidence, $\pm 0.005\text{mm}^{-1}$ against variations of bifurcations. Since there is a small change in tapering values between airway tracks with and without bifurcations. I show it may be unnecessary to segment and remove bifurcation regions of the airways. It has been shown in the literature that segmenting bifurcation is a non-trivial task [136].

I analysed the reproducibility of the components that constitute the tapering measurements. The reproducibility of area measurements was analysed in relation to simulated radiation dose and CT reconstruction kernels. For simulated dose, I found the 95% confidence interval remains at $\pm 1.5\text{mm}^2$ in noisy images under $\lambda = 3$. Note on Figure 4.5, there is a bias towards overestimating larger lumen sizes at lower doses. As the centreline length remains constant and bias on the smaller lumen remain stable, the overestimation results in an increase in taper magnitude. For reconstruction kernel, I found the largest 95% confidence interval was $\pm 1.9\text{mm}^2$. The reproducibly of arclength was tested against voxel sizes and showed that arclengths have a 95% confidence interval of up to ± 5.0mm for scales under $\sigma = 1.5$. The increase in the standard deviation of arclength and area against voxel size and dose respectively correlate with uncertainty in tapering. The results show that my tapering measurement is suitable to be used on a population of airways containing scans with a range of doses. However, further investigation is required to show if the current pipeline described in Section 2.4, can be applied on airways solely from low dose scans. I hypothesise two possible approaches to improve the validity of my tapering measurement in low dose scans. First, replace the current lumen measuring algorithm in Section 2.4.5 to a method designed for low dose scans such as from Yang et al. [104]. Second, using deep learning methods such as Yang et al. [26] to modified the CT scan to reduce artefacts or to infer features from high dose scans. A major disadvantage of these deep learning methods is it has been shown that some algorithms can hallucinate features [137].

This chapter provides useful information for clinical practice and clinical trials. An accurate prediction of the noise amplitude in a particular CT scan and its distribution is a function of the limited radiation dose of the scan, scanner geometry, reconstructed voxel size, other sources of noise, the reconstruction algorithm and any pre- and post-processing used. Many of these factors are proprietary information of the CT manufacturer and hence not available to users [138, 139]. We have undertaken an experiment to assess the dependence of our measurements on a simulated noise field added to the CT scan data and have presented the results. This gives an indication of the dependence on radiation dose assuming all other factors remain the same. We recommend that the accuracy experiment presented in this paper be repeated for the particular reconstruction, scan protocol and scanner type used to make the measurements.

Bronchiectasis is often described as an orphan disease and has suffered a lack of interest and funding [140, 38]. I have shown the reproducibility of airway tapering can assist in the diagnosis and management of bronchiectasis. In addition, we show it is feasible to use our tapering measurement in large scale clinical studies of the disease provided careful phantom calibration is taken.

In the next chapter, I will be analysing specific points of dilatation of the airways track. I combine my proposed pipeline with Bayesian changepoint detection to find regions of diseased airways. I show the clinical utility by using my proposed algorithm by finding volume change on airways affected by idiopathic pulmonary fibrosis (IPF).

Chapter 5

Locating Changes along the Airway Track

The following chapter is a joint collaboration with Ryutaro Tanno (RT) and Michael Duong (MD). In terms of contributions, MD developed and implemented Bayesian changepoint formulation and Reversible Jump Metropois Hasting. RT contributed as an advisor role on presentation and interpretation of results and data analysis.

5.1 Abstract

Numerous lung diseases, such as idiopathic pulmonary fibrosis (IPF), are manifested as dilation of the airways. In order to quantify the progression of such diseases, prior analyses have introduced a variety of computational methods for measuring the airway cross-sectional area from CT images. However, the combination of image noise and anatomical fluctuations causes high variability in the measurements of cross-sectional areas, rendering the identification of affected regions very difficult. In this work, I introduce a noise-robust method for automatically detecting the location of progressive airway dilatation given two measurements of the same airway acquired at different time points. To this end, I propose a probabilistic model of abrupt relative variations between two measurements of cross-sectional areas and perform inference via Reversible Jump Markov Chain Monte Carlo sampling. I demonstrate the efficacy of the proposed method on two datasets; (i) images of healthy airways with simulated dilatation; (ii) pairs of real images of IPF-affected

airways acquired at 1 year intervals. Results on simulated data show that our model is able to detect the starting location of airway dilatation within the accuracy of 2.5mm, while the experiments on the IPF dataset display reasonable agreement with radiologists. In addition, I demonstrate that by estimating the location of dilatation I can compute a relative change in airway volume which is useful for quantification of IPF disease progression.

5.2 Publication

The contents if this chapter has been accepted in the following:

- **K Quan**, R Tanno, M Duong, A Nair, R Shipley, M Jones, C Brereton, J Hurst, D Hawkes, J Jacob, "Modelling Airway Geometry as Stock Market Data using Bayesian Changepoint Detection", In *10th International Workshop on Machine Learning in Medical Imaging*, 2019.

5.3 Introduction & Motivation

In fibrosing lung disease, contraction of the lung interstitium pulls on airway walls, and this dilatation is termed traction bronchiectasis. Airway dilatation calculated using crude lobar-level visual scores have been shown to be powerful predictors of outcome in idiopathic pulmonary fibrosis (IPF) [141]. More precise and automated measures that can identify and quantify airway dilatation over time on serial computed tomography (CT) imaging would be valuable as potential endpoints for IPF drug trials as a more sensitive measure of disease progression.

Conventional methods evaluating airways as a measure of disease progression are restricted to comparing cross-sectional area measurements at a given generation between baseline and follow up scans [142]. The measurements are taken at sparse intervals and thus it is not possible to compute measures such as airway volume nor locate the precise spatial arrangement of airway damage in the lungs. To our knowledge, no work has analysed disease progression in terms of a series of cross-sectional area measurements along the airway track at contiguous intervals. I considered an airway track as a path along the airway centreline from the start of

the carina to the most distal point of an airway visible on a CT image. However one would have to distinguish a dilatation from various sources of noise including: (i) Biases and precision from computing CSA such as from centreline generation [73] and lumen identification [96]. (ii) Artefactual measurements such as in bifurcation regions [2]. (iii) Normal biological variations [143].

5.3.1 Contribution

My contribution is to introduce a Bayesian Change Point Detection model to track the progression of pulmonary disease along the airway using contiguous airway lumen measurements. Bayesian Change Point Detection is a machine learning method used to locate abnormal or sudden changes in a given signal or time series. The method looks not only the absolute change in signal but also change in the underlying distribution of measurements. For our work, I have applied the method to a series of cross-sectional area changes between baseline (first) and follow up (second) CT scans. The purpose is to automatically find the point at which the airway has dilated due to parenchymal disease.

Bayesian Change Point Detection has been mainly applied to DNA sequencing [144] and stock market data [145]. The main challenge in implementing our proposed algorithm, that there are no analytical solutions when I input non-conjugate distributions. Thus, I will implement a Reversible-jump Markov Chain Monte Carlo (RJMCMC) framework [146, 147] to find an approximation to the solution.

To demonstrate clinical utility, for this paper I applied our Bayesian Change Point Detection model on airways affected by IPF. Whist there are methods to quantify disease progression in IPF, none have utilised automated measures of airway volume, despite crude visual lobar measures of traction bronchiectasis having been shown to strongly predict mortality in IPF. Proposed automated measures of parenchymal damage such as CALIPER and QLF consider imaging features selected by the radiologist [148]. Our methods uniquely, solely depend on changes to the geometry of the airways.

5.4 Method

In this section, I introduce a method for quantifying progression of IPF on patients with serial CT scans performed one year apart. The method proceeds as follows. Firstly, I fit a tubular shape model to airways in both baseline and follow-up CT scans, and acquire estimates of the cross-sectional areas along them (Sec. 5.4.1). I then treat the difference in the cross-sectional areas as a time series, and employ the proposed Bayesian change point model to estimate the posterior distribution over locations of abrupt airway dilatation (Sec. 5.4.2). Lastly, I post-process this posterior distribution to determine the region of dilatation (Sec. 5.4.3).

5.4.1 Airway Pre-processing

In this work, I assume that each diseased airway is scanned at two different time points, which I refer to as the "baseline" and "follow-up" scan. For each airway track, I acquire a series of cross-sectional area measurements using the method in Section 2.4 and summarised in on Figure 5.1. Following a manual segmentation of the airway, as described in Section 2.4, the method computes the airway centreline and the corresponding normal planes at contiguous intervals, each of which is then used to estimate the cross-sectional area. The final output is a 1D function of cross sectional area along the arc length of the airways for baseline $f_{Base}(x)$ and follow up $f_{FoUp}(x)$ scans.

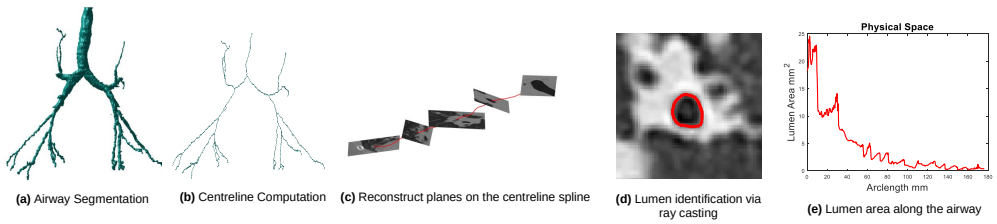

Figure 5.1: Summary of the pipeline developed Section 2.4. I have implemented the method as part of the pre-processing stage to model the geometry as a 1D signal.

The next task was to align the signals on both baseline $f_{Base}(x)$ and follow up $f_{FoUp}(x)$ scan. To this end, I resample the signal to 1mm using cubic interpolation. I considered the first 50 points on both signals g_{Base}, g_{FoUp} from the start of the carina.

To register the two airways together, I apply the transformation $f_{FoUp}(x-a)$ where

$$a = \text{argmin}_{a\in[-5,5]} \left|\left| \log\left(\frac{g_{Base}(x)}{g_{FoUp}(x-a)}\right)\right|\right|_2. \tag{5.1}$$

The longest of the two signal were truncated from the right hand side such that both signals were of the same length. For the rest of the methodology, I will only consider the series difference defined as

$$y = \log(f_{FoUp}) - \log(f_{Base}). \tag{5.2}$$

5.4.2 Bayesian Changepoint Model

5.4.2.1 Changepoint Definition

The progression of fibrosing lung disease can manifest as traction bronchiectasis, resulting in dilatation of the airways. Thus I hypothesise at the start of dilatation, the series y will begin to abnormally increase thus producing a change point. To detect the change point, I introduce a probabilistic model. More formally, given signal:

$$y = (y_1, \ldots, y_n) \tag{5.3}$$

of length n, I define a change-point τ as the location where there exists a change in parameters θ in the underlying distribution F. In other words, at change point $1 < \tau < n$, the observations y can be separated at τ such that:

$$y = \begin{cases} (y_1, \ldots, y_\tau) \sim F(\theta_1) \\ (y_{\tau+1}, \ldots, y_n) \sim F(\theta_2) \end{cases}, \tag{5.4}$$

where $\theta_1 \neq \theta_2$. This definition can be naturally extended to the scenario with M change points; I denote the changepoint location vector by $\tau = (\tau_1, \ldots, \tau_k)$, with parameters $\theta = (\theta_1, \ldots, \theta_{k+1})$ for each respective segment. For ease of notation, I also denote $\tau_0 = 1$ and $\tau_{k+1} = n$.

In terms of time series, a changepoint is interpreted as the point y_τ where the

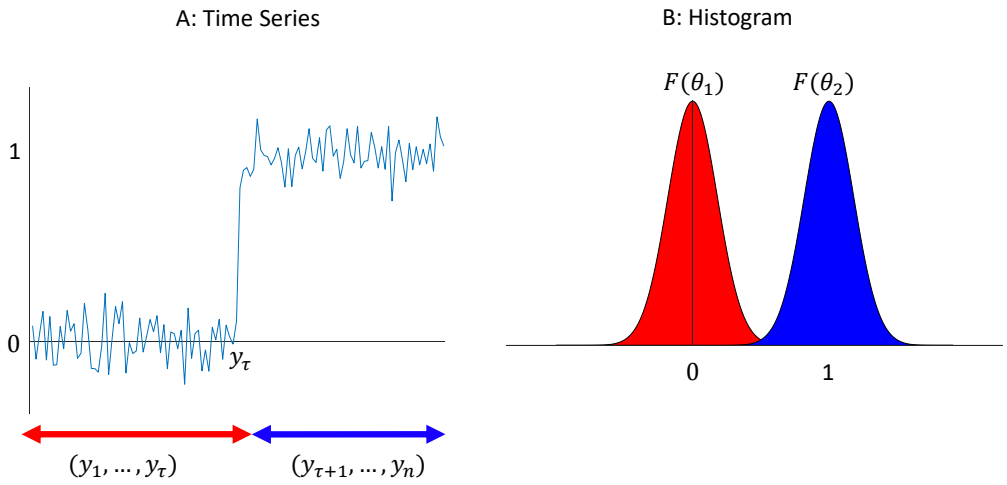

Figure 5.2: A schematic diagram describing a changepoint. Using the same notation in Equation 5.4, consider the time series in A. There is a changepoint τ at y_τ, if I select the points on the left-hand side; highlighted in red and construct a histogram from these points. The histogram would approximate into a Gaussian distribution F those parameters $\theta_1 = (\mu_1, \sigma_1^2)$ which includes a mean, $\mu_1 = 0$. By performing the same analysis on the points on the right-hand side highlighted in blue. The resulting histogram would be a Gaussian distribution F those parameters $\theta_2 = (\mu_2, \sigma_2^2)$ with $\mu_2 = 1$. Thus $\theta_1 \neq \theta_2$ resulting in a changepoint y_τ between the segments.

time series changes in behaviour. I qualified the behaviour as the points being sampled from the probability distribution function F with the parameters θ. An example is described in Figure 5.2.

5.4.2.2 Model Assumption

Assuming statistical independence between segments, the likelihood factorises as:

$$p(y|\tau, \theta, M) = \prod_{l=1}^{k+1} F(y_{\tau_{l-1}:\tau_l}|\theta_l) \tag{5.5}$$

where $y_{\tau_{l-1}:\tau_l} = (y_{\tau_{l-1}}, \ldots, y_{\tau_l})$. I also specify prior distributions on the the number of change points $p(M;\delta)$, the locations of the changepoints $p(\tau|M;\gamma)$, and the parameters of the corresponding segments $p(\theta|M;\beta)$ where β, γ and δ represent the hyper-parameters.

Given the likelihood and the prior distributions above, I would like to estimate the posterior distributions over the locations of change points $p(\tau|y)$. Commonly in

Bayesian change point analysis, likelihoods with a conjugate prior are chosen to allow calculation of analytical posteriors for change points and parameters, enabling faster convergence and better accuracy [149]. However, in our work, I wish to relax this conjugacy assumption in order to allow flexibility in the choices of prior and likelihoods. In this paper, F was defined as the Student t distribution with parameters $\theta_l = (\nu_l, \mu_l, \sigma_l)$ with degrees of freedom ν_l, mean μ_l and standard deviation σ_l. I chose t-distribution for its robustness to outliers [150] caused by noise from the area measurements.

Posterior inference with our model possesses two challenges. Firstly, without the conjugacy assumption, computing the posterior distributions is intractable. Secondly, the dimensionality of the posterior distribution over the changepoints τ is given by M and varies during inference. To combat the first problem, I use the Metropolis-Hasting (MH) algorithm [151], a variant of Markov Chain Monte Carlo (MCMC) methods that can sample from the posterior, with or without conjugacy. Given that the number of changepoints M is known, MH can be used to sample from the posterior distributions over the changepoints τ and segment parameters θ. To address the second problem of varying posterior dimensionality M, I extend the above sampling scheme to the Reversible Jump MCMC framework [147]. Taken all together, the method is capable of traversing the full posterior distributions for M, τ, θ and I refer to this as Reversible Jump Metropolis Hasting (RJMH) algorithm. A detailed implementation is discussed in Appendix A.

5.4.3 Locating Change in Airway Dilatation

For airways affected by IPF, dilatation starts at the distal point and progresses in the proximal direction [54]. Therefore, I topologically can assume that each affected airway undergoes a single changepoint from which dilatation starts. To locate such unique changepoint, I consider the posterior probability of the changepoint $p(\tau|\mathbf{y})$, and perform the following post-processing steps.

On each airway track, the proximal region is surrounded by cartilage [9]. As the airway track loses cartilage support, the geometry of the airway changes and results in a changepoint. Since such biological changepoint is independent of the

disease state and occurs prior to dilatation, I eliminate it by discounting the most proximal peak in the posterior distribution $p(\tau|\mathbf{y})$. I then selected highest peak on the modified posterior $p(\tau|\mathbf{y})$ as the final estimation for the starting point of dilatation.

5.5 Evaluation & Results

I evaluated our proposed method with two experiments. Firstly, I used a set of healthy airways, in which I had simulated dilatation to quantify the accuracy of our method and compared the results with conventional changepoint methodologies. Secondly, I assessed the clinical utility of our method on a dataset of airways affected by IPF. I compared our labels with those from two experienced thoracic radiologists. The properties of the images used in both experiments are displayed on Table 5.1.

5.5.1 Disease Simulation

To quantitatively assess accuracy, a ground truth is required. To this end, I applied our point detection algorithm on augmented healthy airway series to simulate the airway dilatation caused by IPF. After obtaining written informed consent from 3 patients, a trained radiologist (R1) selected 14 pairs of healthy airways in both baseline and follow-up scans. The image properties are displayed on Table 5.1. They were acquired from different scanners and used different reconstruction kernels. The airways were pre-processed as described in Sec. 5.4.1 to produce a function of area change along the length of the airway. I interpret this output signal as the overall noise caused from normal biological changes and acquisition.

I modelled the change in dilatation with a logistic function:

$$l = \frac{M}{1 + e^{-k(x-\alpha)}}. \tag{5.6}$$

I interpreted M as the magnitude of dilatation and α as the point of dilatation. The parameters α are set such that the dilatation starts 10-40mm from the distal point in increments of 5mm. In addition, I set M to range from 0.3-3 in increments of

Experiment	Patients	Baseline Scan Voxel Size	Follow-up Scan Voxel Size	Airways Tracks	Time between scans
1	1	0.67, 0.67, 1.00	0.56, 0.56, 1.00	6	9M 6D
1	2	0.63, 0.63, 1.00	0.78, 0.78, 1.00	7	35M 6D
1	3	0.72, 0.72, 1.00	0.72, 0.72, 1.00	1	5M 22D
2	4	0.72, 0.72, 1.00	0.64, 0.64, 1.00	3	12M 5D
2	5	0.67, 0.67, 1.00	0.87, 0.87, 1.00	1	10M 24D

Table 5.1: Table of the image properties of voxel size, number of airways used and the time between scans. The airways were selected by a trained radiologist R1. All patients in Experiment 1 do not have IPF. Voxel Size units are in mm and in (x,y,z) direction. Abbreviation: M - Months, D - Days.

0.25. Finally I set $k = 0.5\text{mm}^{-1}$, in order to create an abnormal increase in cross sectional area. To simulate the dilatation on the airway; the logistic function was added to the area change of the healthy airway, as shown on Figure 5.3. I applied every permutation of M and α on each of the 14 healthy airways. After the signal augmentation, I applied our proposed Bayesian changepoint detection algorithm.

The proposed method was compared against two conventional methods. First, I use a basic thresholding method. For a given signal, I applied a 5mm moving mean average and thresholded the point at which the signal reached above the upper quartile from the right hand side. Secondly, I implemented the method based on Lavielle [6], in summary I consider K changepoint and these changepoints y_i, minimize the function:

$$J(K) = \sum_{r=0}^{K-1} \sum_{i=k_r}^{k_{r+1}-1} \Delta(y_i, y_{k_r:k_{r+1}-1}) + \beta K, \tag{5.7}$$

where β is modified such that the function finds less than K changepoints. For our paper, different $\Delta(y_i, y_{k_r:k_{r-1}-1})$ were evaluated and I found

$$\Delta(y_i, y_{k_r:k_{r-1}-1}) = y_i - \text{mean}(y_{k_r:k_{r+1}-1}) \tag{5.8}$$

gives the most accurate results. To replicate the post processing of our proposed method, I consider $K = 2$ possible changepoints. This takes into account the changepoint caused by the support cartilage. Finally, I set a minimum distance of 20mm. Once I acquired the changepoints, the most peripheral point was chosen as the point of dilatation. The implementation was performed through Matlab inbuilt function; `findchangepts`[1].

Figure 5.4 shows the accuracy for each individual method as a heatmap. The metric used to quantify accuracy was the displacement between the ground truth and the changepoint given by the proposed method. A positive displacement (mm) corresponds to an overestimation of the ground truth towards the distal point. Each

[1] `https://www.mathworks.com/help/signal/ref/findchangepts.html` last accessed on May 4, 2021.

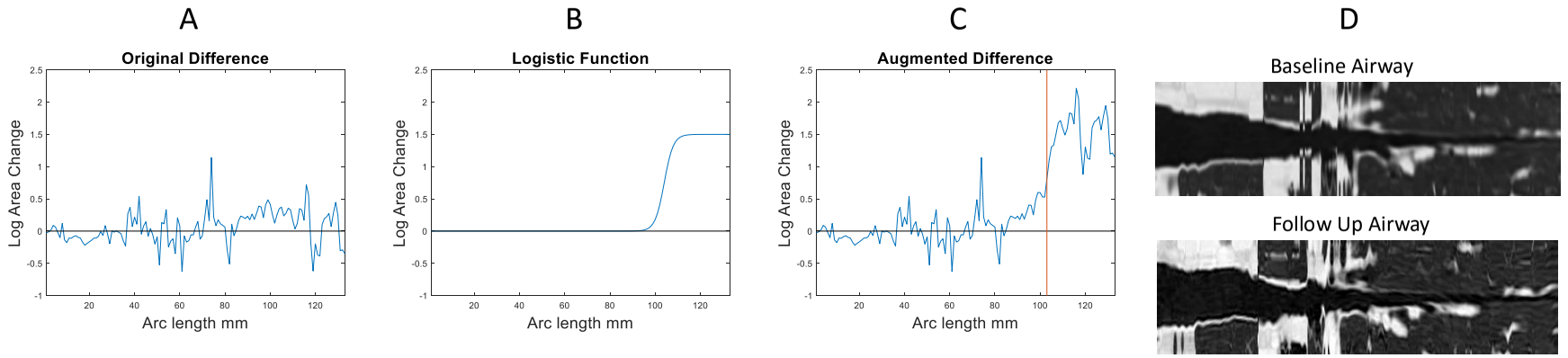

Figure 5.3: (A). An example of the area change of an airway remaining healthy on both baseline and follow-up scan. (B). A logistic function I constructed to simulate a dilatation due to IPF. (C). The augmented area change. The red line corresponds to our ground truth as the starting point of dilatation α. (D). The corresponding reconstructed airways.

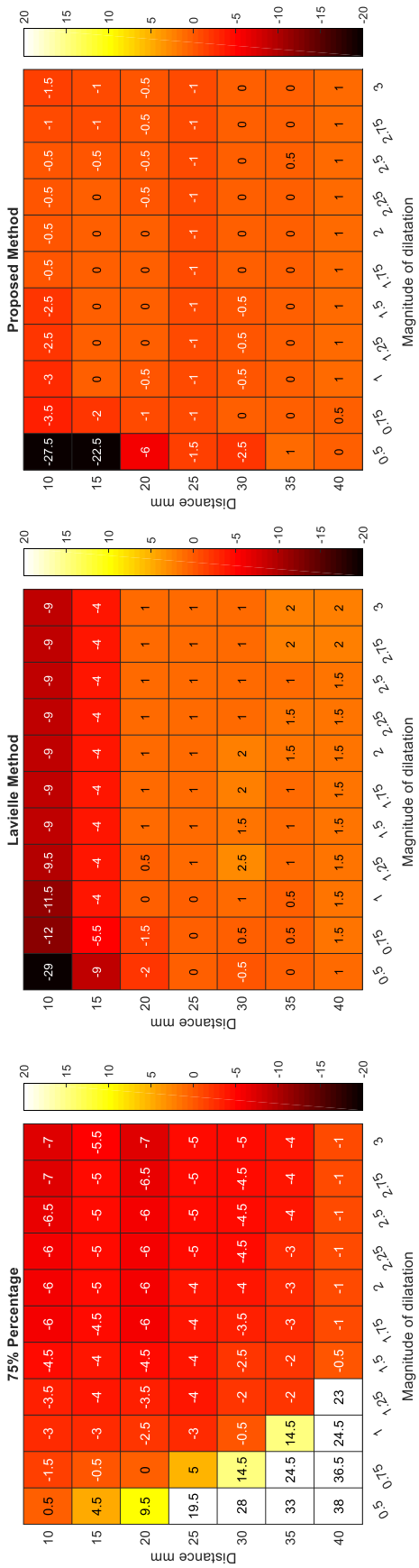

Figure 5.4: Heatmap showing the accuracy of each method. (Left). Thresholding method. (Middle). Method from Lavielle [6]. (Right). Our proposed method. The colour scale is the same on all of the heatmaps.

entry on the heatmap corresponds to the median average of all displacements over 14 airway pairs.

When the magnitude of dilation is larger than $M > 0.75$, our proposed method achieves consistently higher accuracy than Lavielle [6]. I note that the accuracy gain in the peripheral regions of the airways at $\alpha =$ 10-30mm from the distal point are the most clinically relevant in IPF as lung parenchymal damage begins in the lung periphery and progresses proximally [54]. Furthermore on the same peripheral regions $\alpha =$ 10-30mm, the baseline method showed systematic bias in accuracy towards the central airways. This was due to the baseline method being influenced by outliers from the longer expanses of normal airway regions. The proposed method uses the t-distribution as the likelihood thus making it robust to possible outliers within the data [150]. On the other hand, the proposed method suffers from poor accuracy below magnitudes of dilatation $M = 0.75$. However, in physical terms a dilatation of $M = 0.75$ corresponds to a percentage increase in cross sectional area of $e^{0.75} - 1 \approx 112\%$. This is within the range of normal biological change of the airways [143].

5.5.2 Application to Airways Affected by IPF

I applied our method to airways affected by IPF. The purpose was to compare our measurement to the labels provided by a radiologist and compute the volume change of the identified diseased airway regions. For our dataset, I acquired 4 airway pairs from 2 patients after obtained a waiver for consent from the local Research Ethics Committee. All airways were judged by the radiologist R1 to be dilated as a consequence of IPF on baseline and to have visually worsened on follow-up imaging. Image properties are displayed in Table 5.1.

I compared the performance of our method against two trained thoracic subspecialist radiologists. Two radiologists R1, R2 identified the point of at which a given airway was seen to demonstrate increased dilatation on the follow-up CT scan. To assessed the reproducibility of manual labeling, each radiologist labelled the same airway twice through two different protocols. In the first method, the radiologists interrogated axial CT images. Using 2 separate workstations and the airway

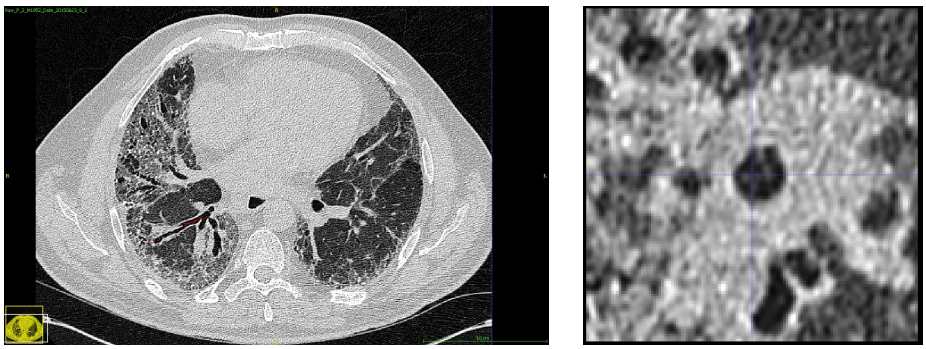

Figure 5.5: Example views of images in two measurement protocols employed by radiologists to locate starting points of dilatation. (Left). Protocol 1 based on the axial slice. (Right). Protocol 2 based on the reconstructed cross sectional planes.

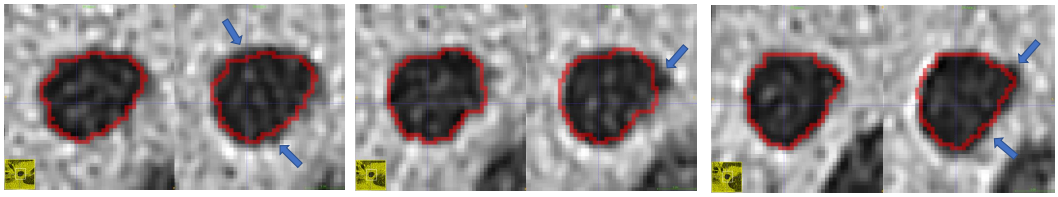

Figure 5.6: A row of three consecutive reconstructed slices in Airway 2 located on the arc length of 62-64mm. Each slice shows the airway lumen at baseline (left) and follow-up (right). The boundary delineation (red) from the baseline are superimposed on the follow-up scan. The blue arrows indicate pixels from the lumen outside the boundary.

centreline, the radiologists identified the point on the centreline (on the follow-up scan) where the airway demonstrated definitive worsened dilatation. For the second method, the radiologist compared the aligned reconstructed cross-sectional planes on baseline and follow-up scans. The radiologist then selected the slice where the airway had worsened when evaluated against the baseline scan. An example of both protocols are displayed on Figure 5.5.

Figure 5.7 compares the predictions of our method with the labels from radiologists obtained in two different protocols. The results indicate that the predictions for Airway 1, 3 and 4 are within the range of the radiologists' labels. In the case of Airway 2, although our method based on the maximum peak overestimates with respect to the radiologists' predictions, the posterior distribution contains another equally probable peak that underestimates the radiologists' labels (see the second highest peak at 70mm), potentially indicating a more proximal point of dilatation.

Airway	PVC of $V_{c\to d}$	PVC of $V_{t\to d}$	PVC of $V_{c\to t}$
1	2.6 %	32.9%	1.1%
2	3.2 %	129.7%	2.2%
3	2.6 %	47.4 %	-0.3%
4	7.4 %	48.4 %	7.1%

Table 5.2: The percentage volume change (PVC %) for each region of the airway.

To test this, I delineated the boundary of the lumen on the reconstructed cross sectional slices at baseline in the neighbouhood of this peak, and Figure 5.6 shows the initial few slices (62-64mm). I observed that, when the delineated boundary from baseline was superimposed on the follow-up scan, the boundary is contained inside of the follow-up lumen with several lumen pixels are consistently outside from the boundary. Thus, this result indicates that the starting point of dilatation is more proximal than the labels from the radiologists.

To demonstrate the clinical utility of locating the starting point of airway dilatation, I compared longitudinal airway volume changes in diseased and healthy regions of each of the airway tracks. To find the volume of the airway, I considered the aligned signals, f_{Base},f_{FoUp} as defined in Section 5.4.1. These signals are measurements of area against the airway arc length. Thus volume can be computed via the area under the curve. For our work, I used the trapezium rule to find the volume. Three volumetric regions were considered:

1. The entire airway $V_{c\to d}$ i.e. from the carina, c to the distal point, d.

2. The carina to the dilatation point t, denoted as $V_{c\to t}$.

3. The dilatation point to the distal point, denoted by $V_{t\to d}$.

Note that $V_{c\to d} = V_{c\to t} \cup V_{t\to d}$ and $V_{c\to t}$ does not overlap with $V_{t\to d}$. Table 5.2, shows the results of the percentage volume change. The volume change in $V_{t\to d}$ had greater sensitivity for selecting progressive airway dilatation in IPF than the volume change in the entire airway $V_{c\to d}$.

5.6 Discussion

In this paper, I modelled changes in area along airway tracks as a time series with the purpose of detecting abnormal dilatation caused by IPF using Bayesian changepoint detection. Experiments on simulated data show that our model is able to detect the starting location of airway dilatation with superior accuracy than the relevant baseline methods. The results on the IPF longitudinal dataset display reasonable agreement with radiologists, while in one case indicating a more plausible location of dilatation, potentially missed by the experts.

I aligned the transformed planar airways on follow up and baseline solely using the main bronchus and the area measurements. Various proposed methods in the literature used bifurcation points [152] or orientation of the airways [153]. However, these methods are not possible under incomplete segmentations or airways that are under a planar transformation. In terms of registration accuracy, my alignment method allowed radiologists to compare the planar reconstructed airway in Section 5.5.2, examples of aligned airways are shown in Figure 5.6.

5.6.1 Limitation

In this experiment, the airways with traction bronchiectasis were chosen on an ad hoc basis. The airways were chosen based on qualitative visual inspection by a trained radiologist. From our knowledge, there is no detailed clinically accepted quantification of the severity of traction bronchiectasis. Current studies use crude visual inspection to quantified the severity and progression of traction bronchiectasis [58].

5.7 Conclusion

Identifying changepoints and thereby calculating a change in airway dilatation over time could become a sensitive measure of IPF aggravation. This would form an important secondary endpoint in drug trials, where our measurements could indicate whether a new drug ameliorates disease progression better than existing medications [47]. In the future, I hope to evaluate such utility of our proposed method on a larger cohort of IPF subjects. Furthermore, our method is applicable to other lung airway

diseases, characterised by dilatation (such as cystic fibrosis) or other geometrical deformations, and such extensions remain valuable future work.

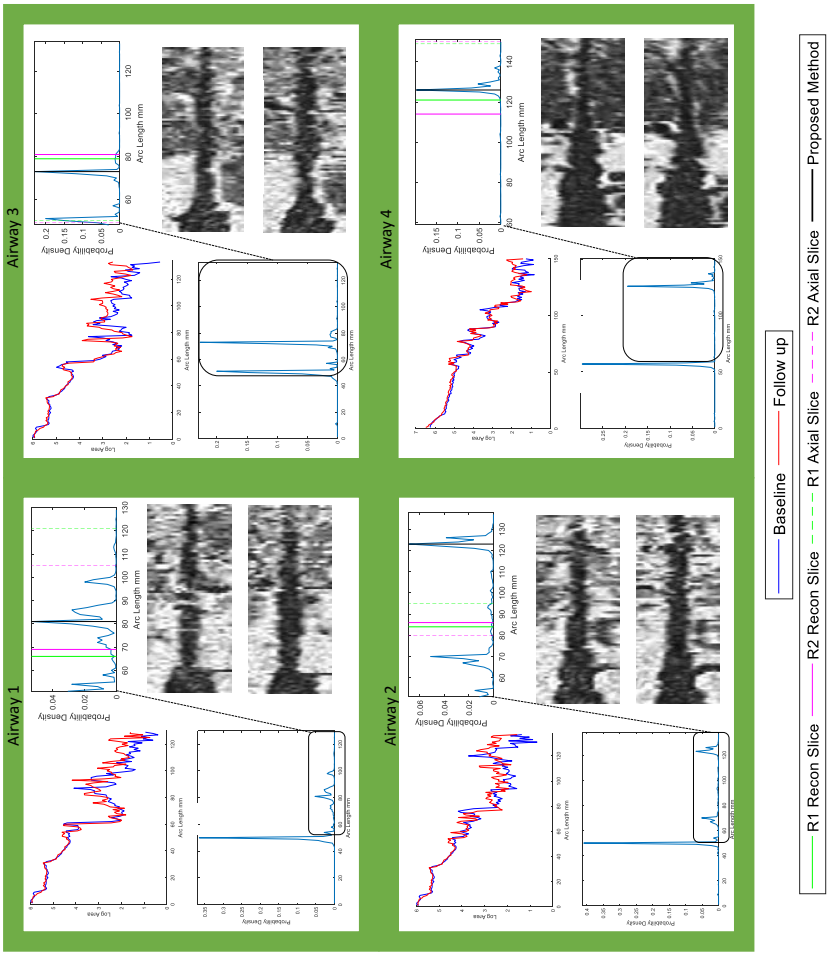

Figure 5.7: The log cross sectional area and posterior distribution $p(\tau|y)$ for each of the four airway pairs. Airways 1,2,3 come form the same patient. In the magnified region (black) I compared the labels from our proposed method with the radiologist. Furthermore, I displayed the reconstructed slices within the magnified region.

Chapter 6

Epilogue

6.1 Introduction

In this chapter, I summaries my contributions and propose future work. In this thesis, I showed the following contributions: (i) A proposed tapering measurement of the airway track with validation of accuracy and precision. (ii) An application of airway modelling using Bayesian Changepoint Analysis to determine the worsening of airway dilatation. The motivation is to provide computerized and robust measurements on airways affected by bronchiectasis or IPF. The chapter is organised as follows: (i) Summary of my contributions (Sec. 6.2). (ii) Clinical impact of my work (Sec. 6.3). (iii) Future work (Sec. 6.4). (iv) My closing remarks (Sec. 6.5).

6.2 Technical & Engineering Contributions

In this section, I present my technical and experimental contributions. They concern the following: (i) Assessing the accuracy of my image processing pipeline (Sec. 6.2.1). (ii) A tapering measuring and analysing its reproducibility against various acquisition parameters (Sec. 6.2.2). (iii) A novel application of the Bayesian Changepoint analysis to monitor progression of traction bronchiectasis (Sec. 6.2.3).

6.2.1 Accuracy of Pipeline

In this thesis, I proposed a pipeline to measure the cross-sectional areas along the airway track. Given an airway segmentation and labelled distal points, the pipeline

outputs a function of contiguous cross-sectional areas against the arclength of the airway. My contribution is a detailed validation of the accuracy of area measurements at contiguous intervals on phantoms on a clinical scanner.

In the experiment, I present two novelties for assessing the accuracy of airway lumen quantification: First, measuring the area at contiguous intervals along the 3D printed tubes. Second, I assessed the pipeline on phantoms with changes in diameter along the vessel. Previous experiments in the literature consist of measuring the phantom lumen at single or sparse intervals or on tubes with fixed diameters [117, 118].

My results showed the pipeline can measure to sub-voxel accuracy. In addition, the pipeline can detect changes in area along the airway lumen. The results can be used to infer the accuracy during post processing of measurements, such as to generate a tapering measure.

6.2.2 Tapering Measurement

I proposed a novel tapering measure to quantify the change in area along the airway track. The measurement is defined as the gradient of the linear regression between logarithmic area and arclength. The proposed measurement considers the entire airways track thus encapsulating all abnormal airway morphologies. My contribution is to show the tapering measurement gives a statistical difference between a set of healthy and bronchiectatic airways. Furthermore, I show the relationship between the precision of my proposed measurement and imaging parameters such as dose, voxel size and CT reconstruction. My results provide important calibration information for future clinical trials using my measurements.

6.2.3 Locating Abnormal Tapering

My contribution is introducing a novel application of Bayesian changepoint detection to identify the progression of dilatation along an airway track. The technical novelty involves modelling the change in cross-sectional area as a 1D signal and interpreting a progressive dilatation as a changepoint. Finally, we compute the volume change in the identified dilatated region – this is a novel interpretation of progres-

sion of traction bronchiectasis.

In terms of experimentation, I implemented a proof of principle validation using simulated and clinical data. The results showed an accuracy of locating dilatation to 2.5mm. Furthermore, on clinical data, the start of dilatation were in range or more proximal than the radiologists label. The method is technologically advance than the state of the art of monitoring IPF progression via visual inspection [154].

6.3 Clinical Impact

In this section, I discuss the possible impacts of my work on two airway diseases: bronchiectasis (Sec. 6.3.1) and IPF (Sec. 6.3.2).

6.3.1 Bronchiectasis

Bronchiectasis is a heterogeneous disease, the spatial location and magnitude of dilatation can vary between patients. Current severity and longitudinal analysis of bronchiectasis in CT images such as in McDonnell et al. [41] involves the use a variation of the Bhalla score [37]. The scoring system does not consider the dilatation of individual airways. Thus, possibly failing to detect subtle localised changes caused by the disease.

My work provides a computerized method to monitor airway dilatation caused by bronchiectasis for clinical research. Features that are included in the Bhalla score such as airway wall thickening, or mucus may not appear on every patient. By measuring explicitly the tapering of the airways, I can potentially relate the physical dilatation of the airway with frequency of exacerbation or mortality.

6.3.2 IPF

A principle feature in patients with IPF is traction bronchiectasis; the dilatation of the airways caused by contraction of fibrosing connective tissue. To my knowledge, there are no medical image computing methods that quantifies solely the progression of traction bronchiectasis across longitudinal scans. For my work, we quantified progression of IPF by the volume change of the diseased region. A possible impact is informing researchers of any anatomical processes in the dilatation of the

airways, possibly leading to improved understanding of the mechanisms of therapeutic agents. For example, the drug Nintedanib has proven effective at slowing progression of IPF. However, the drug was originally developed for cancer [155].

6.4 Future Work

In this section, I discuss possible future experiments from ideas proposed in this thesis. In Section 6.4.1 & 6.4.2, I discuss improvements and modifications to my proposed image analysis algorithms. In Section 6.4.3 & 6.4.4 I discuss possible future work combining my imaging measurement with other clinical data.

6.4.1 Applying Bayesian Changepoint Detection to Bronchiectatic Airway

From the review by Cantin et al. [101], the appearance of bronchiectasis can be classified as cylindric, varicose and cystic. The appearance can be distinguished by changes in cross sectional area along the centreline of the airways. For example, varicose bronchiectasis is characterised as a string of pearls appearance, cylindric bronchiectasis is characterised as a lack of tapering. Finally, cystic bronchiectasis is characterised as isotropic expansion of the airways.

In Chapter 5, I proposed a machine learning algorithm called Bayesian Changepoint Detection to determine changes in distribution of cross-sectional areas. The proposed method was applied to airways affected by IPF. I believe the methods can be applied to airways with bronchiectasis. I hypothesise that the appearance of cylindric, varicose and cystic bronchiectasis will display distinct changes of cross section areas along the arc length of the airway. Thus, the number and location of changepoints can be clustered to a particular appearance of bronchiectasis. The impact will be to quantify phenotypes of bronchiectasis.

In addition, Bayesian Changepoints Detection can locate possible dilatation along the airway. Thus, enabling topological analysis of bronchiectasis for example where the abnormal dilatation are at the proximal region of the lungs. The topology and location of bronchiectasis is clinical relevant for example the presentation of fungal lung disease; aspergillosis is characterise by proximal airway dilatation

[156]. Thus, topological information of bronchiectasis could be used a phenotype of the disease.

6.4.2 Applicability of Tapering Measurement to Clinical Studies

Patients with bronchiectasis in a clinical setting may have other pulmonary abnormalities such mucus plugging and collapsed lung [38]. These features can perturb the intensity of the CT image leading to image processing algorithms outputting spurious results. Thus, for any proposed image analysis algorithm to be applicable for clinical studies, one would have to consider the robustness of the algorithms to a wide range of anatomical abnormalities.

In Chapter 2, I proposed an airway tapering measurement to quantify bronchiectasis. My tapering measurement were taken from airway lumen without mucus. Thus, my tapering measurement can only be applied to ideal cases of bronchiectasis, making the measurement unsuitable for clinical studies. A possible future work would adapt the pipeline to measure airway lumen with mucus. Thus, the tapering measurement can be used on a wider range of patients.

Another obstacle for applicability of my tapering measurement is the use of manual segmentation of the airways thus, restricting evaluations to a small sample size. The state of art deep learning algorithms can only consistently segment airways to the fourth generation [102]. However, there is clinical interest in analysing proximal bronchiectasis [156]. Thus an approach to make my tapering measurement clinically viable would be to modify the tapering measurement to consider a shorter arc length.

6.4.3 The Efficacy of Partitioned Volume Change for IPF Progression

It has been shown that two drugs; Nintedanib and Pirfenidone are proven to be effective at slowing progression of IPF compared to placebo [50, 49]. However, there has been no head to head study to compare the comparative efficacy [47]. The clinical metrics used to quantify IPF progression in drug trials are lung function, walking distance and mortality [50, 49]. However, no imaging information has

been used for quantification of IPF progression. My proposed future work would apply the Bayesian changepoint on longitudinal scans for a head to head drug trials. The hypothesis being volume changes in the dilated regions are a more sensitive measure of progression. Thus, providing an alternative clinical end point.

6.4.4 Linking Frequency of Bronchiectatic Exacerbation with Tapering

It has been acknowledged that the number of exacerbations per year can predict the future risk of mortality [100]. The suggested work combines the tapering measurement with the history of the exacerbations. To proceed, I assume the availability of a dataset of bronchiectatic CT images with an associated number of exacerbations within a year. By exhaustively collecting the entire tapering values in the lungs, I can represent dilatations in an airway tree as a distribution of tapering values. Parameters in the distribution such as mean and standard deviation can be related to the frequency of exacerbation. My hypothesis is there is a relationship between the frequency of exacerbations and both in the number of enlarged airways and the magnitude of dilatation. Thus, there will be a difference in distribution parameters in patients that suffer frequent exacerbations compared to controls. The impact is the possibility of informing clinicians the likelihood if patient is at risk of an exacerbation based on CT images.

6.5 Conclusions

In this thesis, I developed methods to quantify and locate dilatation of airways in the lungs on CT. The motivation is to assist clinicians on assessing two diseases. First, to quantify airways affected by bronchiectasis. Second, to assess the progression of IPF by quantifying the change in traction bronchiectasis. I have used state of the art algorithms to measure the area of the airway lumen at contiguous intervals. In terms of experiments, I performed detailed validation of the repeatability and accuracy of my image processing pipeline. In addition, I show a proof of principle assessment of the accuracy and clinical utility of locating the point of increased dilatation on airways with IPF.

Appendix A

Reversible Jump Metropolis Hasting (RJMH)

A.1 Contribution

The entire contents of this chapter were developed and implemented by M Duong.

A.2 Introduction

As mentioned in Section 5.4.3, I am required to find a solutions to the following posterior distribution; $p(\tau|\mathbf{y})$. Where $\mathbf{y} = (y_1, \ldots, y_n)$ is the ordered area measurement, $\tau = (\tau_1, \ldots, \tau_n)$ is the changepoint location, M is the number of changepoints, $\theta = (\theta_1, \ldots, \theta n)$ are the segment parameters and for each $\theta_i = (\nu_l, \mu_l, \sigma_l)$ are the Student t distribution parameters.

A.3 Method Overview

The Reversible Jump Metropolis Hasting (RJMH) proceeds by randomly executing one of four possible moves, denoted as Υ_i at each iteration:

1. Resample parameters θ, Υ_θ.
2. Move an existing changepoint, Υ_τ.
3. Add a new changepoint, $\Upsilon_{M \to M+1}$.
4. Delete an existing changepoint, $\Upsilon_{M+1 \to M}$.

I also define the maximum number of changepoints k_{max} and at the boundary cases for k, I impose restrictions such that $\Upsilon_{M\to M+1}, \Upsilon_{M+1\to M}$ are skipped for $k = 0, k_{max}$ respectively. Each move updates the appropriate subset of parameters θ, τ by sampling from the corresponding distributions $q(\theta_{new}|\theta_{old})$ and $q(\tau_{new}|\tau_{old})$, and is only executed if it passes the associated acceptance criteria α.

A.3.1 Metropolis Hasting Steps

For Υ_θ, I set $q(\theta_{new}|\theta_{old}) = (\mu_{old}, \sigma^2_{old}, \nu_{old}) + \mathrm{N}(0, \varepsilon)$. This step resamples parameters of each segment by proposing Gaussian perturbations around the current values of parameters for all segments.

For Υ_τ, I set $q(\tau_{new}|\tau_{old}) = \tau_{old} + (-1)^b \mathrm{Poi}(\lambda)$ where $b \sim$Binary$[0,1]$. This step selects a changepoint τ at random and shifts it with a Poisson perturbation. The segments neighbouring this new changepoint location have parameters θ resampled as in move Υ_θ using the current segment parameters.

A.3.2 Reversible Jump Steps

For $\Upsilon_{M\to M+1}$, I proposed random new changepoints over our data, $\tau_{new} \sim \mathrm{U}[1, n-1]$. The proposed τ_{new} split an existing segment into a new left segment $\theta_l = (\mu_l, \sigma^2_l, \nu_l)$ and new right segment $\theta_r = (\mu_r, \sigma^2_r, \nu_r)$. Our proposal for μ_i, σ^2_i are defined by a Gaussian perturbation on empirical values of the respective $i = l, r$ segments (Fig. A.1). The proposal for ν_i, is Gaussian perturbation of the previous update ν_{old}. Due to dependence of the ν_i proposal, a Jacobian term is introduced $|J_{M\to M+1}| = 2$.

For $\Upsilon_{M+1\to M}$, I remove a changepoint τ_{new}. As before, proposals for $\mu_{new}, \sigma^2_{new}$ are defined using empirical values of the segments and Gaussian perturbation (Fig. A.1). The proposal for ν_{new} is the mean of the previous ν_l, ν_r. The move introduces Jacobian term $|J_{M+1\to M}| = 0.5$.

A.3.3 Parameters Choice & Implementation

With the algorithm now defined in detail, I close out this methodology with the choice of priors used. The prior for the given data set (simulated and airway) is given as follows: $\mu \sim \mathrm{N}(0,1)$, $\sigma^2 \sim$ Scaled-Inv-$\chi^2(5, 0.4^2)$, $\nu \sim \mathrm{U}[2, 100]$ and

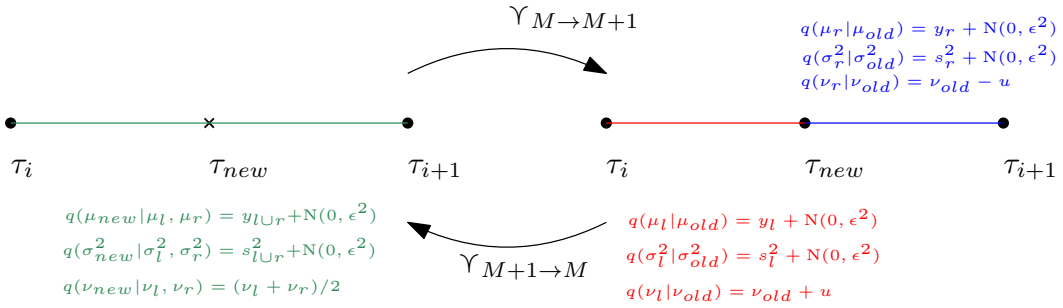

Figure A.1: A schematic diagram describing the proposals moves $\Upsilon_{M\to M+1}, \Upsilon_{M+1\to M}$. Note that $u \sim \mathrm{N}(0,\varepsilon^2)$ and y_i, s_i^2 are the mean and variance respectively of data within the coloured segment.

$M \sim \mathrm{Bin}(n-1, \frac{0.5}{n-1})$. The hyper-parameters for μ, σ^2, ν were chosen to be non-informative and within plausible ranges. In order to reduce the number of change points I could detect (in the case of acquisition noise), I set the expectation for M to be sufficiently low.

With the model defined, I address some common implementation techniques. I follow a standard procedure of setting a burn-in for the number of iterations to ignore any potential issues with intialisation at approximately 25% of the total iteration count. To remove any chance of auto-correlation, I thin the number of samples by only storing the 5^{th} iteration, after the burn-in period.

Algorithm 4 RJMH Changepoint Detection [147].

Data: Single airway time series data, $\mathbf{y} = (y_1, \ldots, y_n)$
Model Parameters: M = # changepoints, θ = segment parameters, τ= changepoint location
RJMCMC Parameters: N = iterations, B = burn-in, T = Thinning
Initialisation: Set $s = (M, \theta, \tau)$
Initialise set s with no changepoints and empirical segment parameters
for N iterations **do**
  Sample $\Upsilon_i \sim \text{Uniform}\{\Upsilon_\theta, \Upsilon_\tau, \Upsilon_{M\to M+1}, \Upsilon_{M+1\to M}\}$
  if $\Upsilon_i = \Upsilon_\theta$ **then**
    MH-step (1): Resample Segment Parameters
    Resample $\theta_{new} \sim q(\theta_{new}|\theta)$ for each segment
    Compute acceptance ratio: $\alpha = \min\left\{1, \frac{p(\mathbf{y}|\tau,\theta_{new},M)}{p(\mathbf{y}|\tau,\theta,M)} \frac{p(\theta_{new})}{p(\theta)} \frac{q(\theta|\theta_{new})}{q(\theta_{new}|\theta)}\right\}$
    Generate $\beta \sim \text{Uniform}[0,1]$
    if $\beta \geq \alpha$ **then**
      Accept new state
      $s = (M, \theta_{new}, \tau)$
    end if
  else if $\Upsilon_i = \Upsilon_\tau$ **then**
    MH-step (2): Move changepoint
    Move a changepoint $\tau_{new} \sim q(\tau_{new}|\tau)$ and propose new segment parameters $\theta_{new} \sim q(\theta_{new}|\theta)$
    Compute acceptance ratio: $\alpha = \min\left\{1, \frac{p(\mathbf{y}|\tau_{new},\theta_{new},M)}{p(\mathbf{y}|\tau,\theta,M)} \frac{p(\theta_{new})}{p(\theta)} \frac{q(\tau|\tau_{new})}{q(\tau_{new}|\tau)} \frac{q(\theta|\theta_{new})}{q(\theta_{new}|\theta)}\right\}$
    Generate $\beta \sim \text{Uniform}[0,1]$
    if $\beta \geq \alpha$ **then**
      Accept new state
      $s = (M, \theta_{new}, \tau_{new})$
    end if
  else if $\Upsilon_i = \Upsilon_{M\to M+1}$ **then**
    RJ-step (3): Add changepoint
    Propose new changepoint M_{new} as τ_{new} and propose new segment parameters θ_{new}
    Compute acceptance ratio

$$\alpha = \min\left\{1, \frac{p(\mathbf{y}|\tau_{new},\theta_{new},M_{new})}{p(\mathbf{y}|\tau,\theta,M)} \frac{p(\tau_{new})p(\theta_{new})p(M_{new})}{p(\tau)p(\theta)p(M)} \frac{q(\tau|\tau_{new})}{q(\tau_{new}|\tau)} \frac{q(\theta|\theta_{new})}{q(\theta_{new}|\theta)} \frac{q(M|M_{new})}{q(M_{new}|M)} |J_{M\to M+1}|\right\}$$

    where $|J_{M\to M+1}| = 2$ and $q(M_{new}|M)$ is symmetrical to $q(M|M_{new})$.
    Generate $v \sim \text{Uniform}[0,1]$
    if $v \geq \alpha$ **then**
      Accept new state
      $s = (M_{new}, \theta_{new}, \tau_{new})$
    end if
  else if $\Upsilon_i = \Upsilon_{M+1\to M}$ **then**
    RJ-step (4): Delete changepoint
    Delete a changepoint M_{new} as τ_{new} and propose new segment parameters θ_{new}
    Compute acceptance ratio

$$\alpha = \min\left\{1, \frac{p(\mathbf{y}|\tau new,\theta_{new},M_{new})}{p(\mathbf{y}|\tau,\theta,M)} \frac{p(\tau_{new})p(\theta_{new})p(M_{new})}{p(\tau)p(\theta)p(M)} \frac{q(\tau|\tau_{new})}{q(\tau_{new}|\tau)} \frac{q(\theta|\theta_{new})}{q(\theta_n ew|\theta)} \frac{q(M|M_{new})}{q(M_{new}|M)} |J_{M+1\to M}|\right\}$$

    where $|J_{M+1\to M}| = \frac{1}{2}$ and $q(M_{new}|M)$ is symmetrical to $q(M|M_{new})$.
    Generate $v \sim \text{Uniform}[0,1]$
    if $v \geq \alpha$ **then**
      Accept new state
      $s = (M_{new}, \theta_{new}, \tau_{new})$
    end if
  end if
end for
Remove first B samples and keep every T^{th} sample
Return: $\{s\}_{t=1}^{T}$

Appendix B

Summary of Publications

B.1 Journal Paper

- **K Quan**, R Tanno, R J Shipley, J S Brown, J Jacob, J R Hurst, D J Hawkes "Reproducibility of an airway tapering measurement in computed tomography with application to bronchiectasis" In *Journal of Medical Imaging*, 2019.

Abstract: We propose a pipeline to acquire a scalar tapering measurement from the carina to the most distal point of an individual airway visible on computed tomography (CT). We show the applicability of using tapering measurements on clinically acquired data by quantifying the reproducibility of the tapering measure. We generate a spline from the centerline of an airway to measure the area and arclength at contiguous intervals. The tapering measurement is the gradient of the linear regression between area in log space and arclength. The reproducibility of the measure is assessed by analyzing different radiation doses, voxel sizes, and reconstruction kernel on single timepoint and longitudinal CT scans and by evaluating the effect of airway bifurcations. Using 74 airways from 10 CT scans, we show a statistical difference, p = 3.4×10^{-4} in tapering between healthy airways (n = 35) and those affects by bronchiectasis (n = 39). The difference between the mean of the two populations is 0.011mm^{-1}, and the difference between the medians of the two populations is 0.006mm^{-1}. The tapering measurement

retains a 95% confidence interval of $\pm 0.005\text{mm}^{-1}$ in a simulated 25mAs scan and retains a 95% confidence of $\pm 0.005\text{mm}^{-1}$ on simulated CTs up to 1.5 times the original voxel size. We have established an estimate of the precision of the tapering measurement and estimated the effect on precision of the simulated voxel size and CT scan dose. We recommend that the scanner calibration be undertaken with the phantoms as described, on the specific CT scanner, radiation dose, and reconstruction algorithm that are to be used in any quantitative studies.

B.2 Conference Proceedings

- **K Quan**, R J Shipley, R Tanno, G McPhillips, V Vavourakis, D Edwards, J Jacob, J R Hurst, D J Hawkes, "Tapering analysis of airways with bronchiectasis." In *Proceedings of SPIE*, 2018.

Abstract: Bronchiectasis is the permanent dilation of airways. Patients with the disease can suffer recurrent exacerbations, reducing their quality of life. The gold standard to diagnose and monitor bronchiectasis is accomplished by inspection of chest computed tomography (CT) scans. A clinician examines the broncho-arterial ratio to determine if an airway is brochiectatic. The visual analysis assumes the blood vessel diameter remains constant, although this assumption is disputed in the literature. We propose a simple measurement of tapering along the airways to diagnose and monitor bronchiectasis. To this end, we constructed a pipeline to measure the cross-sectional area along the airways at contiguous intervals, starting from the carina to the most distal point observable. Using a phantom with calibrated 3D printed structures, the precision and accuracy of our algorithm extends to the sub voxel level. The tapering measurement is robust to bifurcations along the airway and was applied to chest CT images acquired in clinical practice. The result is a statistical difference in tapering rate between airways with bronchiectasis and controls.

- **K Quan**, R Tanno, M Duong, A Nair, R Shipley, M Jones, C Brereton, J Hurst, D Hawkes, J Jacob, "Modelling Airway Geometry as Stock Market Data using Bayesian Changepoint Detection", In *10th International Workshop on Machine Learning in Medical Imaging*, 2019.

Abstract: Numerous lung diseases, such as idiopathic pulmonary fibrosis (IPF), exhibit dilation of the airways. Accurate measurement of dilatation enables assessment of the progression of disease. Unfortunately the combination of image noise and airway bifurcations causes high variability in the profiles of cross-sectional areas, rendering the identification of affected regions very difficult. Here we introduce a noise-robust method for automatically detecting the location of progressive airway dilatation given two profiles of the same airway acquired at different time points. We propose a probabilistic model of abrupt relative variations between profiles and perform inference via Reversible Jump Markov Chain Monte Carlo sampling. We demonstrate the efficacy of the proposed method on two datasets; (i) images of healthy airways with simulated dilatation; (ii) pairs of real images of IPF-affected airways acquired at 1 year intervals. Our model is able to detect the starting location of airway dilatation with an accuracy of 2.5mm on simulated data. The experiments on the IPF dataset display reasonable agreement with radiologists. We can compute a relative change in airway volume that may be useful for quantifying IPF disease progression.

B.3 Conference Abstract

- **K Quan**, J Jacob, R J Shipley, D J Hawkes, J R Hurst, "Airway tapering in bronchiectatic and healthy airways." *European Respiratory Journal*, 52: Suppl. 62, OA3793, 2018.

Abstract:

Introduction: Bronchiectasis is the permanent dilatation of airways. The

gold standard for diagnosing bronchiectasis is increased broncho-arterial diameter ratio on CT. Increase in ratio assumes that the pulmonary artery remains constant. This assumption is disputed (Diaz, A.A. et al. Chest 2017 Jun, 151(6):1255-1262).

Aim: We show a statistical difference in the tapering measurement between a radiologically healthy airway and a bronchiectatic airway. The tapering measurement is independent of blood vessel and lobar location.

Methods: A pipeline was constructed to measure the cross-sectional lumen at contiguous intervals along the centreline from the carina to the most distal point visible on CT. The output is a scalar value describing the exponential decay of area as a function of distance along the airway. We applied the pipeline to a group of 35 healthy and 39 bronchiectatic airways identified by an expert radiologist. We then applied the pipeline to 14 pairs of healthy airways from paired longitudinal scans taken at least 5 months apart.

Results: The first experiment showed bronchiectatic airways have a reduction in taper rate (mean 3.17×10^{-2} vs. 2.11×10^{-2}/mm, p = 7.1×10^{-7}). The second experiment shows a good agreement with ICC $>$ 0.99 between the two sets and standard deviation of the tapering difference is 1.45×10^{-3}/mm.

Conclusions: We present a proof of principle study that tapering rate in a bronchiectatic airway is different to healthy airways and that healthy airways do not differ over time. Our technique provides the potential for use in the diagnosis of bronchiectasis, and the assessment of progression of bronchiectasis over time.

Bibliography

[1] J M Bland and D G Altman. Statistical methods for assessing agreement between two methods of clinical measurement. *The Lancet*, 327(8476):307–310, 1986.

[2] Kin Quan, Rebecca J. Shipley, Ryutaro Tanno, Graeme McPhillips, Vasileios Vavourakis, David Edwards, Joseph Jacob, John R. Hurst, and David J. Hawkes. Tapering analysis of airways with bronchiectasis. *Proceedings of SPIE*, 10574:105742G, 2018.

[3] Tsuyoshi Oguma, Toyohiro Hirai, Motonari Fukui, Naoya Tanabe, Satoshi Marumo, Hajime Nakamura, Hisao Ito, Susumu Sato, Akio Niimi, Isao Ito, Hisako Matsumoto, Shigeo Muro, and Michiaki Mishima. Longitudinal shape irregularity of airway lumen assessed by CT in patients with bronchial asthma and COPD. *Thorax*, 70(8):1–6, aug 2015.

[4] Rahul Prasanna Kumar, Fritz Albregtsen, Martin Reimers, Bjørn Edwin, Thomas Langø, and Ole Jakob Elle. Three-dimensional blood vessel segmentation and centerline extraction based on two-dimensional cross-section analysis. *Annals of Biomedical Engineering*, 43(5):1223–1234, 2015.

[5] L Alvarez, A Trujillo, C Cuenca, E González, J Esclarín, L Gomez, L Mazorra, M Alemán-Flores, P G Tahoces, and J M Carreira. Tracking the aortic lumen geometry by optimizing the 3D orientation of its cross-sections. In *Medical Image Computing and Computer-Assisted Intervention*, 2017.

[6] Marc Lavielle. Using penalized contrasts for the change-point problem. *Signal Processing*, 85(8):1501–1510, 2005.

[7] Pippa McGowan, Angus Jeffries, and Andrew Turley. *Respiratory System*. Elsevier, 2003.

[8] Richard Drake, A Wayne Vogl, and Mitchell Adam. *Gray's Anatomy for Students*. Elsevier, 2010.

[9] E R Weibel. *Morphometry of the Human Lung*. Springer, 1963.

[10] John Burnard West. *Respiratory Physiology: The Essentials*. Lippincott Williams & Wilkins, 2000.

[11] James Ambrose. Computerized transverse axial scanning (tomography): part 2 clinical application. *British Journal of Radiology*, 46(552):1023–1047, dec 1973.

[12] M C Pasteur, D Bilton, and A T Hill. British Thoracic Society guideline for non-CF Bronchiectasis. *Thorax*, 65:i1–i58, 2010.

[13] G Raghu, M Remy-Jardin, J L Myers, L Richeldi, C J Ryerson, D J Lederer, J Behr, V Cottin, S K Danoff, F Morell, K R Flaherty, A Wells, F J Martinez, A Azuma, T J Bice, D Bouros, K K Brown, H R Collard, A Duggal, L Galvin, Y Inoue, R G Jenkins, T Johkoh, E A Kazerooni, M Kitaichi, S L Knight, G Mansour, A G Nicholson, S N J Pipavath, I Buendía-Roldán, M Selman, W D Travis, S Walsh, and K C Wilson. Diagnosis of Idiopathic Pulmonary Fibrosis. An Official ATS/ERS/JRS/ALAT Clinical Practice Guideline. *American Journal of Respiratory and Critical Care Medicine*, 198(5):e44–e68, 2018.

[14] Willi Kalender. *Computed Tomography: Fundamentals, System Technology, Image Quality, Applications*. Publicis Publishing, 2011.

[15] P P Dendy and B Heaton. *Physics for Diagnostic Radiology*. Taylor and Francis, 1999.

[16] S. Webb. *The Physics of Medical Imaging*. CRC Press, 1988.

[17] J Hsieh. *Computed tomography: principles, design, artifacts, and recent advances*. SPIE & Wiley-interscience, 2009.

[18] Joseph V. Hajnal, David J. Hawkes, and Derek L. G. Hill. *Medical Image Registration*. CRC Press, 2001.

[19] Anna Fabijańska. Two-pass region growing algorithm for segmenting airway tree from MDCT chest scans. *Computerized Medical Imaging and Graphics*, 33(7):537–546, 2009.

[20] O Weinheimer, T Achenbach, C Bletz, C Duber, H U Kauczor, and C P Heussel. About objective 3-d analysis of airway geometry in computerized tomography. *IEEE Transactions on Medical Imaging*, 27(1):64–74, jan 2008.

[21] Stanislav Žabić, Qiu Wang, Thomas Morton, and Kevin M. Brown. A low dose simulation tool for CT systems with energy integrating detectors. *Medical Physics*, 40(3):031102–1–14, 2013.

[22] Anthony P. Reeves, Yiting Xie, and Shuang Liu. Automated image quality assessment for chest CT scans. *Medical Physics*, 45(2):561–578, 2017.

[23] Xin Meng, Yongqian Qiang, Shaocheng Zhu, Carl Fuhrman, Jill M Siegfried, and Jiantao Pu. Illustration of the obstacles in computerized lung segmentation using examples. *Medical physics*, 39(8):4984–91, aug 2012.

[24] R Wiemker, A Ekin, R Opfer, T Bülow, and P Rogalla. Unsupervised extraction and quantification of the bronchial tree on ultra-low-dose vs. standard dose CT. In *Proceedings of SPIE*, 2006.

[25] Tobias Achenbach, Oliver Weinheimer, Christoph Dueber, and Claus Peter Heussel. Influence of pixel size on quantification of airway wall thickness in computed tomography. *Journal of Computer Assisted Tomography*, 33(5):725–730, 2009.

[26] Qingsong Yang, Pingkun Yan, Yanbo Zhang, Hengyong Yu, Yongyi Shi, Xuanqin Mou, Mannudeep K. Kalra, Yi Zhang, Ling Sun, and Ge Wang. Low-Dose CT Image Denoising Using a Generative Adversarial Network With Wasserstein Distance and Perceptual Loss. *IEEE Transactions on Medical Imaging*, 37(6):1348–1357, 2018.

[27] Thomas Humphries, Sean Coulter, Dong Si, Matthew Simms, and Ruiwen Xing. Comparison of deep learning approaches to low dose CT using low intensity and sparse view data. In *SPIE Medical Imaging*, 2019.

[28] Jelmer M. Wolterink, Tim Leiner, Max A. Viergever, and Ivana Išgum. Generative adversarial networks for noise reduction in low-dose CT. *IEEE Transactions on Medical Imaging*, 36(12):2536–2545, 2017.

[29] James D Chalmers, Stefano Aliberti, and Francesco Blasi. State of the art review: management of bronchiectasis in adults. *The European Respiratory Journal*, 45(5):1446–1462, 2015.

[30] Guillermo Suarez-Cuartin, James D. Chalmers, and Oriol Sibila. Diagnostic challenges of bronchiectasis. *Respiratory Medicine*, 116:70–77, 2016.

[31] James D Chalmers and Adam T Hill. Mechanisms of immune dysfunction and bacterial persistence in non-cystic fibrosis bronchiectasis. *Molecular Immunology*, 55(1):27–34, aug 2013.

[32] P J Cole. Inflammation: a two-edged sword – the model of bronchiectasis. *European Journal of Respiratory Diseases*, 147:6–15, 1986.

[33] James D Chalmers, Anne B Chang, Sanjay H Chotirmall, Raja Dhar, and Pamela J McShane. Bronchiectasis. *Nature Reviews Disease Primers*, 4(45), 2018.

[34] James D Chalmers, Michael Loebinger, and Stefano Aliberti. Challenges in the development of new therapies for bronchiectasis. *Expert Opinion on Pharmacotherapy*, 16(6):833–850, mar 2015.

[35] Adam T. Hill, Charles S. Haworth, Stefano Aliberti, Alan Barker, Francesco Blasi, Wim Boersma, James D. Chalmers, Anthony De Soyza, Katerina Dimakou, J. Stuart Elborn, Charles Feldman, Patrick Flume, Pieter C. Goeminne, Michael R. Loebinger, Rosario Menendez, Lucy Morgan, Marlene Murris, Eva Polverino, Alexandra Quittner, Felix C. Ringshausen, Gregory Tino, Antoni Torres, Montserrat Vendrell, Tobias Welte, Rob Wilson, Conroy Wong, Anne O'Donnell, and Timothy Aksamit. Pulmonary exacerbation in adults with bronchiectasis: a consensus definition for clinical research. *The European Respiratory Journal*, 49(6), 2017.

[36] James D. Chalmers. Bronchiectasis exacerbations are heart-breaking. *Annals of the American Thoracic Society*, 15(3):301–303, 2018.

[37] M Bhalla, N Turcios, V Aponte, M Jenkins, B S Leitman, D I McCauley, and D P Naidich. Cystic fibrosis: scoring system with thin-section CT. *Radiology*, 179:783–788, 1991.

[38] James D. Chalmers, Pieter Goeminne, Stefano Aliberti, Melissa J. McDonnell, Sara Lonni, John Davidson, Lucy Poppelwell, Waleed Salih, Alberto Pesci, Lieven J. Dupont, Thomas C. Fardon, Anthony De Soyza, and Adam T. Hill. The bronchiectasis severity index an international derivation and validation study. *American Journal of Respiratory and Critical Care Medicine*, 189(5):576–585, 2014.

[39] D B Reiff, A U Wells, D H Carr, P J Cole, and D M Hansell. CT findings in bronchiectasis: limited value in distinguishing between idiopathic and specific types. *AJR. American journal of roentgenology*, 165(2):261–7, aug 1995.

[40] Miguel Á Martínez-García, Javier de Gracia, Monserrat Vendrell Relat, Rosa-Maria Girón, Luis Máiz Carro, David de la Rosa Carrillo, and Casilda Olveira. Multidimensional approach to non-cystic fibrosis bronchiectasis: the FACED score. *European Respiratory Journal*, 43(5):1357–67, may 2014.

[41] Melissa J. McDonnell, Stefano Aliberti, Pieter C. Goeminne, Marcos I. Restrepo, Simon Finch, Alberto Pesci, Lieven J. Dupont, Thomas C. Fardon, Robert Wilson, Michael R. Loebinger, Dusan Skrbic, Dusanka Obradovic, Anthony De Soyza, Chris Ward, John G. Laffey, Robert M. Rutherford, and James D. Chalmers. Comorbidities and the risk of mortality in patients with bronchiectasis: an international multicentre cohort study. *The Lancet Respiratory Medicine*, 4(12):969–979, 2016.

[42] M. J. McDonnell, S. Aliberti, P. C. Goeminne, K. Dimakou, S. C. Zucchetti, J. Davidson, C. Ward, J. G. Laffey, S. Finch, A. Pesci, L. J. Dupont, T. C. Fardon, D. Skrbic, D. Obradovic, S. Cowman, M. R. Loebinger, R. M. Rutherford, A. De Soyza, and J. D. Chalmers. Multidimensional severity assessment in bronchiectasis: An analysis of seven European cohorts. *Thorax*, 71(12):1110–1118, 2016.

[43] Aarash D Saleh and John R Hurst. How to assess the severity of bronchiectasis. *The European Respiratory Journal*, 43(5):1217–9, may 2014.

[44] Wei Jie Guan, Rong Chang Chen, and Nan Shan Zhong. The bronchiectasis severity index and FACED score for bronchiectasis. *European Respiratory Journal*, 47(2):382–384, 2016.

[45] J. C. Costa, J. N. Machado, C. Ferreira, J. Gama, and C. Rodrigues. The Bronchiectasis Severity Index and FACED score for assessment of the severity of bronchiectasis. *Pulmonology*, 24(3):149–154, 2018.

[46] James D. Chalmers. Bronchiectasis and COPD overlap: A case of mistaken identity? *Chest*, 151(6):1204–1206, 2017.

[47] D J Lederer and F J Martinez. Idiopathic pulmonary fibrosis. *The New England Journal of Medicine*, 378(19):1811–1823, 2018.

[48] Luca Richeldi, Harold R Collard, and Mark G Jones. Idiopathic Pulmonary Fibrosis. *The Lancet*, 389:1941–1952, 2017.

[49] L Richeldi, R M du Bois, Ganesh Raghu, Arata Azuma, Kevin K. Brown, Ulrich Costabel, Vincent Cottin, Kevin R Flaherty, David M. Hansell, Yoshikazu Inoue, Dong Soon Kim, Martin Kolb, Andrew G. Nicholson, Paul W. Noble, Moisés Selman, Hiroyuki Taniguchi, Michèle Brun, Florence Le Maulf, Mannaïg Girard, Susanne Stowasser, Rozsa Schlenker-Herceg, Bernd Disse, and Harold R. Collard. Efficacy and safety of nintedanib in advanced idiopathic pulmonary fibrosis. *New England Journal of Medicine*, 370(22):2071–2082, 2014.

[50] Talmadge E. King, Williamson Z. Bradford, Socorro Castro-Bernardini, Elizabeth A. Fagan, Ian Glaspole, Marilyn K. Glassberg, Eduard Gorina, Peter M. Hopkins, David Kardatzke, Lisa Lancaster, David J. Lederer, Steven D. Nathan, Carlos A. Pereira, Steven A. Sahn, Robert Sussman, Jeffrey J. Swigris, and Paul W. Noble. A Phase 3 Trial of Pirfenidone in Patients with Idiopathic Pulmonary Fibrosis. *New England Journal of Medicine*, 370(22):2083–2092, 2014.

[51] Kathleen O. Lindell, Zhan Liang, Leslie A. Hoffman, Margaret Q. Rosenzweig, Melissa I. Saul, Joseph M. Pilewski, Kevin F. Gibson, and Naftali Kaminski. Palliative care and location of death in decedents with idiopathic pulmonary fibrosis. *Chest*, 147(2):423–429, 2015.

[52] Christopher S. King and Steven D. Nathan. POINT: Should All Patients With Idiopathic Pulmonary Fibrosis, Even Those With More Than Moderate Impairment, Be Treated With Nintedanib or Pirfenidone? Yes. *Chest*, 150(2):273–275, 2016.

[53] D A Lynch, N Sverzellati, W D Travis, K K Brown, T V Colby, J R Galvin, J G Goldin, D M Hansell, Y Inoue, T Johkoh, A G Nicholson, S L Knight, S Raoof, L Richeldi, C J Ryerson, J R Ryu, and A U Wells. Diagnostic Criteria for Idiopathic Pulmonary Fibrosis: A Fleischner Society White Paper. *The Lancet Respiratory*, 6:138–153, 2018.

[54] Joseph Jacob and David M. Hansell. HRCT of fibrosing lung disease. *Respirology*, 20(6):859–872, 2015.

[55] David A. Lynch, J. David Godwin, Sharon Safrin, Karen M. Starko, Phil Hormel, Kevin K. Brown, Ganesh Raghu, Talmadge E. King, Williamson Z. Bradford, David A. Schwartz, and W. Richard Webb. High-resolution computed tomography in idiopathic pulmonary fibrosis: Diagnosis and prognosis. *American Journal of Respiratory and Critical Care Medicine*, 172(4):488–493, 2005.

[56] Joseph Jacob, Brian J. Bartholmai, Ryoko Egashira, Anne Laure Brun, Srinivasan Rajagopalan, Ronald Karwoski, Maria Kokosi, David M. Hansell, and Athol U. Wells. Chronic hypersensitivity pneumonitis: Identification of key prognostic determinants using automated CT analysis. *BMC Pulmonary Medicine*, 17(1):1–12, 2017.

[57] Fabien Maldonado, Teng Moua, Srinivasan Rajagopalan, Ronald A Karwoski, Sushravya Raghunath, Paul A Decker, Thomas E Hartman, Brian J Bartholmai, Richard A Robb, and Jay H Ryu. Automated quantification of radiological patterns predicts survival in idiopathic pulmonary fibrosis. *European Respiratory Journal*, pages 204–212, 2014.

[58] Joseph Jacob, Brian J. Bartholmai, Srinivasan Rajagopalan, Maria Kokosi, Ryoko Egashira, Anne Laure Brun, Arjun Nair, Simon L.F. Walsh, Ronald Karwoski, and Athol U. Wells. Serial automated quantitative CT analysis in idiopathic pulmonary fibrosis: functional correlations and comparison with changes in visual CT scores. *European Radiology*, 28(3):1318–1327, 2018.

[59] Joseph Jacob, Brian J. Bartholmai, Srinivasan Rajagopalan, Maria Kokosi, Arjun Nair, Ronald Karwoski, Sushravya M. Raghunath, Simon L. Walsh, Athol U. Wells, and David M. Hansell. Automated quantitative computed tomography versus visual computed tomography scoring in idiopathic pul-

monary fibrosis validation against pulmonary function. *Journal of Thoracic Imaging*, 31(5):304–311, 2016.

[60] Daniel Y. Chong, Pechin Lo, Stefano Young, Michael F. McNitt-Gray, Fereidoun Abtin, Jonathan G. Goldin, Matthew S. Brown, and Hyun J. Kim. Robustness-Driven Feature Selection in Classification of Fibrotic Interstitial Lung Disease Patterns in Computed Tomography Using 3D Texture Features. *IEEE Transactions on Medical Imaging*, 35(1):144–157, 2016.

[61] Erkan Ü Mumcuolu, Frederick R. Long, Robert G. Castile, and Metin N. Gurcan. Image analysis for cystic fibrosis: Computer-assisted airway wall and vessel measurements from low-dose, limited scan lung CT images. *Journal of Digital Imaging*, 26:82–96, 2013.

[62] Adria Perez-Rovira, Wieying Kuo, Jens Petersen, Harm A W M Tiddens, and Marleen De Bruijne. Automatic airwayartery analysis on lung CT to quantify airway wall thickening and bronchiectasis. *Medical Physics*, 43(10):5736–5744, 2016.

[63] Catalin Fetita, Pierre-Yves Brillet, Christopher Brightling, and Philippe A. Grenier. Grading remodeling severity in asthma based on airway wall thickening index and bronchoarterial ratio measured with MSCT. *Proceedings of SPIE*, 9415:941515, 2015.

[64] David M Hansell. Thin-section CT of the lungs: the Hinterland of normal. *Radiology*, 256(3):695–711, 2010.

[65] Joung Sook Kim, N L Muller, Chan Sup Park, David A. Lynch, Lee S. Newman, Philippe Grenier, and Christian J. Herold. Bronchoarterial ratio on thin section CT: comparison between high altitude and sea level. *Journal of Computer Assisted Tomography*, 21(2):306–311, 1997.

[66] Shin Matsuoka, Katsuhiro Uchiyama, Hideki Shima, Naoyuki Ueno, Sonomi Oish, and Yoko Nojiri. Bronchoarterial ratio and bronchial wall thickness

on high-resolution CT in asymptomatic subjects: Correlation with age and smoking. *American Journal of Roentgenology*, 180(2):513–518, 2003.

[67] Alejandro A. Diaz, Thomas P. Young, Diego J. Maselli, Carlos H. Martinez, Ritu Gill, Pietro Nardelli, Wei Wang, Gregory L. Kinney, John E. Hokanson, George R. Washko, and Raul San Jose Estepar. Quantitative CT measures of bronchiectasis in smokers. *Chest*, 151(6):1255–1262, 2017.

[68] Veronika Cheplygina, Adria Perez-rovira, Wieying Kuo, Harm A W M Tiddens, and Marleen De Bruijne. Early Experiences with Crowdsourcing Airway Annotations in Chest CT. In *International Workshop on Large-Scale Annotation of Biomedical Data and Expert Label Synthesis*, 2016.

[69] Benjamin L. Odry, Atilla P Kiraly, Carol L Novak, David P Naidich, and Jean-Francois Lerallut. Automated airway evaluation system for multi-slice computed tomography using airway lumen diameter, airway wall thickness and broncho-arterial ratio. *Proceedings of SPIE*, 6143:61430Q, 2006.

[70] Raman Venkatraman, Raghav Raman, Bhargav Raman, Richard B. Moss, Geoffrey D. Rubin, Lawrence H. Mathers, and Terry E. Robinson. Fully automated system for three-dimensional bronchial morphology analysis using volumetric multidetector computed tomography of the chest. *Journal of Digital Imaging*, 19(2):132–139, 2006.

[71] Oliver Weinheimer, Mark O Wielp, Hans-Ulrich Kauczor, Christoph Brochhausen, David Hollemann, Dasha Savage, and J Craig. Fully automated lobe-based airway taper index calculation in a low dose MDCT CF study over 4 time-points. *Proceedings of SPIE*, 10133:101330U, 2017.

[72] Eva M. van Rikxoort, Baggerman Wouter, and Bram Van Ginneken. Automatic segmentation of the airway tree from thoracic CT scans using a multi-threshold approach. In *The First International Workshop on Pulmonary Image Analysis*, 2009.

[73] Kálmán Palágyi, Juerg Tschirren, Eric A Hoffman, and Milan Sonka. Quantitative analysis of pulmonary airway tree structures. *Computers in Biology and Medicine*, 36(9):974–996, 2006.

[74] S.R. Aylward and E. Bullitt. Initialization, noise, singularities, and scale in height ridge traversal for tubular object centerline extraction. *IEEE Transactions on Medical Imaging*, 21(2):61–75, 2002.

[75] Kensaku Mori, Jun Ichi Hasegawa, Yasuhito Suenaga, and Jun Ichiro Toriwaki. Automated anatomical labeling of the bronchial branch and its application to the virtual bronchoscopy system. *IEEE Transactions on Medical Imaging*, 19(2):103–114, 2000.

[76] Thomas H Cormen, Charles E Leiserson, Ronald L Rivest, and Clifford Stein. *Introduction to algorithms*. MIT Press, 2009.

[77] Florent Grélard, Fabien Baldacci, Anne Vialard, and Jean Philippe Domenger. New methods for the geometrical analysis of tubular organs. *Medical Image Analysis*, 42:89–101, 2017.

[78] Benjamin J. Irving, Pierre Goussard, Savvas Andronikou, Robert Gie, Tania S. Douglas, Andrew Todd-Pokropek, and Paul Taylor. Computer assisted detection of abnormal airway variation in CT scans related to paediatric tuberculosis. *Medical Image Analysis*, 18(7):963–976, 2014.

[79] Erwin Kreyszig. *Advanced Engineering Mathematics*. John Wiley & Sons, 1964.

[80] Steven J. Leon. *Linear Algebra with Applications*. Pearson Prentice Hall, 2009.

[81] Peter Shirley and Steve Marschner. *Fundamentals of computer graphics*. A K Peters, 2009.

[82] Atilla P. Kiraly, Joseph M. Reinhardt, Eric a. Hoffman, Geoffrey McLennan, and William E. Higgins. Virtual bronchoscopy for quantitative airway analysis. In *Proceedings of SPIE*, 2005.

[83] Andrew W Fitzgibbon, Maurizio Pilu, and Robert B Fisher. Direct least squares fitting of ellipses. In *Proceedings of 13th International Conference on Pattern Recognition*, 1996.

[84] Andrey I Nikiforov and Richard B Schlesinger. Morphometric variability of the human upper bronchial tree. *Respiration Physiology*, 59(3):289–299, 1985.

[85] Md K Azad, Hansen A Mansy, and Peshala T Gamage. Geometric features of pig airways using computed tomography. *Physiological Reports*, 4(20):e12995, 2016.

[86] D L Streiner, G R Norman, and J Cariney. *Health Measurement Scales: A practical guide to their development and use*. Oxford University Press, 2015.

[87] Dakai Jin, Krishna S. Iyer, Cheng Chen, Eric A. Hoffman, and Punam K. Saha. A robust and efficient curve skeletonization algorithm for tree-like objects using minimum cost paths. *Pattern Recognition Letters*, 76:32–40, 2016.

[88] Ruben Cardenes, Hrvoje Bogunovic, and Alejandro F. Frangi. Fast 3D centerline computation for tubular structures by front collapsing and fast marching. In *2010 IEEE International Conference on Image Processing*, sep 2010.

[89] A. P. Kiraly, J. P. Helferty, E. A. Hoffman, G. McLennan, and W. E. Higgins. Three-dimensional path planning for virtual bronchoscopy. *IEEE Transactions on Medical Imaging*, 23(9):1365–1379, 2004.

[90] Ziyue Xu, Ulas Bagci, Brent Foster, Awais Mansoor, Jayaram K Udupa, and Daniel J Mollura. A hybrid method for airway segmentation and automated

measurement of bronchial wall thickness on CT. *Medical image analysis*, 24(1):1–17, may 2015.

[91] Florent Grélard, Fabien Baldacci, Anne Vialard, and Jacques-Olivier Lachand. Precise cross-section estimation on tubular organs. In *Computer Analysis of Images and Patterns*, 2015.

[92] Benjamin L. Odry, Atilla P. Kiraly, Carol L. Novak, David P. Naidich, and Jean-Francois Lerallut. An evaluation of automated broncho-arterial ratios for reliable assessment of bronchiectasis. In *Proceedings of SPIE*, 2008.

[93] Juerg Tschirren, Eric A. Huffman, Geoffrey McLennan, and Milan Sonka. Intrathoracic airway trees: Segmentation and airway morphology analysis from low-dose CT scans. *IEEE Transactions on Medical Imaging*, 24(12):1529–1539, 2005.

[94] Daniel A Moses, Laughlin Dawes, Claude Sammut, and Tatjana Zrimec. Peripheral bronchial identification on chest CT using unsupervised machine learning. *International Journal of Computer Assisted Radiology and Surgery*, 13(9):1379–1395, 2018.

[95] P Thévenaz, T Blu, and M Unser. Interpolation revisited. *IEEE Transactions on Medical Imaging*, 19(7):739–758, jul 2000.

[96] Suicheng Gu, Carl Fuhrman, Xin Meng, Jill M. Siegfried, David Gur, Joseph K. Leader, Frank C. Sciurba, and Jiantao Pu. Computerized identification of airway wall in CT examinations using a 3D active surface evolution approach. *Medical Image Analysis*, 17(3):283–296, 2013.

[97] Atilla P Kiraly, Benjamin L Odry, David P Naidich, and Carol L Novak. Boundary-Specific cost functions for Quantitative Airway Analysis. In *Medical Image Computing and Computer-Assisted Intervention*, 2007.

[98] Osama I Saba, Eric A Hoffman, and Joseph M Reinhardt. Maximizing quan-

titative accuracy of lung airway lumen and wall measures obtained from X-ray CT imaging. *Journal of Applied Physiology*, 95(3):1063–75, sep 2003.

[99] Anthony De Soyza, Timothy Aksamit, Tiemo-Joerg Bandel, Margarita Criollo, J. Stuart Elborn, Elisabeth Operschall, Eva Polverino, Katrin Roth, Kevin L. Winthrop, and Robert Wilson. RESPIRE 1: A phase III placebo-controlled randomised trial of ciprofloxacin dry powder for inhalation in non-cystic fibrosis bronchiectasis. *The European respiratory journal*, 51:1702052, 2018.

[100] J D Chalmers, S Aliberti, A Filonenko, M Shteinberg, P C Coeminne, A T Hill, T C Fardon, D Obradovic, C Gerlinger, G Sotgiu, E Operschall, R A Rutherford, K Dimakou, E Polverino, A De Soyza, and M J McDonnell. Characterization of the Frequent Exacerbator Phenotype in Bronchiectasis. *American Journal of Respiratory and Critical Care Medicine*, 197(11):1410–1420, 2018.

[101] Luce Cantin, Alexander A Bankier, and Ronald L Eisenberg. Bronchiectasis. *American Journal of Roentgenology*, 193(3):W158–W171, 2009.

[102] Jean-Paul Charbonnier, Eva M. van Rikxoort, Arnaud A.A. Setio, Cornelia M. Schaefer-Prokop, Bram van Ginneken, and Francesco Ciompi. Improving airway segmentation in computed tomography using leak detection with convolutional networks. *Medical Image Analysis*, 36:52–60, 2017.

[103] Zijian Bian, Jean-Paul Charbonnier, Jiren Liu, Dazhe Zhao, David A Lynch, and Bram van Ginneken. Small airway segmentation in thoracic computed tomography scans: A machine learning approach. *Physics in Medicine and Biology*, 63(15):155024, 2018.

[104] Zepa Yang, Hyeongmin Jin, and Jong Hyo Kim. Attenuation Profile Matching: An accurate and scan parameter-robust measurement method for small airway dimensions in low-dose CT scans. *Medical Physics*, 45(9):4145–4157, 2018.

[105] Raúl San José Estépar, George G Washko, Edwin K Silverman, John J Reilly, Ron Kikinis, and Carl-Fredrik Westin. Accurate airway wall estimation using phase congruency. In *Medical Image Computing and Computer-Assisted Intervention*, jan 2006.

[106] Terry E Robinson, Frederick R Long, Pavi Raman, Paramita Saha, M J Emond, Joseph M Reinhardt, Raghav Raman, and Alan S Brody. An airway phantom to standardize CT acquisition in multicenter clinical trials. *Academic Radiology*, 16(9):1134–1141.e1, 2009.

[107] Masaru Hasegawa, Yasuyuki Nasuhara, Yuya Onodera, Hironi Makita, Katsura Nagai, Satoshi Fuke, Yoko Ito, Tomoko Betsuyaku, and Masaharu Nishimura. Airflow limitation and airway dimensions in chronic obstructive pulmonary disease. *American Journal of Respiratory and Critical Care Medicine*, 173(12):1309–1315, 2006.

[108] Tsuyoshi Oguma, Toyohiro Hirai, Akio Niimi, Hisako Matsumoto, Shigeo Muro, Michio Shigematsu, Takashi Nishimura, Yoshiro Kubo, and Michiaki Mishima. Limitations of airway dimension measurement on Iimages obtained using multi-detector row computed tomography. *PLoS ONE*, 8(10):e76381, oct 2013.

[109] Tobias Achenbach, Oliver Weinheimer, Christoph Brochhausen, David Hollemann, Bastian Baumbach, Alexander Scholz, and Christoph Düber. Accuracy of automatic airway morphometry in computed tomography - Correlation of radiological-pathological findings. *European Journal of Radiology*, 81:183–188, 2012.

[110] Rafael Wiemker, Udo van Stevendaal, Holger Schmitt, Amnon Steinberg, Ekta Dharaiya, Mark Rabotnikov, and Tobias Klinder. Comparison of correction methods for bronchial lumen and wall thickness measurement using a physical tube array phantom. In *Proceedings of SPIE*, 2013.

[111] Anil K. Jain. *Fundamentals of digital image processing*. Prentice Hall, 1989.

[112] George C. Kagadis, Nancy L. Ford, Dimitrios N. Karnabatidis, and George K. Loudos. *Handbook of small animal imaging : preclinical imaging, therapy, and applications*. CRC Press, 2019.

[113] V. Patel, R. N. Chityala, K. R. Hoffmann, C. N. Ionita, D. R. Bednarek, and S. Rudin. Self-calibration of a cone-beam micro-CT system. *Medical Physics*, 39(1):2009, 2009.

[114] Jane S Matsumoto, Jonathan M Morris, Thomas A Foley, Eric E Williamson, Shaui Leng, Kiaran P McGee, Joel L Kuhlmann, Linda E Nesberg, and Terri J Vrtiska. Three-dimensional physical modeling: Applications and experience at Mayo Clinic. *Radiographics*, 35(7):1989–2006, 2015.

[115] Emily Hammond, Chelsea Sloan, John D. Newell Jr, Jered P. Sieren, Melissa Saylor, Craig Vidal, Shayna Hogue, Frank De Stefano, Alexa Sieren, Eric A. Hoffman, and Jessica C. Sieren. Comparison of low- and ultralow-dose computed tomography protocols for quantitative lung and airway assessment. *Medical Physics*, 44(9):4747–4757, 2017.

[116] Patricia Leutz-Schmidt, Oliver Weinheimer, Bertram J. Jobst, Julien Dinkel, Jürgen Biederer, Hans-Ulrich Kauczor, Michael U. Puderbach, and Mark O. Wielpütz. Influence of exposure parameters and iterative reconstruction on automatic airway segmentation and analysis on MDCT An ex vivo phantom study. *Plos One*, 12(8):e0182268, 2017.

[117] Jonathan C. Wong, Yasutaka Nakano, Harvey O. Coxson, Nestor L. Müller, Peter D. Paré, and James C. Hogg. The influence of reconstruction algorithm on the measurement of airway dimensions using computed tomography. In *Proceedings of SPIE*, 2008.

[118] J Ken Leader, Bin Zheng, Frank C Sciurba, Harvey O Coxson, Carl R Fuhrman, Jessica M McMurray, Sang C Park, Glenn S Maitz, and David Gur. Quantification of airway morphometry: the effect of CT acquisition and reconstruction parameters. In *Proceedings of SPIE*, 2007.

[119] Bin Zheng, Joseph K. Leader, Jessica M. McMurray, Sang Cheol Park, Carl R. Fuhrman, David Gur, and Frank C. Sciurba. Automated detection and quantitative assessment of pulmonary airways depicted on CT images. *Medical Physics*, 34(7):2844–2852, 2007.

[120] Catalin Fetita, Margarete Ortner, Pierre-Yves Brillet, Francoise Preteux, and Philippe A Grenier. Volumetric quantification of airway wall in CT via collision-free active surface model: application to asthma assessment. *IEEE Transactions on Image Processing*, 33(7):1512–1526, 2014.

[121] Donald P Frush, Christopher C Slack, Caroline L Hollingsworth, George S Bisset, Lane F Donnelly, Jiang Hsieh, Trudy Lavin-Wensell, and John R Mayo. Computer-simulated radiation dose reduction for abdominal multidetector CT of pediatric patients. *American Journal of Roentgenology*, 179(2):1107–1113, 2002.

[122] Rafael C. Gonzalez, Richard Eugene Woods, and Steven L. Eddins. *Digital Image Processing Using MATLAB*. Pearson Prentice Hall, 2011.

[123] Xin Sui, Felix G Meinel, Wei Song, Xiaoli Xu, Zixing Wang, Yuyan Wang, Zhengyu Jin, Jiuhong Chen, Rozemarijn Vliegenthart, and U Joseph Schoepf. Detection and size measurements of pulmonary nodules in ultra-low-dose CT with iterative reconstruction compared to low dose CT. *European Journal of Radiology*, 85(3):564–570, 2016.

[124] Yukihiro Nagatani, Masashi Takahashi, Kiyoshi Murata, Mitsuru Ikeda, Tsuneo Yamashiro, Tetsuhiro Miyara, Hisanobu Koyama, Mitsuhiro Koyama, Yukihisa Sato, Hiroshi Moriya, Satoshi Noma, Noriyuki Tomiyama, Yoshiharu Ohno, and Sadayuki Murayama. Lung nodule detection performance in five observers on computed tomography (CT) with adaptive iterative dose reduction using three-dimensional processing (AIDR 3D) in a Japanese multicenter study: Comparison between ultra-low-dose CT and low-dose CT by

receiver-operating characteristic analysis. *European Journal of Radiology*, 84(7):1401–1412, 2015.

[125] A. Larbi, C. Orliac, J. Frandon, F. Pereira, A. Ruyer, J. Goupil, F. Macri, J. P. Beregi, and J. Greffier. Detection and characterization of focal liver lesions with ultra-low dose computed tomography in neoplastic patients. *Diagnostic and Interventional Imaging*, 99(5):311–320, 2018.

[126] M R Spiegal and L J Stephens. *Schaum's outline of theory and problems of statistics*. McGraw-Hill Education, 1998.

[127] J Tschirren, T Yavarna, and J M Reinhardt. Airway Segmentation Framework for Clinical Environments. In *The Second International Workshop on Pulmonary Image Analysis*, 2009.

[128] Chang Won Kim and Jong Hyo Kim. Realistic simulation of reduced-dose CT with noise modeling and sinogram synthesis using DICOM CT images. *Medical Physics*, 41(1):011901–1–15, 2014.

[129] Tomomi Takenaga, Shigehiko Katsuragawa, Makoto Goto, Masahiro Hatemura, Yoshikazu Uchiyama, and Junji Shiraishi. A computer simulation method for low-dose CT images by use of real high-dose images: a phantom study. *Radiological Physics and Technology*, 9(1):44–52, 2016.

[130] Robiël E. Naziroglu, Vincent F. van Ravesteijn, Lucas J. van Vliet, Geert J. Streekstra, and Frans M. Vos. Simulation of scanner- and patient-specific low-dose CT imaging from existing CT images. *Physica Medica*, 36:12–23, 2017.

[131] Xiang Li, Ehsan Samei, David M. DeLong, Robert P. Jones, Ana Maria Gaca, Caroline L. Hollingsworth, Charles M. Maxfield, James G. Colsher, and Donald P. Frush. Pediatric MDCT: Towards Assessing the Diagnostic Influence of Dose Reduction on the Detection of Small Lung Nodules. *Academic Radiology*, 16(7):872–880, 2009.

[132] M Robins, J Solomon, J Hoye, E Abadi, D Marin, and E Samei. How reliable are texture measurements? In *Proceedings of SPIE*, 2018.

[133] Jørn Justesen and Søren Forchhammer. *Two-Dimensional Information Theory and Coding: With Application to Graphics and High-Density Storage Media*. Cambridge University Press, 2009.

[134] John Hoffman, Stefano Young, Frédéric Noo, and Michael McNittGray. Technical Note: FreeCT_wFBP: A robust, efficient, opensource implementation of weighted filtered backprojection for helical, fanbeam CT. *Medical Physics*, 43(3):1411–1420, 2016.

[135] A Rodriguez, F N Ranallo, P F Judy, D S Gierada, and S B Fain. CT reconstruction techniques for improved accuracy of lung CT airway measurement. *Medical Physics*, 41(11):111911–1–111911–8, 2014.

[136] Qier Meng, Takayuki Kitasaka, Masahiro Oda, Junji Ueno, and Kensaku Mori. Airway Segmentation from 3D Chest CT Volumes Based on Volume of Interest Using Gradient Vector Flow. *Medical Imaging Technology*, 36(3):133–146, 2018.

[137] Joseph Paul Cohen, Margaux Luck, and Sina Honari. Distribution Matching Losses Can Hallucinate Features in Medical Image Translation. In *Medical Image Computing and Computer Assisted Intervention*, 2018.

[138] B. C. Stoel, F. Bode, A. Rames, S. Soliman, J. H. C. Reiber, and J. Stolk. Quality control in longitudinal studies with computed tomographic densitometry of the lungs. *Proceedings of the American Thoracic Society*, 5(9):929–933, 2008.

[139] David G. Parr, Berend C. Stoel, Jan Stolk, Peter G. Nightingale, and Robert A. Stockley. Influence of calibration on densitometric studies of emphysema progression using computed tomography. *American Journal of Respiratory and Critical Care Medicine*, 170:883–890, 2004.

[140] John R Hurst. Microbial dysbiosis in bronchiectasis. *The Lancet Respiratory Medicine*, 2(12):945–7, 2014.

[141] J Jacob, B J Bartholmai, S Rajagopalan, M Kokosi, A Nair, R Karwoski, S L F Walsh, A U Wells, and D M Hansell. Mortality prediction in idiopathic pulmonary fibrosis: evaluation of computer-based CT analysis with conventional severity measures. *European Respiratory Journal*, 49(1):1601011, 2017.

[142] Philip Konietzke, Oliver Weinheimer, Mark O. Wielpütz, Willi L. Wagner, Philine Kaukel, Ralf Eberhardt, Claus P. Heussel, Hans Ulrich Kauczor, Felix J. Herth, and Maren Schuhmann. Quantitative CT detects changes in airway dimensions and air-trapping after bronchial thermoplasty for severe asthma. *European Journal of Radiology*, 107:33–38, 2018.

[143] Lee Gazourian, Samuel Ash, Emily E.K. Meserve, Alejandro Diaz, Raul San Jose Estepar, Souheil Y. El-Chemaly, Ivan O. Rosas, Miguel Divo, Anne L. Fuhlbrigge, Phillip C. Camp, Vincent T. Ho, Ami S. Bhatt, Hilary J. Goldberg, Lynette M. Sholl, and George R. Washko. Quantitative computed tomography assessment of bronchiolitis obliterans syndrome after lung transplantation. *Clinical Transplantation*, 31(5):e12943, 2017.

[144] David Siegmund, Benjamin Yakir, and Nancy R Zhang. Detecting simultaneous varient intervals in aligned sequences. *The Annals of Applied Statistics*, 5(2A):645–668, 2011.

[145] T. Mikosch and C. Stric. Changes of structure in financial time series and the GARCH model. *REVSTAT Statistical Journal*, 2(1):41–73, 2004.

[146] Peter J. Green. Reversible jump Markov Chain Monte Carlo computation and Bayesian model determination. *Biometrika*, 82(4):711–732, 1995.

[147] Peter J Green and David I Hastie. Reversible jump MCMC. *Genetics*, 155(3):1391–1403, 2009.

[148] X Wu, G H Kim, M L Salisbury, D Barber, B J Bartholmai, K K Brown, C S Conoscenti, J De Backer, K R Flaherty, J F Gruden, E A Hoffman, S M Humphries, J Jacob, T M Maher, G Raghu, L Richeldi, B D Ross, R Schlenker-Herceg, N Sverzellati, A U Wells, F J Martinez, D A Lynch, J Goldin, and S L F Walsh. Computed tomographic biomarkers in idiopathic pulmonary fibrosis: The future of quantitative analysis. *American Journal of Respiratory and Critical Care Medicine*, pages 1–41, 2018.

[149] Andrew Gelman, John B Carlin, Hal S Stern, David B Dunson, Aki Vehtari, and Donald B Rubin. *Bayesian Data Analysis*. CRC Press, 3rd edition, 2014.

[150] S J D Prince. *Computer Vision: Models, Learning, and Inference*. Cambridge University Press, 2012.

[151] Siddhartha Chib and Edward Greenberg. Understanding the Metropolis-Hastings Algorithm. *The American Statistician*, 49(4):327–335, 1995.

[152] Alfredo Morales Pinzón, Marcela Hernández Hoyos, Jean-Christophe Richard, Leonardo Flórez-Valencia, and Maciej Orkisz. A tree-matching algorithm: Application to airways in CT images of subjects with the acute respiratory distress syndrome. *Medical Image Analysis*, 35:101–115, 2017.

[153] Michael W Graham and William E Higgins. Globally optimal model-based matching of anatomical trees. In *Proceedings of SPIE*, 2006.

[154] Nicola Sverzellati and Pierre-Yves Brillet. When Deep Blue first defeated Kasparov: is a machine stronger than a radiologist at predicting prognosis in idiopathic pulmonary fibrosis? *European Respiratory Journal*, 49:1602144, 2017.

[155] Frank Hilberg, Gerald J. Roth, Martin Krssak, Susanna Kautschitsch, Wolfgang Sommergruber, Ulrike Tontsch-Grunt, Pilar Garin-Chesa, Gerd Bader, Andreas Zoephel, Jens Quant, Armin Heckel, and Wolfgang J. Rettig. BIBF 1120: Triple angiokinase inhibitor with sustained receptor blockade and good antitumor efficacy. *Cancer Research*, 68(12):4774–4782, 2008.

[156] M L Chabia, A Goracci, N Rochec, A Paugamd, A Lupoe, and M P Revelf. Pulmonary aspergillosis. *Diagnostic and Interventional Imaging*, 96:435–442, 2015.